Model of Water Evaporation Stage During Drying of Latex Coatings

A Thesis

Submitted to the Faculty

of

Drexel University

by

Venkata Ramana Gundabala

in partial fulfillment of the

requirements for the degree

of

Master of Science in Chemical Engineering

December 2002

Dedications

Dedicated to my parents

Acknowledgements

I would like to acknowledge several people who have helped me through out my research period. My research advisor, Dr. Richard Cairncross has been a great influence in my development as an independent researcher. Individual and group meetings all through the two years have helped me hone my analyzing and thinking skills. His suggestions and critical comments on reports and presentations have improved my writing and communicating skills. I owe my gratitude to him.

I would also like to thank Dr. Cameron Abrams and Dr. Nily Dan for readily agreeing to serve as thesis committee members. Thanks are also due to Dorothy Porter for her administrative help and Dan Luu for technical help. I would like to thank my lab mates Amitkumar Jain and Srinath Madasu for extending a helping hand whenever I needed. I would also like to thank all the chemical engineering graduate students who made my life at Drexel a memorable one.

Lastly, I owe my gratitude to my parents for their constant support and encouragement.

Table of Contents

List of Tables

List of Figures

Abstract

Model of Water Evaporation Stage during Drying of Latex Coatings

Venkata Ramana Gundabala

Richard Allan Cairncross, Ph.D

Traditional solvent-based coatings pose several environmental concerns due to high volatility and polluting effects of the solvents. Water-based latex coatings have been identified as a worthy alternative because of the ease of application; however the properties of latex coatings are often inferior to solvent-based coatings due to incomplete film formation. To achieve suitable film properties for most applications, it is necessary for latex particles to aggregate and coalescence into a continuous film during drying. Film formation during drying of latex coatings is occurs in three stages.

This thesis presents a particle dynamics model that predicts evolution of particle layers and packing structure during the first stage of drying of latex coatings, which is period of constant evaporation rate. In this model the inertia of particles is negligible and the velocity and trajectory of each particle is determined by balancing the drag force on the particle with interparticle repulsion, surface tension and Brownian forces. DLVO theory was used to predict the screened electrostatic interactions between particles. The Brownian force has random magnitude and direction to simulate random particle motions observed in colloidal systems.

Areal density profiles and 3D plots are used to make base case and parametric analysis on evolution of particle layers and packing structure. The parameters used for investigation include electrolyte concentration, drying rate, particle size, magnitude of random force variance, initial volume fraction, and initial particle distribution. FCC and HCP are the most commonly observed packing structures. The results show that use of smaller particle sizes, lower electrolyte concentrations, and slower drying rates produce more highly ordered packing structure.

Chapter 1: Introduction

1.1 Motivation

Traditional solvent-based coatings pose several environmental concerns due to high volatility and polluting effects of the solvents. Drying of solvent-based coatings produces large amounts of volatile organic compounds (VOC). Increasing government regulations on VOC emission have put pressure on the coating industry to reduce or eliminate solvents in coating formulations. Several alternatives such as high solids, 100% solids, melts, powders, and water-based coatings exist, but water-based latex coatings have been identified as a worthy alternative because of the ease of application and faster drying. Latex coatings are dispersions of polymer particles in a suspending medium, usually water. From their first use in the paint industry, latex coatings have found wide range of applications in the past half-century. Presently they find applications in paints, paper coatings, and pressure-sensitive adhesives.

The use of latex coatings in most applications is based on the formation of a continuous film during drying. The industrial applications of these films depend on their final mechanical and transport properties. The final film properties depend not only on the properties of the polymers used but also on the method of preparation of latexes and their film formation mechanism.

Film formation during drying of latex coatings is known to occur in 3 stages as depicted in Figure 1.1. Stage I is the water evaporation stage; in Stage I the particles are disperse and particle contact is infrequent. As water evaporates, the

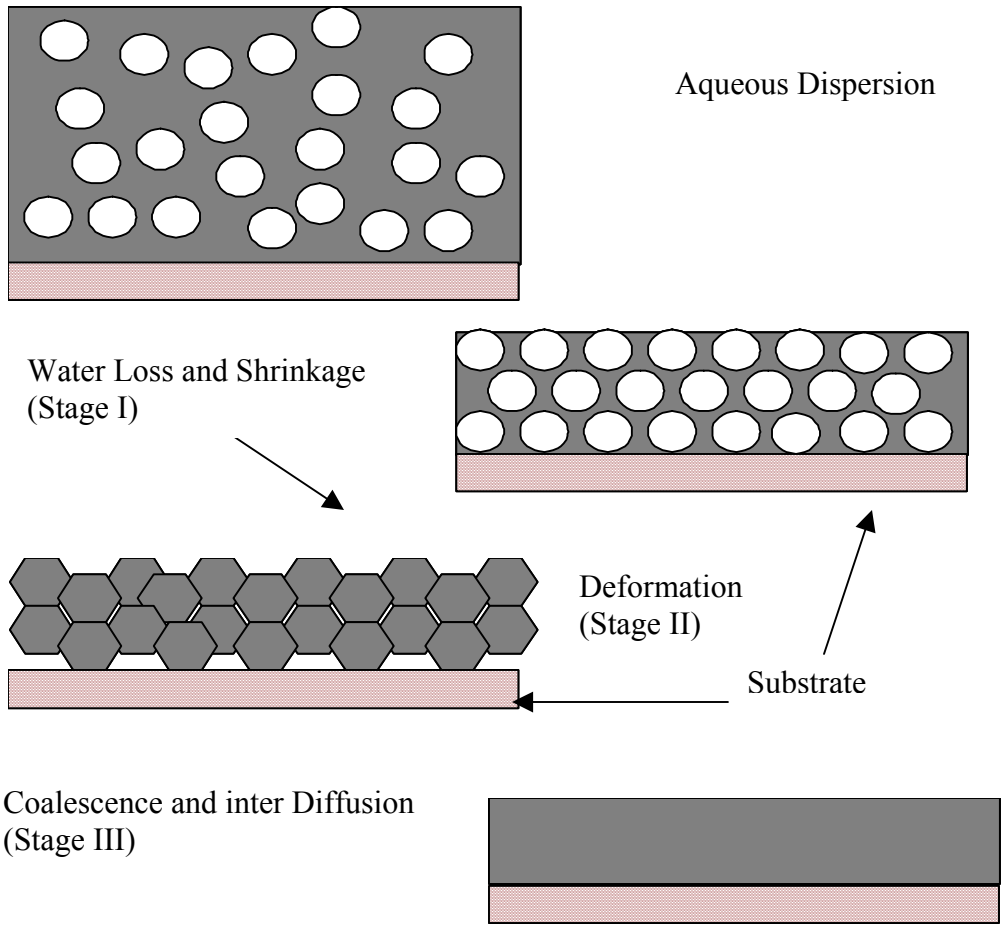

Figure 1.1 Three stages of Film Formation
(Adapted from Du Chesne et. al. 1999).

particles come closer together and either arrange into an ordered packing or distribute randomly, depending on the magnitude of various parameters involved in the drying process. Stage II is the particle deformation stage during which particles deform under the influence of capillary forces. Stage III is the coalescence stage during which polymer diffusion across particle boundaries results in the formation of a continuous film.

The films obtained from drying of water-based latex coatings are often inferior to those obtained from solvent-based coatings in terms of their final permeability and mechanical properties. This inferiority in properties may be due to non-uniformities and presence of voids in the final film, an indication of incomplete film formation. Incomplete film formation may be a result of non-uniform drying, incomplete particle deformation, improper chain diffusion or some other non-uniformity. These phenomena are influenced in a complicated manner by several parameters such as rate of evaporation, polymer properties, particle size, etc. It is the lack of proper understanding of the influence of these parameters on film forming mechanism that is responsible for the inability to properly control the properties of the films obtained from drying of water-based latex coatings.

Several researchers carried out investigations on the forces causing deformation in Stage II. Several theories were proposed to explain the mechanism of deformation. Capillary forces were identified as the main driving force for deformation (Brown, 1956). Experimental work was also done to study the type and extent of particle ordering in the first stage of film formation. In most observations (Monovoukas et. al. (1988), He et. al. (1996)), either face centered cubic packing or hexagonal cubic packing was identified at the end of first stage. The type and extent of ordering was found to depend on several parameters such as particle volume fraction, electrolyte concentration, rate of evaporation, and particle size. A model that takes into account all the forces in particle ordering during Stage I, would be useful in evaluating the relative magnitude of various parameters that result in different levels

of ordering and layering. This thesis studies particle ordering and layering phenomena occurring during the first stage.

1.2 Background

Latex dispersions are a category of stabilized colloidal suspensions in which the dispersion medium is water and the dispersed phase consists of polymer particles. In real systems, the dispersion medium contains several other components such as electrolytes, surfactants, initiators, emulsifiers, etc. Based on their thermodynamic stability, colloidal dispersions can be broadly classified into two categories: *lyophilic* (solvent-loving) and *lyophobic* (solvent-hating). If the solvent is water, they are called *hydrophilic* and *hydrophobic*, respectively.

Lyophilic dispersions are thermodynamically stable because of the affinity of the particles of the dispersed phase to the molecules of the dispersion medium. Due to this affinity, there is a decrease in Gibbs free energy when the particles are dispersed. In the case of lyophobic dispersions, dispersion of particles results in an increase in Gibbs free energy, thereby making them thermodynamically unstable. So, they tend to undergo aggregation, as soon as they are dispersed. But, almost all industrial applications require the lyophobic dispersions to undergo controlled aggregation i.e. the dispersions need to be metastable or unstable to coagulate. This is generally achieved through either charge stabilization (presence of charged functional groups on particle surfaces) or steric stabilization (presence of ionic or non-ionic surfactants on particle surfaces). The barrier to coagulation caused by charge or steric stabilization on lyophobic colloidal particles is only a kinetic one; their

thermodynamic stability is unaltered. Over long periods of time, they ultimately form an aggregate.

The charge present on latex particles is generally obtained from surfactants that are added during their preparation. Common functional groups on the surfactant molecules are carbonic, sulphonic acid and tertiary amine groups. Emulsifiers are added to prevent particle coagulation during polymerization and to provide long-term stability to the system. They provide stability either electrostatically or sterically depending on whether the emulsifier used is an anionic surfactant or nonionic surfactant respectively. Molecular weight modifiers or chain transfer agents such as carbon tetra bromide are sometimes added to control the chain length of the polymers and thereby to control the molecular weight of the polymers.

Latex particle preparation is generally carried through a stepwise or semi continuous emulsion polymerization. Acrylates, methacrylates and vinyl acrylates are common monomers. The polymerization reaction is carried out by loading the monomers along with an initiator and an emulsifier into the reactor. Typical particle sizes obtained from this reaction range from 100 nm to 1000 nm.

1.3 Stages of Film Formation

Research during the last five decades on film formation has covered wide range of topics ranging from the very basic question of whether water has any role to play in film formation (Dobler et. al. 1992) to more complicated issues like the effect of pigments on film formation (Sheehan et. al. 1993) and the use of latex blends (Keddie et. al. 1995) and core shell morphologies (Jaonicot et. al. 1990) to enhance film properties. Based on their studies on drying of latex dispersions, Vanderhoff et

al. (1973) proposed a three-stage model for film formation. In Stage I, water evaporation occurs at a constant rate, resulting in an increase in solid concentration. During this stage, the particles are in continuous Brownian motion and as inter-particle distance decreases, electrostatic interactions dominate over the thermal interactions. This stage comes to an end once enough water has evaporated to make the particles to arrange themselves into a close packed array. Eckersley et al. (1994) made gravimetric and E-SEM studies to confirm that drying rate in this stage is constant. The drying rate is comparable (about 85%) to the evaporation rate of pure water (Croll (1986)).

Stage II starts when the particles come into close contact. The rate of drying in Stage II decreases (Figure 1.3) due to decreasing air/water interface area available for evaporation, which is a result of increasing regions of coalesced film. The particles undergo deformation due to coalescence under the influence of several forces based on the drying conditions. Stage III is the polymer interdiffusion stage when particle boundaries cease to exist and diffusion of polymer chains takes place. The drying rate during this stage decreases drastically due to diffusion controlled evaporation. Film formation from latex dispersions, according to Vanderhoff et al., can be viewed as transformation from a dispersion to close packed aggregate of particles (Stage I) and then to an aggregate of deformed particles (Stage II), followed by the formation of a continuous film (Stage III).

Croll (1986) proposed a two-stage model of film formation for acrylic latexes. The first stage is similar to that of Vander Hoff et al. but he invoked the presence of a vertical drying front which moves downwards leaving behind a dry porous layer and

a wet layer beneath (Figure 1.2). He observed that the evaporation rate was independent of film thickness, particle size and composition. From these observations he concluded that the air-water interface area remained constant throughout the drying process resulting in a constant drying rate period. The second stage is characterized by a falling rate period of drying which is due to decrease in supply of water to the drying front from wet layer beneath. From his experiments, Croll could not establish the exact reason for the decrease in the supply of water during this stage. Though Croll proposed a two-stage model it can be assumed that polymer chain interdiffusion follows the second stage of Croll's model. The drying rate curve for the entire period of film formation as observed by Vanderhoff et al. and Croll is shown in Figure 1.3, with constant drying rate seen for most part of drying.

Modern instrumental techniques have facilitated researchers to make extensive investigation on drying rates, skin formation and particle ordering during the first stage. The next section presents a review of the past experimental work done on film forming mechanism during Stage I.

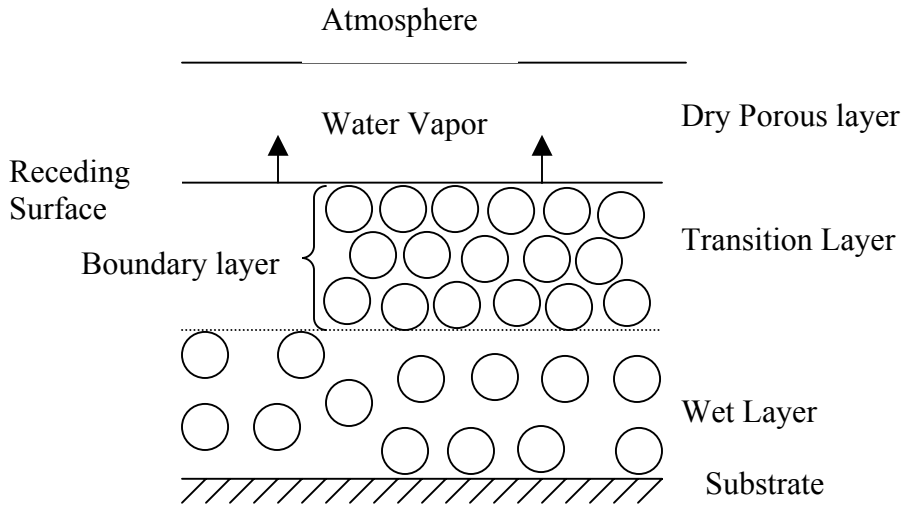

Figure 1.2 Croll's Receding Front Model
(Adapted from Croll 1986)

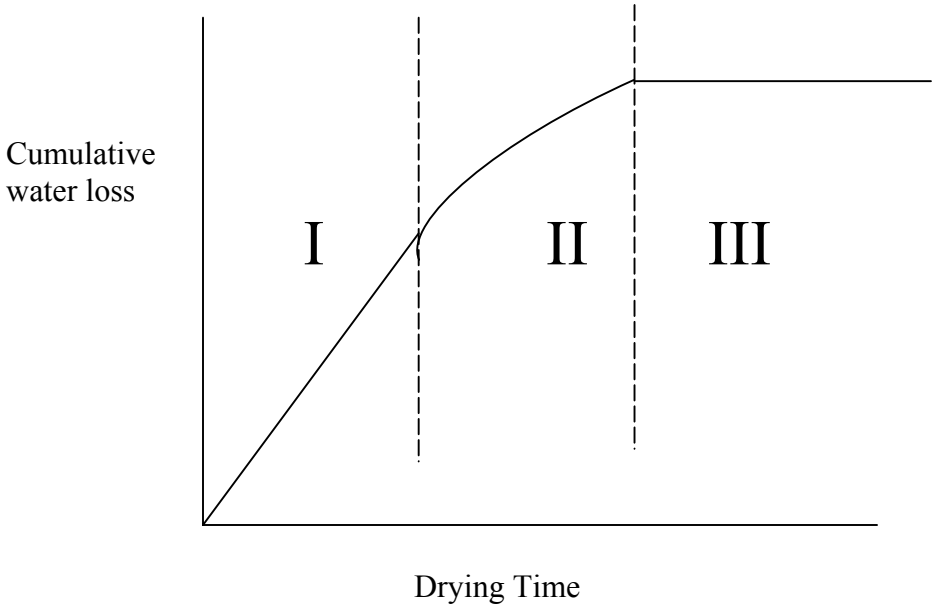

Figure 1.3 Water loss during latex drying

1.4 Stage I of Film Formation: Water Evaporation

Many researchers have used ESEM (environmental-scanning electron microscopy), cryogenic SEM, atomic force microscopy, ellipsometry, SANS (small angle neutron spectroscopy), SAXS (small angle X-ray scattering) to investigate the effect of various parameters on Stage I of film formation for various latex systems.

1.4.1 Measurements of Film Formation: Effect of T_g and Drying Temperature

Keddie et al. (1995) used ESEM and ellipsometry to measure the influence of drying temperature and polymer glass transition temperature (T_g) on skin formation (reported by Croll (1986)) and kinetics of film formation. In the case of soft latexes i.e. latexes with low T_g, particles continuously deform during film formation, thereby reducing the area of air-water interface and the evaporation rate. So water evaporation is the rate-limiting step and no drying front can be observed. In the case of hard latexes (high T_g latexes), particle deformation by viscous flow is the rate-

limiting step and a drying front recedes inward. At low temperatures, low T_g latexes (soft latexes) film formed at longer times compared to high T_g latexes, probably due to decrease in evaporation rate in case of low T_g latexes.

1.4.2 Measurements of Packing and Structure

a) Effect of Electrolytes

He et al. (1996) used ESEM to show how salt ($MgSO_4$) concentration affects particle ordering and type of packing obtained at end of Stage I for core shell polymer lattices. Without added salt, evaporation of water produced hexagonal or cubic packing at the end of Stage I. Addition of salts destabilizes latex dispersions and evaporation of water produced a randomly packed structure.

Light diffraction measurements (Monovoukas et al. (1988)) on crystal evolution of highly charged monodisperse polystyrene latex dispersions with added salt (KCl) showed that ordering of particles is a function of ionic strength of the dispersion. BCC structure was found to be thermodynamically stable at very low ionic strengths and very low particle volume fractions. At higher volume fractions the crystal structure evolves into FCC. As ionic strength was increased, the size of crystallites and lattice spacings decreased due to domination of Vander Waals forces over screened repulsions.

Sheehan et al. (1993) used Cryogenic SEM to show how ionic strength and extent of carboxylation influenced the type of packing obtained from drying of styrene-butadiene latexes. Systems with higher degree of carboxylation had higher stability against coalescence even at ionic strengths greater than that required for removing electrostatic repulsions. At low ionic strengths, such systems evolved into

hexagonal close-packed structure, unlike the systems with lower degree of carboxylation, which produced disordered packing at end of Stage I.

b) Effect of Drying Rate

Pusey et al. (1989) used light-scattering measurements to analyze the structure of crystals obtained from hard colloidal spheres. The particles were sterically stabilized using poly-12-hydroxystearic acid. Crystals obtained from slow evaporation showed face-centered-cubic packing structure. Slower evaporation rates allow more time for particles to explore lattice sites. Based on free energy consideration, FCC is the most favorable structure for crystals obtained from hard colloidal spheres (Frenkel et al. (1986)).

Rieger et al. (1992) used SANS to investigate the structure of packing obtained from styrene/n-butyl acrylate copolymer latex. Under proper system conditions, the latex evolved into FCC packing. However, higher evaporation rates resulted in less well-defined crystalline packing.

c) Effect of Particle Dispersity

Dingenouts et al. (1998) used SAXS to investigate the influence of particle dispersity on packing obtained at end of Stage I of film formation. In order to exclusively study the first stage they used high T_g polymer and dried the latex dispersion at temperatures below T_g. This would prevent any deformation of particles during Stage I. The system evolved into a highly ordered structure without true long-range order. They attributed the absence of long-range order to the residual polydispersity in their system; increasing polydispersity decreased the ordering observed.

AFM images of films formed from PMMA/PBMA latex dispersions (Butt et al. 1994) showed hexagonal close-packed structures that extended over short ranges. Higher thickness of film and broader particle size distribution apparently inhibited long range ordering.

Jaonicot et al. (1990) used SANS to observe the affect of particle volume fraction, salt presence and particle dispersity on type of packing obtained at the end of Stage I of film formation. The particles used in their experiments had hydrophobic copolymer latex core with hydrophilic shell. The shell stabilizes the particles from aggregation. Monodisperse latex dispersions with considerable particle volume fraction evolved into a close packing of FCC in the absence of any salts. Dilute dispersions, presence of salt and polydispersity of particles prevented long range ordering.

d) Effect of Substrate

Higoshita et al. (1991) investigated the influence of substrate on particle packing. When monodisperse latexes were deposited onto semi permeable substrate (cellulose membrane), it was found that formation of ordered array was related to the existence of a secondary minimum of potential between substrate and particles.

Li et al. (1996) observed the formation of 2-D crystal arrays in monolayer and multilayer film formation using AFM and reported that unannealed samples formed disordered arrays. Structure of monolayer arrays was found to be influenced by the nature of the substrate (mica, glass, etc).

e) Other Effects

Freeze-fracture electron microscopy investigations made by Wang et al. (1992) dealt with the influence of surfactant and particle size on type of packing obtained at the end of Stage I. In the absence of surfactant, systems with larger particle sizes (337 nm) evolved into FCC packing. When a surfactant is present, smaller domains of FCC packing could be seen. Systems with smaller particle sizes (117 nm) gave random packing structures.

Chevalier et al. (1992) used SANS and Transmission Electron Microscopy to examine the influence of magnitude of charge stabilizaton on type of packing obtained at end of Stage I. Films were produced by casting two different core shell latex systems on quartz and glass. The two systems had same cores but different shells, which produced electrostatic repulsions of different magnitudes. Systems with higher repulsive interactions produced FCC structure over a long range.

Denkov et al. (1992) used optical microscopy to investigate the forces influencing particle arrangement during formation of 2-D crystals from polystyrene latex spheres cast on a horizontal glass substrate. They concluded that only lateral capillary forces influenced the particle arrangement. Neither electrostatic repulsion nor Vander Waals attraction played a significant role in formation of 2-D arrays.

From the several experimental observations made on Stage I of film formation, it is evident that the type of packing and extent of ordering obtained depends on several parameters such as type of latex, particle size, presence of surfactant, ionic concentration, nature of substrate, rate of drying.

1.4.3 Models of Stage I of Film Formation

The complicated dynamics involved with discrete particle systems and the difficulties involved in dealing with systems involving simultaneous occurrence of several processes has restricted researchers from using models to investigate the mechanism of latex film formation. The models that exist only deal with specific parameters and processes influencing final film formation.

Croll (1987) developed a mathematical model that predicts evaporation rate during the first two stages of film formation. Both conduction and convection processes were considered to occur within the coating. During the first stage the evaporation rate is mainly influenced by the environmental conditions and temperature of coating. In the second stage the concentration of water in the transition layer was the main parameter in determining the evaporation rate. Croll also showed that under normal conditions, wet layer occupies majority of total film thickness.

In a study of non-uniformities in lateral drying, Routh et al. (1998) developed a model that predicts the propagation of drying fronts in the horizontal direction during solvent evaporation. Vertical uniformity in drying was ensured by taking zero Peclet number. Lubrication approximation was used to track the position of the front of close-packed particles and thereby the propagation of drying front.

Qi Liao et al. (2000) performed Brownian dynamics simulations to investigate Stage I of film formation of mixed polymer latexes. The influence of particle surface potential and Van der Waals interaction potential on type of packing and distribution obtained at the end of water evaporation stage were analyzed. The simulations were carried using Turq's algorithm (1977). Turq applied Brownian dynamics to

electrolyte solutions to see the influence of coulomb forces on self-diffusion coefficient of solute molecules. He generated an algorithm that represents the colloidal particle trajectories under the influence of several forces. Difference in surface potentials between the binary mixed particles determined the particle distribution. Small differences in surface potentials resulted in random particle distribution. For the case of higher surface potential difference, latexes with weaker electrostatic repulsions formed clusters in the final film. The model Qi Liao et al. (2000) developed did not take into account steric stabilization and hydrodynamic interactions.

Robbins et al. (1988) used molecular and lattice dynamics techniques to obtain phase diagram of colloidal systems in which particles interact through a repulsive screened coulomb potential (Yukawa Potential, Yukawa (1935)). Highly charged colloidal dispersions of monodisperse polystyrene particles were used in these studies. The phase diagram shows a transition from FCC to BCC with increasing temperatures, which is due to higher entropy associated with BCC structure.

It is well known that the classical Brownian diffusion theory developed by Einstein is applicable only to very dilute systems. But when the dispersion is concentrated, inter-particle forces and hydrodynamic interactions influence the diffusion of particles. Batchelor (1976) modified the classical theory to account for these effects, which become significant in the case of a latex dispersion, which is our present system under consideration.

From published prior research on modeling drying in latex coatings, it is evident that the models developed support some of the experimental observations already made. But the need for a comprehensive model that can be used to make a detailed parametric study to corroborate the experimental observations is evident. The next section gives a brief review of research that has been done on Stages II and III of film formation.

1.5 Stages II and III of Film Formation

Stage II is the particle deformation stage and is the most controversial of the three stages of film formation. For latex dispersions, particle deformation is thermodynamically favorable because of the decrease of total area of particle-water or/and particle-air interfaces. Despite a half century of research in this field, no consensus has yet been reached on the forces driving deformation. But four major theories have evolved during this period: (1) Dry Sintering Theory, (2) Capillary Theory, (3) Wet Sintering Theory, and (4) Surface Layer Theory.

According to Dry Sintering Theory proposed by Dillon et al. (1951), particle-air interfacial tension is responsible for particle deformation. One of the key assumptions in this theory is that drying is complete before deformation starts. However, this assumption is normally invalid because it is generally accepted that drying and deformation occur concomitantly.

According to Capillary Theory proposed by Brown (1956), film formation occurs when forces causing deformation (Van der Waals attraction, gravity, surface tension forces and capillary forces) dominate forces resisting deformation (elastic resistance and electrostatic repulsions). But Capillary Theory considered that only

capillary forces (arising due air-water interfacial tension) and elastic resistance forces are significant during deformation. The elastic deformation has been predicted using Hertz's theory for elastic spheres. Capillary Theory is the most popular one, though several modifications have been made by several researchers such as Mason (1973), Lamprecht (1980), and Eckersley et al. (1990).

According to Wet Sintering Theory proposed by Vanderhoff et al. (1970), polymer-water interfacial tension plays an important role in deformation. In the initial stage of deformation, when the two particles are in contact at only one point, the driving force for increasing contact zone is the air-water interfacial tension. This theory received little attention because of the difficulty in verifying experimentally.

According to the Surface Layer Theory proposed by Sheetz (1965), horizontal component of capillary force causes deformation of particles in the top layer, which results in the formation of a continuous film over the bulk latex. As water diffusion occurs through the film, a normal compressive force compresses the particles below and causes deformation.

Thus the driving force for particle deformation during Stage II is the major point of controversy, but other investigations carried on this stage will not be discussed in this thesis. Stage III of film formation is one of the less controversial stages. Voyutskii (1958) proposed that for deformation at end of second stage to be permanent, interdiffusion of polymer chains is needed. Researchers have studied this stage of film formation w.r.t influence of particle size, molecular weight, annealing conditions, etc on diffusion rate of polymer molecules.

1.6 Goal and System Description

The goal of the project is to develop a particle dynamics model that represents particle motion and aggregation associated with Stage I of film formation during drying of latex coatings. The model is then used to make parametric study and determine the drying conditions and particle properties required for obtaining long range ordering. The parameters tested include magnitude of random force, electrolyte concentration, rate of evaporation, particle size and initial particle distribution.

The latex coating modeled is a dispersion of hard-core polystyrene particles in aqueous solution. The developed model assumes pseudo-steady state (zero inertia) and the velocity and trajectory of each particle is determined by balancing the drag force on the particle with inter-particle repulsion, buoyancy, surface tension, Brownian force and Vander waals attractive forces. The model is solved numerically using forward Euler's method with automatic time step control. The cut-off length for interparticle interactions is used to divide the entire computational cell into subcells and thus improves the computational efficiency. This study uses areal density profiles, 2D and 3D plots to analyze particle ordering, packing orientation and layering phenomena that occur as water evaporates.

In this thesis, Chapter 2 discusses the various forces acting in colloidal systems and presents their governing equations. Chapter 3 shows the particle mechanics model developed using force balance and discusses the numerical aspects of the model. Chapter 4 presents the results obtained for a base case and also the results obtained from a parametric analysis. The thesis ends with a chapter containing conclusions and recommendations for further research.

Chapter 2: Forces Acting in Colloidal Systems

2.1 Introduction

This chapter discusses various forces that act in colloidal systems in general and in latex dispersions in particular. The system modeled is a dispersion of hard-core polystyrene particles suspended in an aqueous solution. The particles are charged and are in the size range of 100 nm to 1000 nm. As water evaporation occurs during stage I of film formation, the particles are in continuous motion under the influence of several forces. The main forces influencing the particle motion include Drag force, Buoyancy force, Brownian force, Surface Tension force, screened electrostatic repulsions, steric repulsions and Van der Waals attractions.

The model representing the particle motion during stage I is obtained by balancing the drag force with a sum of the other forces. This is possible by assuming that inertia of colloidal particles is negligible (*pseudo steady state* assumption) due to the sub-micron level size of colloidal particles. The assumption is called *psuedo steady state* because, although the acceleration is neglected, the velocities of the particles are not constant; i.e. the time-scale for acceleration of particles is much shorter than time-scale for changes in forces. The resulting model is a system of first order non-linear differential equations for particle position, which is easier to solve, compared to the second order equations obtained when considering the inertial term.

The sections in this chapter describe the origin and nature of the forces, and models for estimating the forces acting in colloidal systems. These forces form the basis of the model in Chapter 3 and the relative magnitudes of the various forces are discussed in this chapter.

2.2 Drag Force

In colloidal systems, a drag force arises due to the resistance of surrounding fluid to the motion of particles. The resistance is caused by the viscous shear of the fluid flowing over the particles and by the pressure difference between the upstream and downstream sides of the moving particle. The viscosity of the suspending fluid is a measure of resistance of fluid to particle motion. The drag force acts in a direction opposite to particle velocity, thus opposing the particle motion.

In colloidal suspensions in water, Reynolds number, which is the ratio of inertial force to viscous force, is small (10^{-6} for a one-micron size particle in water). For a Reynolds number of this magnitude the flow is accurately predicted by Stoke's flow. In this regime, the drag force is given by Stoke's equation:

$$\mathbf{F_D} = -6\pi\mu_w a\mathbf{V_i} \tag{2.1}$$

The above equation and all equations that represent various forces in this chapter are vector equations. All vectors used throughout the thesis are made bold-faced to distinguish them from scalars. $\mathbf{F_D}$ is the drag force vector acting on a particle i, μ_w is viscosity of suspending fluid (water), a is the particle radius and $\mathbf{V_i}$ is the vector representing particle velocity relative to the surrounding fluid. Equation 2.1 is valid only for a single sphere in a dilute medium. In using the above equation to model our system, it is assumed that the system considered is dilute and no inter-particle hydrodynamic interactions exist. This assumption is reasonably valid because the simulations used to investigate particle ordering and layering phenomena are carried out from an initial volume fraction of approximately 0.05 until volume fraction reaches approximately 0.6. For most part of the drying period (80%), the inter-

particle distances are more than a few particle radii to make hydrodynamic forces negligible.(Crocker, 1996).

The magnitude of the drag force is dependent on viscosity of the surrounding fluid, particle size and its velocity. The drag force has a higher magnitude for a fluid with higher viscosity and for larger particles. As particle velocity increases, the resistance to motion increases linearly resulting in higher magnitude of drag force.

2.3 Buoyancy Force

In colloidal systems, a buoyancy force arises due to the density difference between the particles and the suspending fluid. Based on whether the density of particle is lesser or greater than the suspending fluid, the buoyancy force acts either in vertically upward direction or in vertically downward direction respectively. In the predictions presented in this thesis, the particles are composed of polystyrene which has a density about 20% greater than water, resulting in downward buoyancy force.

The governing equation for the buoyancy force is dependent on whether the particle is completely immersed or partially immersed in the suspending fluid. When the particle is fully submerged, the buoyancy force is dependent only on particle size and density difference between particle and suspending fluid. The general equation for the buoyancy force is then given by:

$$\mathbf{F_B} = -\frac{4\pi}{3} a^3 \mathbf{g}(\rho_p - \rho_w) \tag{2.2}$$

$\mathbf{F_B}$ is the buoyancy force vector acting on the particle, ρ_p is the density of the particle, ρ_w is the density of suspending fluid (water in this case), **g** is acceleration due to gravity vector.

When the particle is partially immersed, there is an extra upward force due to the lower density of air compared to water. The governing equation for the buoyancy force when the particle is partially immersed is given by:

$$\mathbf{F_B} = -\frac{4\pi}{3} a^3 \rho_p \mathbf{g} \varsigma \tag{2.3a}$$

$$\varsigma = \left[\left(1 - \frac{\rho_a}{\rho_p} \right) - 0.25(1+\cos\theta)^2 (2-\cos\theta) \left(\frac{\rho_w - \rho_a}{\rho_p} \right) \right] \tag{2.3b}$$

ς is the parameter indicating the fraction of weight and buoyancy. ρ_a is the density of air, θ is the angle shown in Figure 2.1. It is the angle that line joining the center of the particle with the point at which the air-water interface meets the particle surface makes with the vertical direction.

The above equation is based on the assumption that the air-water interface remains horizontal up to the point of contact with the particle surface i.e. deformation of air-water interface is neglected. When the particle is partially immersed, the magnitude of the buoyancy force is not only dependent on densities of particle and suspending fluid but also on air density and on the extent to which the particle is submerged. When the particle is completely submerged, the angle θ is zero and the governing equation for the buoyancy force is then given by equation 2.2. Greater the difference in densities between particle and suspending fluid, greater is the magnitude of the buoyancy force. However, the particle size is on the order of micron and their volume is very small, so the buoyancy force is small compared to other forces and is generally neglected.

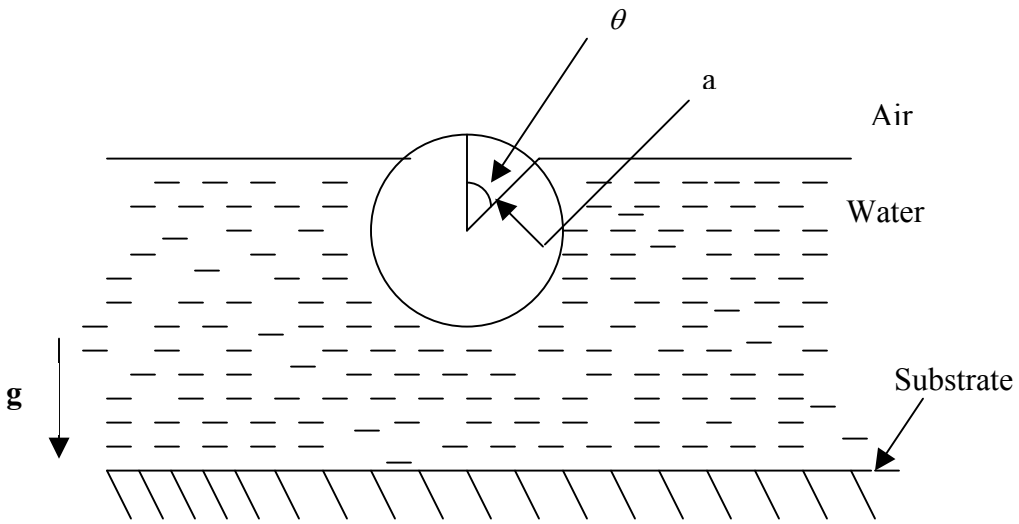

Figure 2.1 Particle partially submerged in water

2.4 Brownian (Random) Force

Colloidal particles, which are in the size range of 100 nm to 1000 nm, are under constant Brownian motion. This arises due to the thermal energy associated with the suspending fluid. The thermal energy of the fluid molecules causes them to undergo collisions with suspended particles, thereby resulting in random-walk motion. The magnitude of the Brownian force vector, **R**(t), causing the random-walk motion has no preferred direction, but has the following properties:

$$< \mathbf{R}(t) >= 0 \tag{2.4a}$$

$$< (\mathbf{R}(t))(\mathbf{R}(t')) >= \delta(t - t') \tag{2.4b}$$

The first property implies that the ensembled average of the random force has a zero magnitude. The second property implies that there is no correlation between the magnitudes of random force at time t and t'. $\delta()$ is the Kronecker Delta. The brackets, <…>, indicate an ensembled average, which is an average over many repeated measurements.

In this model, the magnitude of the random force is assumed to be Gaussian distributed. The assumption of a Gaussian distribution follows from the Central Limit Theorem, which states that the mean of any random variable with any distribution having finite mean and variance, tends towards a Gaussian distribution. The probability density function of Gaussian distributed random force R, is given by:

$$P(R) = \frac{\exp\left(\frac{-(R-\mu)^2}{2\sigma^2}\right)}{\sqrt{2\pi}\sigma} \tag{2.5}$$

$P(R)$ is the probability density function, μ is the mean of the random force and σ^2 is the variance of the random force. By definition (equation (2.4a)), μ is equal to zero.

Brownian diffusion of a particle can be described in terms of a coefficient, D, similar to Fick's diffusion coefficient called Brownian diffusivity. For an isolated sphere in a viscous medium, the Stokes-Einstein relation gives the Brownian diffusivity in terms of thermal energy and drag coefficient:

$$D = \frac{k_B T}{6\pi\mu_w a} \tag{2.6}$$

k_B is Boltzmann constant and T is temperature of the system. In the present model, the above equation is used as basis to obtain the variance of the Gaussian distributed random force. The variance of the Gaussian distributed random force is given by:

$$\sigma^2 = <\mathbf{R}^2> = \frac{12\pi\mu_w a k_B T}{t_s} \tag{2.7}$$

$\langle \mathbf{R}^2 \rangle$ is the ensembled average of the square of the random force and t_s is the time step during which the magnitude of random force **R** (t) is assumed to be constant. Equation 2.7 is obtained from the definition of Brownian Diffusivity and by considering Brownian motion as random walk (Van De Ven 1988).

The equation for the Brownian diffusivity given by Stokes-Einstein relation is derived only for an isolated sphere. The relation is valid for a dilute system where the particles do not have any hydrodynamic interactions.

Prior research shows how hydrodynamic interactions in concentrated colloidal systems affected Brownian diffusivity. Batchelor (1975) theoretically deduced the Brownian diffusivities for the case of two hydrodynamically interacting spherical particles in a deforming dilute homogeneous suspension and in a suspension with a particle concentration gradient. Batchelor divided the motion of spherical particles into two parts, the relative motion of the spheres and the motion of the center of mass of the two. Hydrodynamic interactions between particles cause suppression in the relative diffusivities and an enhancement in the diffusivities of center of mass. From Batchelor's observations it can be inferred that hydrodynamic interactions between particles become significant when interparticle distance becomes less than a few particle radii. This was also confirmed from the experimental observations made by Crocker (1996) using digital video microscopy.

In the present model developed for particle motion during water evaporation, the ordering and aggregation is followed for particle volume fractions ranging from an initial fraction of 0.05 to a final volume fraction of approximately 0.6. For most part of the drying period (80%), the inter-particle distances are of the order of few

particle radii where hydrodynamic interactions can be neglected. For the later phase of drying, when the inter-particle distances become less than few particle radii, hydrodynamic interactions become significant. But to include the hydrodynamic interactions in this model, we would have to take into account not only the interactions between two particles but also the interactions with all other particles, which are close to each other. This results in more complicated expressions for Brownian diffusivities, which is beyond the scope of this thesis. So hydrodynamic interations are neglected through the drying period.

As shown by Van De Ven (1988), the Brownian diffusivities of charged colloidal particles are influenced by parameters such as particle surface potential and thickness of double layer surrounding the particles. In the current model, this effect is also not considered, as we are interested only in the qualitative analysis of the ordering process rather than the quantitative results. In our model, the Brownian diffusivity is considered to be influenced only by the particle size, viscosity of the surrounding fluid and temperature of the system as given by equation 2.6. The diffusivity is higher for smaller particles suspended in lower viscous fluids at higher temperatures.

The random force vector used in the force balance for developing the model is obtained from cumulative distribution function (CDF) for Gaussian distribution, C(R), which is given by:

$$C(R) = \int_{-\infty}^{R} \frac{\exp\left(\frac{-(x-\mu)^2}{2\sigma^2}\right)}{\sigma\sqrt{2\pi}} dx \qquad (2.8)$$

This integral does not have a known analytical solution; however there are published numerical approximations to this integral. To evaluate the random forces to use in the force balance, an algorithm is needed to produce random numbers in a Gaussian distribution. In this thesis that is accomplished by using functions that produce uniformly-distributed random numbers between zero and one, then plugging those random numbers into the inverse of the cumulative distribution function. In this model, we used a numerical approximation for the inverse cumulative distribution function from Hastings (1955):

$$Q(R) = 1\text{-}C(R) = P \tag{2.9a}$$

$$l = \sqrt{\ln\left(\frac{1}{P^2}\right)} \tag{2.9b}$$

$$R_c = R_U\sqrt{\left\langle R^2\right\rangle} \tag{2.9c}$$

$$R_U = \left(l - \frac{C_0 + C_1 l + C_2 l^2}{1 + d_1 l + d_2 l^2 + d_3 l^3}\right) \tag{2.9d}$$

Where R_c is one of the components of the required random force vector **R** i.e. 'c' can be x, y, or z component, and R_U is the magnitude of a unit variant normally distributed random force. This process is repeated three times to get the three components of the random force vector. The values for the coefficients C_0 to d_3 are given in table 2.1.

The values required for the cumulative distribution function are obtained from a random number generator algorithm, ran1() (Press et al., 1992). A histogram (Figure 2.2) is also plotted for the random variable values obtained from the inverse

cumulative distribution function. As can be seen, the distribution is close to the Gaussian distribution, which it ought to be, thus verifying the correctness of the algorithm and the numerical approximation. The mean of the distribution is close to zero, agreeing with equation 2.4a.

Table 2.1 Values of the coefficients used in the approximation to CDF

Coefficients	Values	Coefficients	Values
C_0	2.515517	d_1	1.432788
C_1	0.802853	d_2	0.189269
C_2	0.010328	d_3	0.001308

A sample plot showing the magnitude of the Brownian force as a function of time is shown in Figure 2.3. The random force oscillates with time indicating that it can take positive or negative values with equal probability.

The magnitude of the random force is large compared to the screened columbic repulsions in the initial stages of water evaporation, when the repulsions are weak. As average interparticle distance decreases, the magnitude of the repulsions dominates over the random force. Thus Brownian motion of particles becomes relatively less significant as particle volume fraction increases. The magnitude of screened repulsions as a function of inter-particle distance is shown in section 2.6. The relative magnitudes of random force and eletrostatic repulsions are compared quantitatively in Chapter 3.

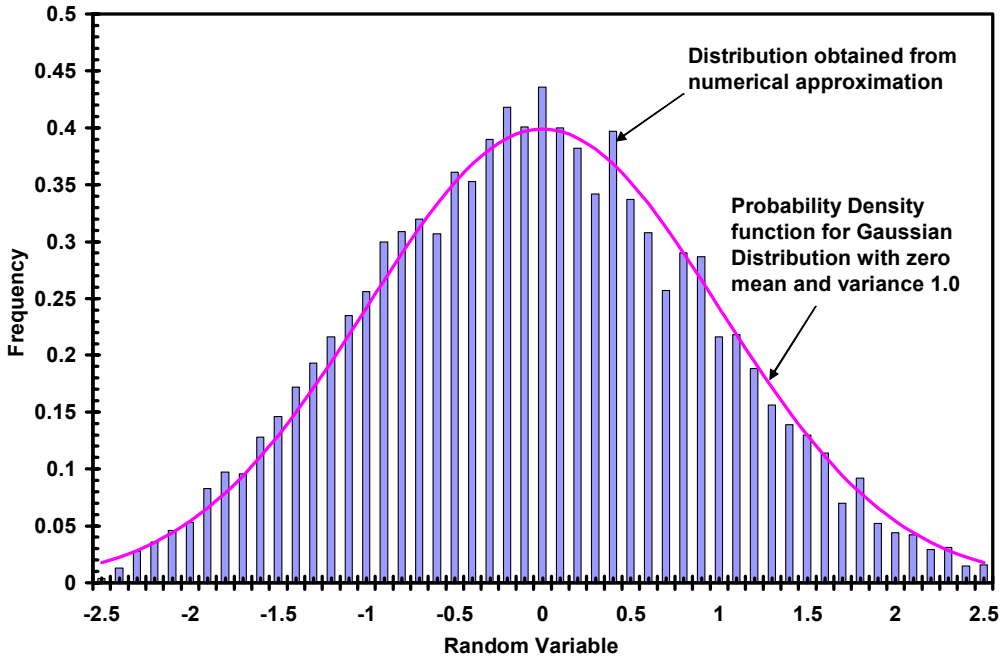

Figure 2.2 Plot comparing the distribution obtained from numerical approximation with PDF for Gaussian distribution. 10,000 random numbers were used to generate the histogram.

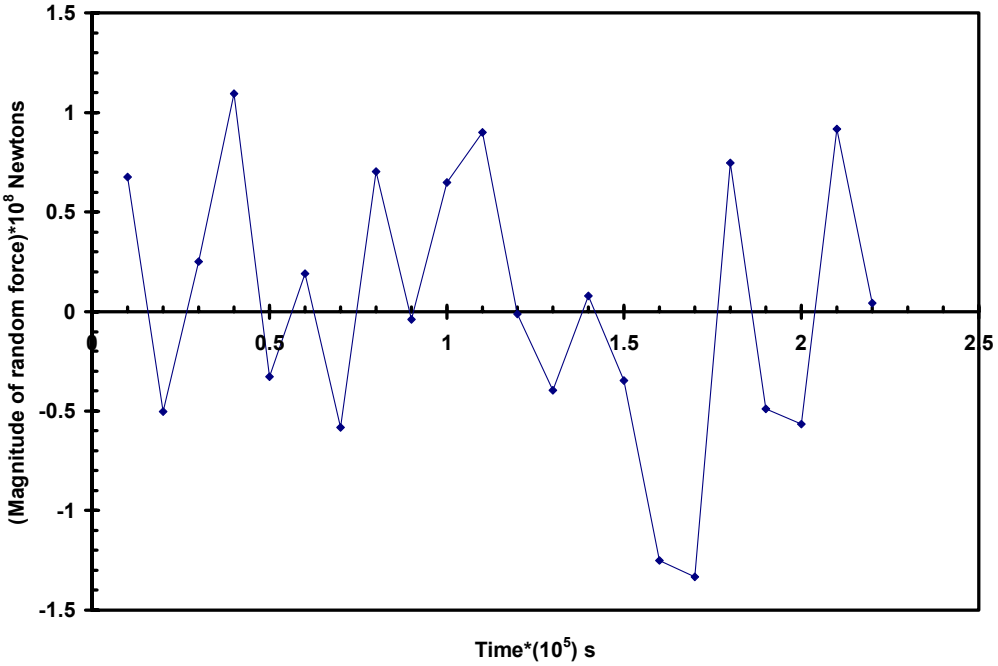

Figure 2.3 Random force obtained from numerical approximation as a function of time.

2.5 Surface Tension Force

In colloidal systems, the surface tension force acting on particles at air-water interface has the effect of trapping the particles within the liquid. When particles reach the air-water interface, force due to surface tension dominates over all other forces causing the particles to move along with the interface.

Surface tension force arises due to anisotropic attractive forces existing between molecules at the interface. The attractive forces existing between molecules away from the interface are isotropic because of the molecules surrounding them in all directions. But molecules at the interface do not have any molecules above them, resulting in higher transverse attractive forces and thereby causing anisotropy in attractive forces.

In the model developed, the governing equation for the surface tension force is obtained by making two assumptions. The main assumption is that surface tension acts tangent to particle surface along the curve of intersection between planar air-water interface and particle. The other assumption is that the air-water interface remains horizontal and planar until it meets the particle surface. Based on these assumptions, the governing equation for the surface tension force was obtained by integrating along the contact line of the interface and the particle. The governing equation gives the surface tension force vector $\boldsymbol{F_{ST}}$ in terms of air-water interfacial tension, σ, particle radius and distance between particle center and air-water interface:

$$\mathbf{F_{ST}} = -2\pi\sigma a\,\eta\mathbf{e_z} \tag{2.10a}$$

$$\eta = \left(1 - \left(\frac{Z_0}{a}\right)^2\right) \tag{2.10b}$$

$$Z_0 = X_s - X_z \tag{2.10c}$$

Z_0 is the distance between the particle center and air-water interface (Figure 2.4), $\boldsymbol{e_z}$ is a unit vector in the positive Z direction and η is the parameter indicating the extent of particle submergence. The value of η ranges from 0 (completely submerged) to 1 (half submerged). The negative sign indicates that the force acts in the negative Z direction (based on the reference frame shown in Figure 2.4). X_s is the position vector of air-water interface and X_z is the Z component of the position vector of the particle.

As can be seen from equation 2.10, the surface tension force is maximum when Z_0 is equal to zero i.e when the interface is exactly at the center of the particle. As Z_0 increases, the force due to surface tension decreases. When particles are completely immersed i.e when Z_0 becomes equal to or greater than the particle radius, the surface tension force becomes zero.

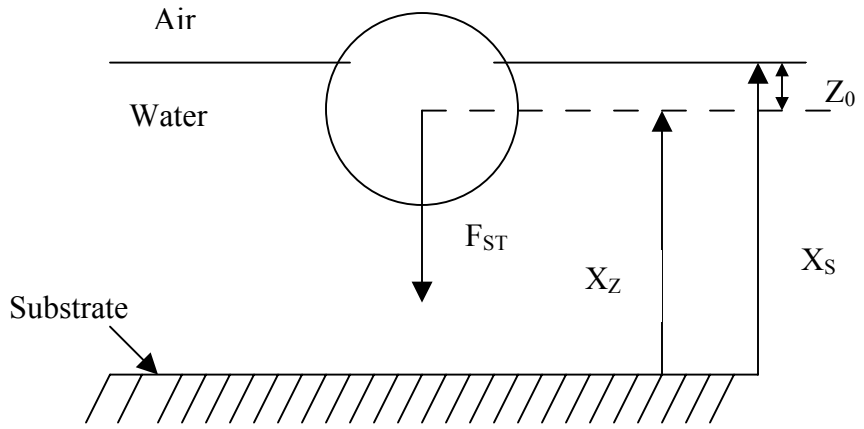

Figure 2.4 A partially submerged particle at the air-water interface

2.6 Screened Electrostatic Interactions

As was discussed in Chapter 1, latex particles acquire charge from the surfactants and emulsifiers present in the dispersion. The charges on the particle are necessary to avoid immediate coagulation. As latex dispersions are lyophobic in nature, the surface charge provides only kinetic stability and not thermodynamic stability. Given enough time, they finally form an aggregate. The electrostatic repulsions between the particles create an energy barrier that prevents immediate coagulation. The magnitude of the energy barrier can be controlled by varying the surface charge and also the electrolyte concentration. The higher the electrolyte concentration, the lower is the magnitude of the energy barrier.

Electrostatic repulsion in colloidal systems is quite different from ordinary columbic repulsion because of the presence of large number of highly mobile ions that effectively screen the interparticle interactions. Thus, the electrostatic interaction between charged colloidal particles involves not only the interactions between the

colloidal particles, but also the interactions between colloidal particles and the sea of ions surrounding the particles. These ions may be counter ions or co ions or ions due to an added electrolyte. The colloidal particles are called macro ions and other ions are called simple ions. Macro ions influence the distribution of simple ions, which in turn influence the interaction between colloidal particles resulting in screened repulsions.

Despite these complications, Deryagin, Landau, Verwey and Overbeek (1942) proposed a useful theory to account for the interactions between colloidal particles. Though the theory has its own limitations due its assumptions, the theory has been widely accepted and is used in the present model to predict electrostatic interactions between latex particles. As every particle has a finite surface charge, there should be an excess of ions of opposite charge in the solution to maintain overall electric neutrality of the system. The ions present in the solution are not uniformly distributed in the solution. The oppositely charged ions are attracted towards the ions present on the surface of particles. But the thermal motion of the ions counteracts this electrostatic attraction. Thus, the ions take an equilibrium position to balance the electrostatic interaction energy with the thermal energy. This results in a diffuse double layer of ions surrounding the particle: one layer formed from the charge on the surface of the particles and the other layer formed from the excess of oppositely charged ions present in the solution (Figure 2.5). Concentration of oppositely charged ions decreases as distance from the particle increases.

In the DLVO theory, the suspending fluid with its simple ions is treated as a simple electrolyte. The local electric potential, $\phi(r)$, depends on the concentration, $n_i(r)$, of ions of type *i,* each with charge, $z_i e$, through Poisson's equation:

$$\nabla^2 \phi(r) = -\frac{4\pi}{\varepsilon} \sum_{i=1}^{N} z_i e n_i(r) \tag{2.11}$$

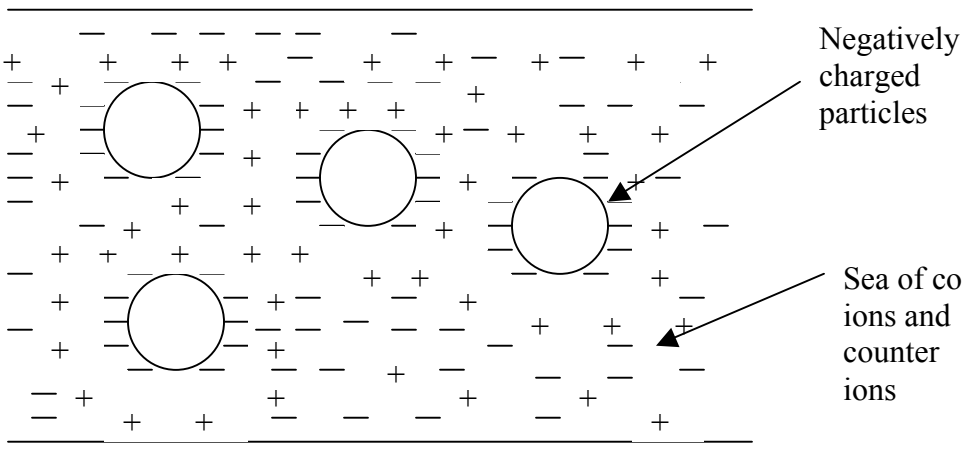

Figure 2.5 Diffuse Layer surrounding the charged particles

ε is the suspending fluid's permittivity. Here *i* includes all ions except the large colloidal particles. The ionic concentrations depend on the local electric potential in a nonlinear manner given by the Boltzmann distribution:

$$n_i(r) = n_i(0) \exp\left(\frac{-z_i e \phi(r)}{k_B T}\right) \tag{2.12}$$

$n_i^{(0)}$ is the ionic concentration for species *i* far from the spheres. Combining Poisson and Boltzmann equations gives the interaction between two colloidal particles. This equation cannot be solved analytically and has been solved numerically for simple geometries.

Deryagin, Landau, Verwey and Overbeek used the approximations from the Debye-Huckel theory of electrolyte structure, retaining only the linear term in the Taylor expansion of the exponential in the Boltzmann's equation, and invoked electroneutrality to obtain a linearized Poisson Boltzman equation:

$$\nabla^2 \phi = k^2 \phi \tag{2.13}$$

$$k^2 = \frac{4\pi}{\varepsilon k_B T} \sum_{i=1}^{N} z_i{}^2 e^2 n_i{}^{(0)} \tag{2.14}$$

k^{-1} is the screening length which gives the length scale over which the colloidal particles are screened by the ions surrounding them. As is evident, k is a function of the concentration of the ions surrounding the colloidal particles. Due to electric neutrality (the total charge due colloidal particles and surrounding ions is zero), it also depends on the concentration of the colloidal particles. When concentration of colloidal particles is large or when the concentration of surrounding electrolyte is small, k tends to be small and vice versa. Lower *k* implies a higher screening length and greater stability to coagulation. The value of *k* can be changed by varying the electrolyte concentration. As drying occurs, the electrolyte concentration increases resulting in increase in k value. But in the present model, k is assumed to be constant throughout the drying period.

Higher electrolyte concentrations result in a lower screening length which implies that the screening effect of the surrounding ions has increased. The decreased screening length has the effect of decreasing the electrostatic interactions between colloidal particles (Figure 2.6) i.e. the magnitude of the energy barrier that exists between particles to prevent rapid coagulation, decreases.

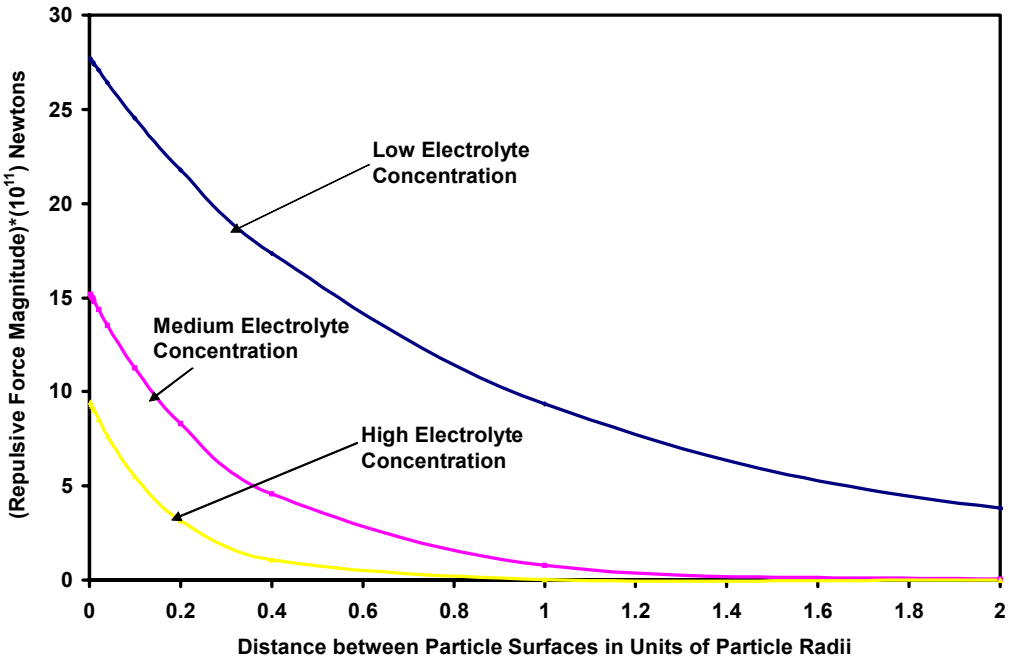

Figure 2.6 Screened electrostatic repulsions as a function of interparticle distance at low ($k = 10^6$), medium ($k = 5*10^6$), and high (10^7) electrolyte concentrations. Particle radius is 0.5 microns.

In Figure 2.6, the magnitude of the electrostatic repulsive force decreases with increase in the electrolyte concentration (i.e. with increase in k value). This is consistent with equations 2.13 and 2.14. Thus at low electrolyte concentrations, the repulsive forces are considerable even at larger inter-particle separations.

The Debye-Huckel theory, on which DLVO theory is based, is essentially a mean field theory. It considers a single charged particle as a reference and calculates how the rest of the ions distribute with regards to the influence of this reference particle. When the pair interaction is concerned, a charged probe particle is introduced into the system with the assumption that this probe particle does not effect the ionic distribution. This assumption is a reasonable one for a system with particles of low valency and at low concentration. This is because, when a highly charged

probe particle is present near another particle, the ionic distribution surrounding the latter particle is not only influenced by itself but also by the probe particle.

Apart from these assumptions, a few more assumptions were also made in the DLVO theory. Since the macro ions are so big, they are assumed to move much more slowly than simple ions. So the macro ions are treated as if they are fixed in space and the potential and the distribution of simple ions is worked out as a boundary value problem. Thus the effective macro ion interaction is obtained by linearly superposing the fields due to two spheres. The screened electrostatic interaction potential between two spherical particles is finally obtained using Derjaguin's approximation (1939). Derjaguin's approximation relates interaction energy per unit area between two flat plates and the interaction energy between two curved surfaces. This approximation is valid for a sphere made up of an infinite number of small parallel plates i.e. the particle radius is assumed to be much greater than the length of the flat plates. Derjaguin's approximation also requires the range of interaction (thickness of the double layer) to be much smaller than the particle radius i.e *ka* is much greater than one. The final equation for the pair interaction U(r) of two colloidal particles of radius 'a' and charge number Z, is given by:

$$U(r) = \frac{Z^2 e^2}{\varepsilon}\left(\frac{\exp(ka)}{1+ka}\right)^2 \frac{\exp(-kr)}{r} \tag{2.15}$$

r is the distance between the two particle centers.

DLVO theory despite its wide applicability in predicting interactions between charged colloidal particles has certain limitations, which need to be observed. The limitations arise mainly due to the following facts:

1. The DLVO theory is based on Debye-Huckel theory that involves a mean field approximation, which becomes invalid when the colloidal particle charges or concentrations become large.
2. The use of only the linear term in the Taylor's expansion of the exponential in the Boltzmann equation is valid as long as the electrostatic potential is smaller compared to the thermal energy, which is not true at distances close to the surface of highly charged particles.
3. The effect of the suspending fluid is taken only in the form of its dielectric constant and the structure of the solvent is not taken into account which may influence the interaction when the particles come as close as a few nanometers.
4. Volume exclusion effect for highly charged particles is not taken into effect.

Thus equation 2.15 is most valid when interparticle distances are greater than the screening length, the colloidal particles are not highly charged and the suspension is of low to moderate concentration.

In recent times there is growing evidence that attractive interactions exist between like charged particles under certain conditions. When particles are confined between two glass plates or when placed near a single glass plate, a long-range attractive interaction potential was observed while DLVO theory predicts pure repulsion. The inherent assumptions in the DLVO theory and hydrodynamic interactions near a wall (Squires et. al. (2000)) have been proposed as the possible reasons for the inability of DLVO theory to predict the attractive interactions.

An alternative theory proposed by Sugami and Ise (1984) has a long-ranged attractive tail in addition to the intermediate range screened electrostatic repulsion. This theory was successful in accounting for the attractive interactions between particles confined to spaces closer to walls but could not represent the repulsive interaction in case of isolated spheres. Bowen and Sharif (1998) solved non-linear Poisson-Boltzmann equation numerically for two spheres placed on the axis of a charged cylindrical shell. Using their approach to solve the non-linear equation for two spheres near a charged wall (substrate) and obtaining pair-wise interaction potential between particles is beyond the scope of the thesis. As the model developed using DLVO theory is used to make a qualitative analysis of particle ordering and layering in the volume fraction range of 0.05 to 0.6, the average interparticle distance is almost always greater than a few particle radii. Under these conditions, the system is always in the applicability regime of the DLVO theory.

The magnitude of force vector for screened columbic interactions, F_{DLVO}, is obtained by taking the derivative of the pair-interaction potential obtained from equation 2.15:

$$F_{DLVO} = -\frac{dU(r)}{dr} \tag{2.16a}$$

$$F_{DLVO} = \frac{Q^2}{\varepsilon}\left(\frac{\exp(ka)}{1+ka}\right)^2 \frac{\exp(-kr)}{r^2}(kr+1) \tag{2.16b}$$

Q is the surface charge on particle. In deriving the above equation, an assumption of equal particle size and surface charge is made. As can be seen from equation 2.16b,

the magnitude of the screened interaction force vector decays more rapidly compared to simple columbic repulsions, due to the presence of the exponential term.

Assuming that the pair interaction forces can be added together for a large number of particles to get the net DLVO force on a particle, the screened columbic repulsion force $\mathbf{F_{DLVO}}$ written in the vector notation is given by:

$$\mathbf{F_{DLVO}} = \frac{Q^2\beta}{\varepsilon a^2}\boldsymbol{\omega} \tag{2.17a}$$

$$\beta = \frac{1}{\left(1+\bar{k}\right)^2} \tag{2.17b}$$

$$\boldsymbol{\omega} = \sum_{j=1}^{N} \frac{\left(\bar{k}\bar{r}_{ij}+1\right)}{\bar{r}_{ij}^{\,2}} \exp\left(-\bar{k}\left(\bar{r}_{ij}-2\right)\right)\mathbf{e_{ij}} \tag{2.17c}$$

Here the over bar indicates that the term is scaled WRT the particle radius 'a'. $\boldsymbol{\omega}$ is a dimensionless force vector in units of $\frac{Q^2\beta}{\varepsilon a^2}$. It is the sum of inter-particle repulsion forces. $\mathbf{e_{ij}}$ is unit vector joining centers of particles 'i' and 'j'.

2.7 Van der Waals Attractive Interactions

Vander Waals attractive forces also known as London dispersion forces are weak forces that exist between uncharged molecules as a result of induced polarity. These forces become significant when the particles are very smaller in size and when the distances are in the nano level.

The origin of Vander Waals attractions may be related to the fluctuations in the charge distribution of atoms. As the electron cloud in an atom is in continuous motion, there are moments when the electrons are crowded at one side giving

temporary polarity to the atom. This induces temporary polarity to the adjacent atom by repelling the electron cloud. According to the theory proposed by London (1930), the attractive forces between atoms are additive in nature. Because of this nature, the attractive interaction between two colloidal particles containing many atoms is appreciable, despite the force between two atoms being weak.

The Vander Waals attractive forces between atoms are very short ranged, evident from the fact that they decrease with the seventh power of interparticle distance. Because of their additive nature, attractive forces between colloidal particles decrease much more slowly. Hamaker (1937) derived an expression for the attractive interactions between colloidal particles. For two particles of radii a_1 and a_2 separated by distance r, the Vander waals potential energy $U_{vw}(r)$ is given by:

$$U_{vw}(r) = \frac{-A}{6}\left(\frac{2a_1a_2}{r^2 - 4a_1a_2} + \frac{2a_1a_2}{r^2} + \ln\frac{r^2 - 4a_1a_2}{r^2}\right) \qquad (2.17)$$

A is the Hamaker constant which has values generally in the order of 10^{-20} Joules. A is given by $A = (\sqrt{A_{11}} - \sqrt{A_{22}})^2$; A_{11} is the Hamaker constant for the particles and A_{22} is the Hamaker constant for the medium. For water its value is $3.7*10^{-20}$ Joules and for PMMA and PS, the values are $7.11*10^{-20}$ and $6.58*10^{-20}$ Joules.

For two particles of same size and when distance between particle surfaces is much less than the particle radii, we can obtain a useful approximation for equation 2.17:

$$U_{vw}(r) = \frac{-Aa}{12}\frac{1}{r - 2a} \qquad (2.18)$$

As can be seen from the above equation, the attractive interaction potential decreases as the reciprocal of the inter-particle distance. When the attractive potential is combined with the repulsive potential obtained from DLVO theory, it can be observed that, the attractive interactions are significant compared to the screened repulsions at very close distances (at few nanometer distances) as shown in Figure 2.7. At intermediate distances, the repulsive interactions are dominant and at very large distances, the inverse term dominates over the exponential term, resulting in the domination of the Vander Waals attractive interactions. As can be seen from figure 2.7, the attractive force (negative in sign) dominates until 2 nm inter particle surface separation resulting in total negative force. Beyond 2 nm, the positive repulsive forces are dominant resulting in positive total force. At very large separations, the total force again reaches negative value due to dominance of Van der Waals attractions, though the magnitude is very negligible.

In the present model developed, Vander Waals attractions are not considered because of their short-range nature. In our simulations, the particles never get to such close distances where Vander Waals interactions become significant. The average inter-particle distances at most times are greater than a few particle radii.

2.8 Other Forces

Apart from the above-mentioned forces, there are other forces that exist in colloidal systems. When the substrate on which the latex dispersion is applied is charged, the particles would interact not only with each other but also interacting with the substrate. The particles could have attractive or repulsive interactions with the substrate depending on the charge of the substrate. In the present model, the substrate

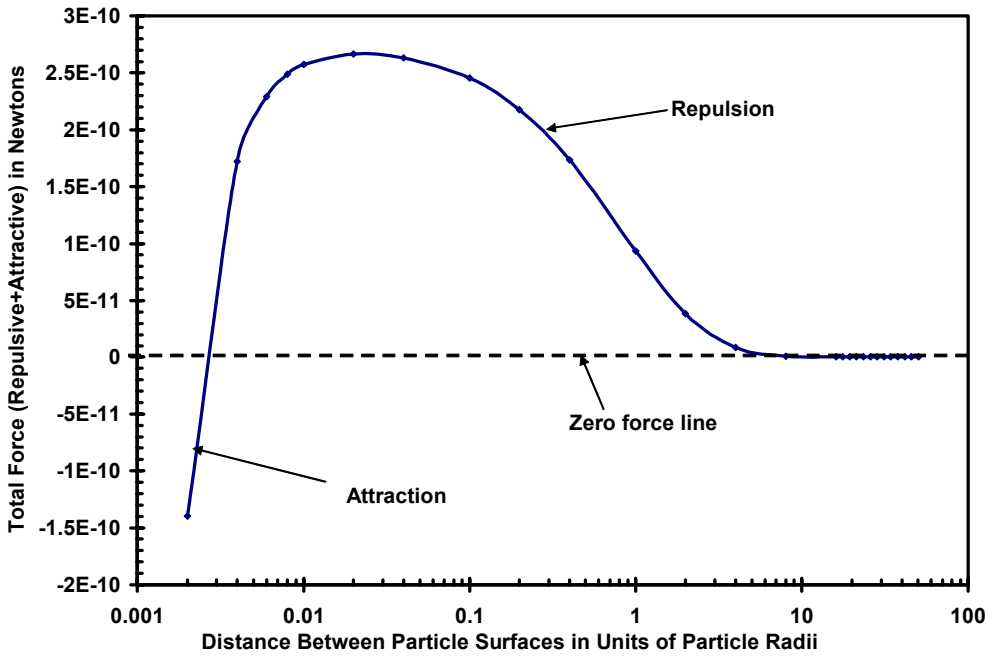

Figure 2.7 Total force (Repulsive and Attractive) as a function of the distance between particle surfaces. k = 10^6 and particle radius is 0.5 microns.

is assumed to be neutral and thus the particles do not have columbic interactions with the substrate. Once the particles hit the substrate or contact each other, they may undergo elastic deformation depending upon the nature of the substrate. In the present model, such deformations were neglected, but once they hit the substrate, their velocity in the z-direction (vertical direction) was assumed to be zero and the particles would move only in the x and y directions.

In this chapter, various forces that play significant role in colloidal systems were discussed along with their physical origin and the governing equations. The conditions under which one force dominates over other force were also presented. The next chapter of the thesis discusses the particle dynamics model developed from a force balance on a particle and the numerical aspects of the model.

Chapter 3: Numerical Model

3.1 Introduction

This chapter discusses the development of particle dynamics model from a balance of various forces discussed in Chapter 2 and the numerical technique used for carrying out the simulations. The model predicts the colloidal particle motion as water evaporation occurs. As was discussed in Chapter 2, water evaporation from a latex dispersion results in an increase in the particle volume fraction and a decrease in average interparticle distance. The initially dilute dispersion (particle volume fraction of approximately 0.05) finally turns into a concentrated dispersion. In the present study, the numerical simulations are carried out until the particle volume fractions reach about 0.6. During this period, the colloidal particles are in continuous motion under the influence of independent forces or forces due to interactions with other particles and solvent molecules.

The model produces a large system of non-linear ordinary differential equations, and is solved numerically by forward Euler time integration. Section 3.2 discusses the particle dynamics model development using force balances on particles. Section 3.3 presents the scaling technique used for making the model dimensionless. Section 3.4 discusses the methods used to improve the computational efficiency of the simulations. In particular, the method in which the cut-off length for screened repulsions was used to divide the computational cell into sub cells will be discussed. Section 3.5 presents the time integration technique used. Finally, an analytical solution for the simple case of two completely submerged particles interacting via

ordinary columbic repulsions that was used to make an initial verification of the numerical solution is presented in Section 3.7.

3.2 Model Development

The particle dynamics model in this thesis predicts colloidal particle motion as water evaporation occurs in latex dispersions. The model enables predicting the effect of operating parameters on particle ordering and layering. The motion of a single particle is governed by Newton's equation of motion for a particle.

$$\frac{4}{3}\pi a^3 \rho_p \frac{d^2\mathbf{X_i}}{dt^2} = \mathbf{F_{Drag}} + \mathbf{F_{DLVO}} + \mathbf{F_{Brownian}} + \mathbf{F_{ST}} + \mathbf{F_{Buoyancy}} \qquad (3.1)$$

Equation 3.1 is commonly used in Molecular Dynamics, Discrete Element Method simulations, etc. for modeling systems containing discrete bodies. The term on the left hand of the equation is the particle inertia, which is mass times acceleration of the particle. Bold font indicates that the variables are vector quantities. $\mathbf{X_i}$ is the position vector of a particle 'i'.

A key assumption in the model in this thesis is that the particle motion is considered to be in psuedosteady state i.e. particle inertia is negligible compared to other forces. This simplifying assumption results in a system of first order non-linear differential equations instead of second order equations. This pseudo-steady assumption reduces computational effort without affecting the accuracy of the results. The assumption is valid in the current model because the surrounding fluid is water and the particles (colloidal) on which force balance is made are very small in size with negligible mass. It is termed pseudo-steady assumption because, though the acceleration term is neglected in developing the equation for particle notion, the

velocity is not constant. Because of the forces acting due to interactions with several particles, the velocity of a particle does not remain constant. The particles are in continuous complicated motion.

By neglecting inertia, the second order term in Newton's equation of motion (equation 3.1) drops out. The particle velocity is the first derivative of the particle position, so the resulting equation of motion is first order:

$$6\pi\mu_w a\frac{d\mathbf{X_i}}{dt} = \mathbf{F_{DLVO}} + \mathbf{F_{Brownian}} + \mathbf{F_{ST}} + \mathbf{F_{Buoyancy}} \tag{3.2}$$

This implies that at all times, the drag forces on a particle are exactly balanced by the inter-particle forces, buoyancy, surface tension and random forces.

In the present model, all the forces and particle positions were treated as vectors with each vector having components in x, y and z directions. The entire latex dispersion system was considered to consist of repetitive unit cells which extend through the thickness of the coating from top to bottom. The top view of such a repetitive system is shown in Figure 3.3. Periodic boundary conditions are assumed in the transverse (x and y) directions. In this assumption, the total number of particles in a single cell is always constant. So, when particles leave through one side of the cell, they enter in the opposite side. However particles can not pass through the top or bottom surfaces of the unit cell. The reference x, y and z planes and the reference origin from which the particle displacements were measured are shown in Figure 3.1. In the figure, $\mathbf{X_i}$ is the position vector representing the position of particle *i*.

Making a force balance in each direction on a particle 'i' gives the differential equation representing the corresponding component of the particle position vector as a function of time. The force balances in the x and y directions are the same but are

different from z direction balance. Surface tension force and buoyancy force acts only in the z direction. In the x direction, Newton's equation of motion (equation 3.2) can be modified as:

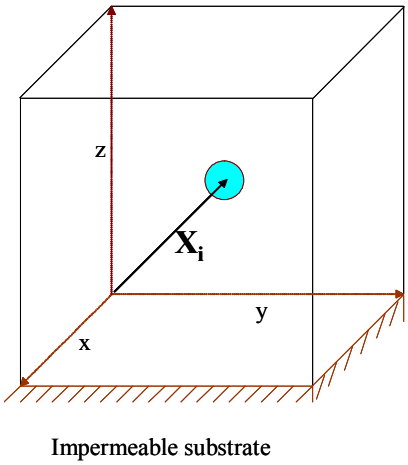

Figure 3.1 A 3D computational cell showing the reference directions and the particle position vector $\mathbf{X_i}$

$$6\pi\mu_w a\frac{dX_{i,x}}{dt} = F_{DLVO,x} + F_{Brownian,x} \tag{3.3}$$

$$6\pi\mu_w a\frac{dX_{i,x}}{dt} = \frac{Q^2\beta}{\varepsilon a^2}\omega_{\mathbf{x}} + R_{i,x} \tag{3.4}$$

$X_{i,x}$ is the x-component of the position vector of particle *i,* $R_{i,x}$ is the x-component of the random force vector acting on particle *i*. This is obtained from equation 2.9c. ω_x is the x-component of the sum of inter-particle repulsion forces vector, ω, given by equation 2.17c. The differential equation representing the particle motion in the y direction is also the same. The z-component of Newton's equation of motion can be written as:

$$6\pi\mu_w a\frac{dX_{i,z}}{dt} = F_{DLVO,z} + F_{Brownian,z} + F_{ST} + F_{Buoyancy} \tag{3.5}$$

$$6\pi\mu_w a\frac{dX_{i,z}}{dt} = \frac{Q^2\beta}{\varepsilon a^2}\omega_z + R_{i,z} - 2\pi\sigma a\eta - \frac{4\pi}{3}a^3\rho_p g\varsigma \tag{3.6}$$

X_{iz} is the z-component of the position vector of particle *i.* The surface tension and buoyancy terms are obtained from equations 2.10a and 2.2a of Chapter 2 respectively. The other parameters were defined in chapter 2. When the particle is fully submerged, surface tension term does not act on the particle, and η is equal to zero. Thus the surface tension exists only when:

$$\left|X_s - X_z\right| < a \tag{3.7}$$

i.e the distance between air-water interface and particle center is less than particle radius. This is shown in Figure 2.4. When the particle is fully submerged, the buoyancy term is obtained from equation 2.3 instead of equation 2.2a, and then $\varsigma = \frac{\rho_p - \rho_w}{\rho_p}$.

3.3 Scaling

In modeling, scaling is used to eliminate terms in the governing equation whose magnitudes are small compared to other terms. After scaling, the equation becomes dimensionless. Scaling is implemented by choosing a proper scaling parameter for each of the variables involved in the equation. In the present model, in each equation, the particle position vector and time are the two variables present. The following are the scaling parameters used for making the two variables dimensionless:

$$\boldsymbol{\chi} = \frac{\mathbf{X}}{a} \; ; \; \tau = \frac{t}{t_0} ; \; t_0 = \frac{a}{V_S} \tag{3.8}$$

$\boldsymbol{\chi}$ is dimensionless particle position vector, τ is dimensionless time, t_0 is scaling parameter for time and V_S is velocity of air-water interface. Particle radius is used for scaling the particle position vector. The scaled equation representing particle trajectory in z direction is given by:

$$\frac{d\chi_{i,z}}{d\tau} = \frac{1}{6\pi\mu_w a V_S}\left[\frac{Q^2\beta}{\varepsilon a^2}\omega_z + R_{i,z} - 2\pi\sigma a\bar{\eta} - \frac{4\pi}{3}a^3\rho_p \mathrm{g}\bar{\varsigma}\right] \tag{3.9}$$

$\chi_{i,z}$ is the z component of scaled position vector of particle *i*. $\bar{\eta}$ and $\bar{\varsigma}$ are the scaled versions of η and ς . The scaled equations in x and y directions are the same as in z direction but without buoyancy and surface tension terms. Estimating the coefficients of the force terms involved in the equation gives an idea on the magnitude of different forces. The buoyancy coefficient has the least magnitude and can be neglected. When particle was at the interface, the surface tension coefficient dominates over all the other coefficients.

3.4 Computational Cell and Cut-off Length

As the number of particles in a real system is quite large compared to that in a simulation, a unit cell is chosen for carrying out the simulations. The properties of the unit cell and two dimensional nature of the periodicity assumption were mentioned in Section 3.2. Even in the single cell chosen, evaluating the interactions of each particle with all other particles at every time step is computationally intensive. In order to reduce the computational load, a cut-off length was determined in which the inter-

particle forces are significant. For inter-particle separations greater than the cut-off length, inter-particle forces are negligible.

The model cell was divided into sub cells such that the size of each sub cell is greater than the cutoff length. Thus each particle interacts with only the particles in its sub cell and with those in the nearest neighboring sub cells. When the particle is in a sub cell which is on the boundary of the computational cell, the concept of periodicity is used is used to find appropriate adjacent sub-cells.

The cut-off length was determined by comparing the magnitude of all the forces acting on each particle at different inter-particle distances. The distance at which the electrostatic repulsion force becomes considerably negligible compared to other forces is taken to be the cut-off length. Figure 3.2 shows the plot of force versus distance (distance between particle centers) curve for a single particle.

As buoyancy force is always negligible compared to other forces, it was not included in the plot. As surface tension force anyway dominates over all other forces when it acts, it was also not considered. The main forces considered were screened columbic repulsive force, random force and drag force. The repulsive force was plotted for three different k values (inverse screening lengths). The particle radius was taken as half a micron, which is the base case particle size. As drag force is dependent on the particle velocity, which cannot be determined without considering the interactions with other particles, the velocity of the air-water interface, which is typically less than the particle velocity, is used to calculate the drag force.

As can be seen from the plot, drag force was the smallest of the forces other than the repulsion force. So cut-off length was taken as the distance at which the

magnitude of the screened repulsions become negligible (one-tenth) compared to the drag force. From the plot it can be seen that this distance is approximately four times the particle radius for high k value (10^7 /m), six times the particle radius for medium k value ($5*10^6$ /m) and almost 17 times the particle radius for low k value (10^6 /m). Thus the cut-off length increases as k value is decreased. This is expected because,

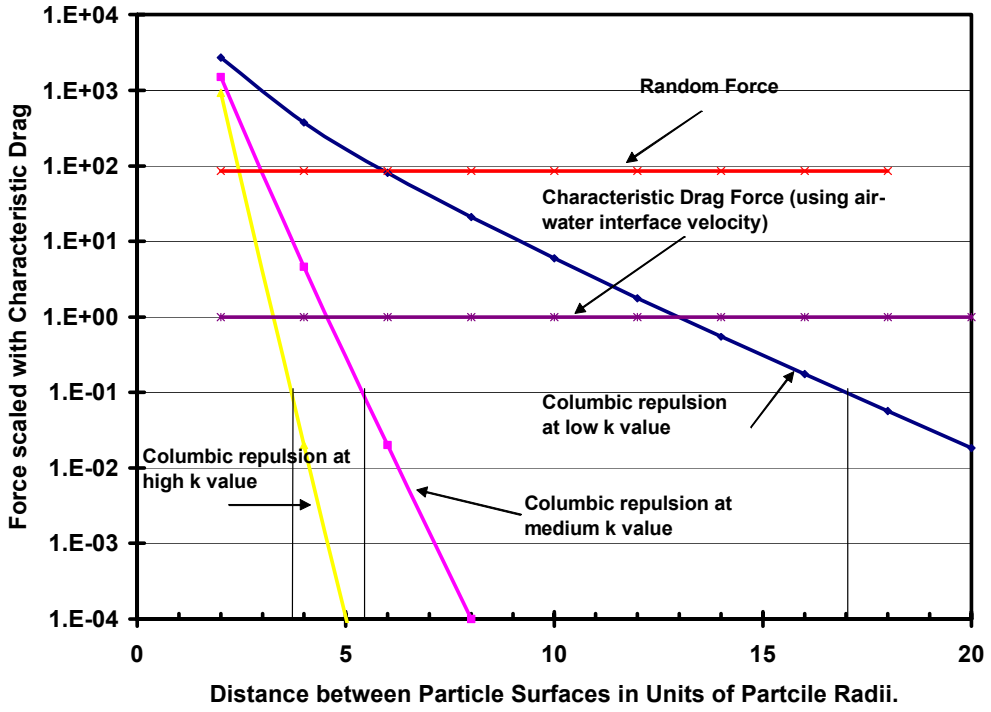

Figure 3.2 Force versus Distance (scaled) curve used for determining cut-off length for three different k values: 10^7 /m; $5*10^6$ /m; 10^6 /m. The force is scaled WRT characteristic Drag force.

lower k value indicates higher electrostatic repulsions and thus the distance at which they become negligible is higher. Thus for high k values, a cut-off length of 4 particle radii would be sufficient.

In the present model, the dimensions of the computational cell were taken as multiples of the particle radius (half a micron). The size of the cell in x and y

directions was taken as 20 times the particle radius and the initial size in the z direction was taken as 50 times the particle radius. As the size of the computational cell is not fixed in the z direction, the cell is divided into sub cells only in the x and y directions. Using the cut-off length of 4 particle radii, the cell can be divide into sub cells in such a way that their x and y dimensions are 4 times the particle radii. A schematic of the computational cell along with sub cells is shown in figure 3.3. In the figure, a particle in any sub cell experiences force from the particles in the nearest 8 sub cells. For example, particle 1 experiences forces due to particles in sub cells, 2, 6, 7, 5', 10', 21', 22' and 25'''. The sub cells with primed numbers indicate that they belong to the computational cell neighboring to the reference computational cell.

As the sub cells extend in x and y directions, the total number of sub cells in a cell is given by:

$$N_{SC} = \frac{X_C Y_C}{X_{SC} Y_{SC}} \tag{3.6}$$

N_{SC} is the total number of sub cells, X_c and Y_c are the sizes of the computational cell in x and y directions respectively, X_{SC} and Y_{SC} are the sizes of the sub cell in x and y directions. The sizes of the sub cell are chosen such that N_{SC} is an integer. Thus in Figure 3.3, there are 25 sub cells, the number obtained using a cut-off length of *4a*. The size of each sub cell depends on the cut-off length, which in turn is dependent on the k value (electrolyte concentration).

3.5 Time Integration

The system of dimensionless non-linear differential equations obtained from the model is solved numerically using explicit Euler's method. We cannot solve the system of equations analytically except for the simple case of two particles

completely submerged. Both Euler's and 4-stage Runge Kutta methods were used to solve the model. The increased accuracy obtained by using the 4-stage Runge Kutta method was negligible, but the computational cost grew by more than 4 magnitudes using the same method. So, explicit Euler's method was used for results in this thesis.

Time step size control is an important aspect in numerical modeling. The time step should be sufficiently small to track continuous motion of the particles. Too small time step size slows down the simulations. Thus there is a need for controlling the time step size and so variable time step size is used rather than using fixed time step. Two different criteria were used to control the time step size.

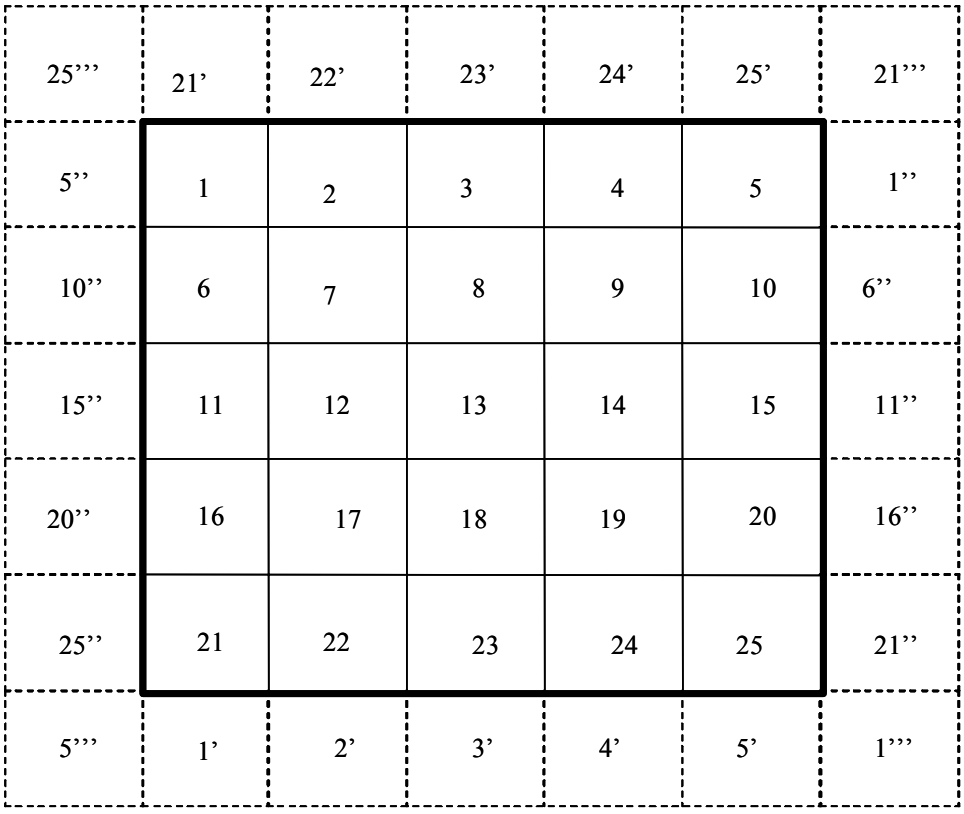

Figure 3.3 A schematic of a Computational cell with 25 sub cells. The sub cells with dashed borders and primes indicate sub cells that are outside of the reference computational cell.

The time step was controlled using a predictor-corrector scheme depending on whether the random Brownian force is active or not. For simulations in the absence of the random force, the magnitude of the component of particle position vector at every time step was predicted from the previous two time steps, using linear extrapolation. This value was compared with actual value obtained at that time step, and the difference obtained between the actual and predicted values was determined for every particle. The maximum of those differences for all particles and directions was then determined. The maximum was then compared with a base error criterion. If the maximum was greater than the error criterion, the time step was reduced by half and the calculation was repeated until the maximum was less than the error criterion. If the maximum obtained was less than one-tenth of the error criterion, the time step size was doubled to increase the computational speed.

When the simulations were carried in the presence of a random force, extrapolation could not be used to predict the new value at a given time step because of the influence of the random force. Instead, the displacement of a particle in a time step was constrained to be less than a set distance, a fraction of its radius. In the results of this thesis, half the particle radius was taken as the maximum displacement a particle can undergo during a time step. If the maximum of all displacements was less than one-fifth of the criterion, the time step was doubled to increase the computational speed. From the simulations, it was found that using an automatic time step controller improves the computational efficiency of the simulations.

3.6 Initial Particle Distribution

Practically, in latex dispersions the particles are more or less randomly distributed. So in the present simulations, the initial particle distribution is obtained using a random number generator. A random number generator is used to generate the x, y and z co-ordinates of all the particles with a restriction that no particles are closer than a specified tolerance of three particle radii.

Figure 3.4 shows three dimensional and two dimensional plots of the initial distribution of the particles. These plots show no particular ordering or arrangement, conforming to the general observation in practical situations.

a) b)

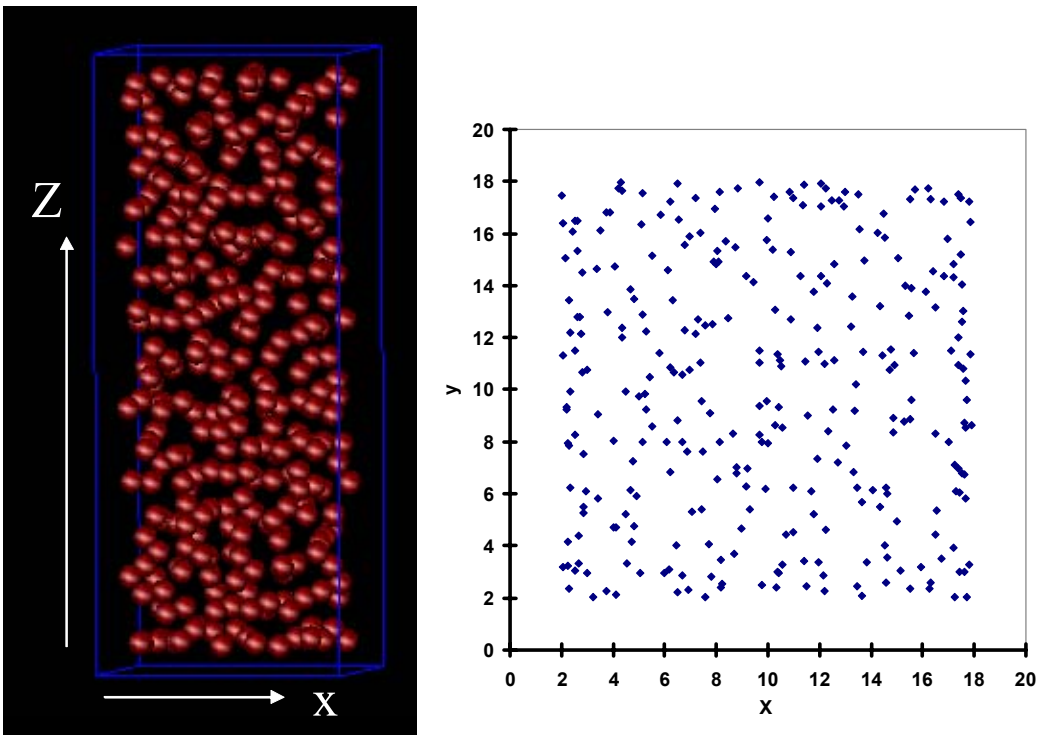

Figure 3.4 a) 3D image of side view, and b) 2D plot of top view of initial particle distribution.

No particles were taken at distances less than two particle radii form the boundaries of the computational cell. This was used in order to maintain the periodicity and also to start with initial distribution having at least four radii inter-particle distance. In real systems, the particles are randomly distributed throughout the cell. So, in Chapter 4, the particle ordering that occurs with decrease in water volume fraction is followed starting from $\tau = 2$ (when the particles are distributed throughout the computational cell) instead of $\tau = 0$. Furthermore, results in Chapter 4 show that the initial particle distribution has no influence on the ordering phenomena occuring during Stage I.

3.7 Analytical Verification

The accuracy of the numerical solution was verified against an analytical solution for the simple case of two particles submerged completely in the dispersion under the influence of ordinary columbic repulsions and in the absence of random force. In this simple case, the term for columbic repulsions in equation 3.9 now becomes:

$$\overline{\mathbf{F_{CR}}} = \frac{Q^2}{4\pi\varepsilon}\frac{1}{a^2\overline{\mathbf{r^2}}} \tag{3.10}$$

Where $\overline{\mathbf{F_{CR}}}$ is simple columbic force vector scaled with particle radius, ‘a’.

Then the first order linear differential equation representing the vector joining the two particle centers written in dimensionless form (Modified form of equation 3.9) is given by:

$$\frac{d\bar{r}}{d\tau} = \frac{1Q^2}{12\pi^2\mu_w V_s a^3 \varepsilon}\frac{1}{\overline{r^2}} \tag{3.7}$$

This was solved analytically and compared with the numerical solution obtained from Euler's time integration. A plot of cube of dimensionless inter-particle distance $\bar{r}$ against dimensionless time is made for both analytical and numerical solutions (Figure 3.5). As is evident from the figure, the numerical solution is in good agreement with the analytical solution.

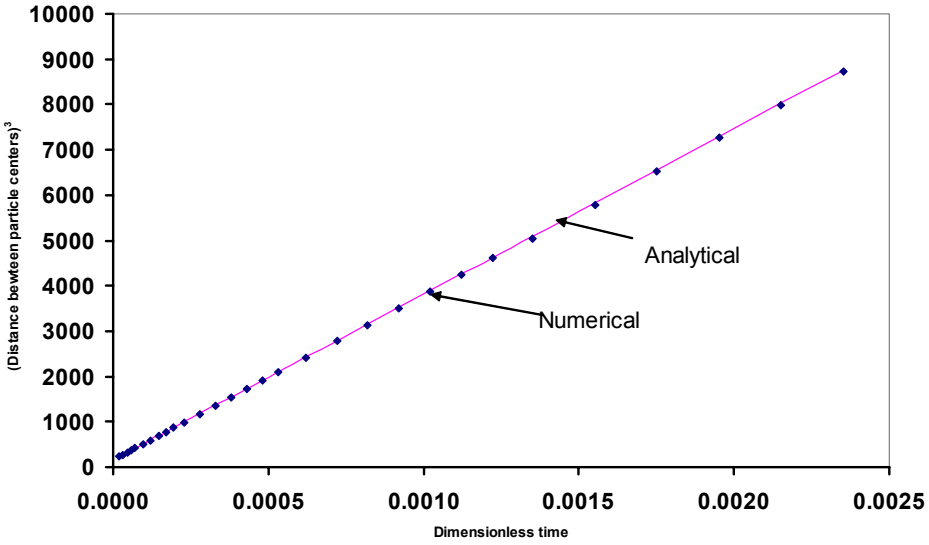

Figure 3.5 Comparison of analytical and numerical results for the simple case of two particles interacting via simple columbic repulsions in the absence of surface tension and random forces.

3.8 Summary

In this chapter a detailed outline of the model development for particle motion along with the numerical aspects of the solution was discussed. It was shown that the initial particle distribution obtained from random number generator showed no particular ordering or arrangement. An analytical solution for the simple case of two completely submerged particles was presented. In the next chapter, some other ways of verifying the numerical solution will be discussed. Then a detailed discussion on the base case and parametric analysis made on particle ordering and layering

phenomena observed as water evaporation occurs will be presented. The influence of random force, rate of evaporation, particle size, initial volume fraction, screening length and other parameters will be discussed.

Chapter 4: Predictions of Particle Ordering During Drying

4.1 Introduction

This Chapter contains the results of particle mechanics simulations and a parametric study on particle ordering and layering phenomena during film formation. The results are first presented for a *base case* which corresponds to a system of poly-styrene particles suspended in water. The values of the parameters used for the *base case* are listed in Table 4.1. The parameters varied in the parametric study include magnitude of random Brownian force, rate of evaporation, particle size, electrolyte concentration, and surface charge density. The goal of the analysis presented in this chapter is to understand the evolution of particle layers and packing structure upon drying during Stage I. The results are analyzed using 2D and 3D images of particle positions, and areal particle density distributions. Also, to verify the accuracy of the predictions, the influence of initial distribution on particle ordering and layering is presented.

4.2 Description of Simulations

This chapter discusses the evolution of a latex system from a random dispersion of particles to an ordered packing structure as water evaporation occurs and particle volume fraction increases. The simulations start with low initial volume fractions and are carried out until the particle volume fraction reaches approximately 0.6. In the present study, evaporation is assumed to occur at a constant rate. As water evaporation occurs, the air-water interface moves downward (in the negative z direction) and the simulation cell shrinks in the z direction. The rate of evaporation

(flux) is used to determine the velocity of the air-water interface. At any instant of time, the particle volume fraction ϕ in dimensionless units is given by:

$$\phi = \frac{N\frac{4}{3}\pi}{X_0 Y_0 (Z_0 - \tau)} \tag{4.1}$$

Where N is the number of particles considered, X_0 and Y_0 are the dimensionless sizes (i.e. in units of particle radius) of the computational cell considered in x and y directions, Z_0 is the dimensionless initial thickness of the cell in the z-direction, and τ is the dimensionless time. Because the scaled velocity is one, (Z_0- τ) represents the thickness of the computational cell. The denominator of equation (4.1) represents the volume of the computational cell. Figure 4.1 shows the change in the particle volume fraction as a function of dimensionless time. A dimensionless time of 50 indicates the time taken for the air-water interface to reach the substrate. The particle volume fraction initially rises slowly with time. As the volume of water decreases the particle volume fraction rises sharply, which is due to the hyperbolic nature of equation 4.1.

In all the simulations carried out in this thesis, the latex dispersion is assumed to be applied on an impermeable substrate. In these simulations, once a particle hits the substrate, the velocity of the particle is set to zero and the particle is allowed to slide freely in the x-y plane.

In this chapter, the evolution of the packing structure and particle layering is observed by taking snapshots of the particle distributions at various volume fractions. Throughout this thesis, the term *snapshot* refers to rendered image of 3D picture of the particle arrangement obtained using Visual Molecular Dynamics software (Humphrey et al., 1996).

To study the evolution of particle layers, snapshots were taken at specific volume fractions (corresponding to points A to G in Figure 4.1) which were chosen to show transition in the number of distinct layers where particles in two different layers merge to reduce the number of distinct layers.

4.3 Predictions for Base Case

This section presents the results obtained from analysis of a *base case*. The base case simulations are carried out with 300 particles. This corresponds to an initial volume fraction of 0.06. The simulations are carried out until the particle volume fraction reaches approximately 0.6 (i.e. at $\tau \cong 45$). The parameters used for the *base case* are listed in Table 4.1. The next sub-section discusses the evolution of particle layers with water evaporation.

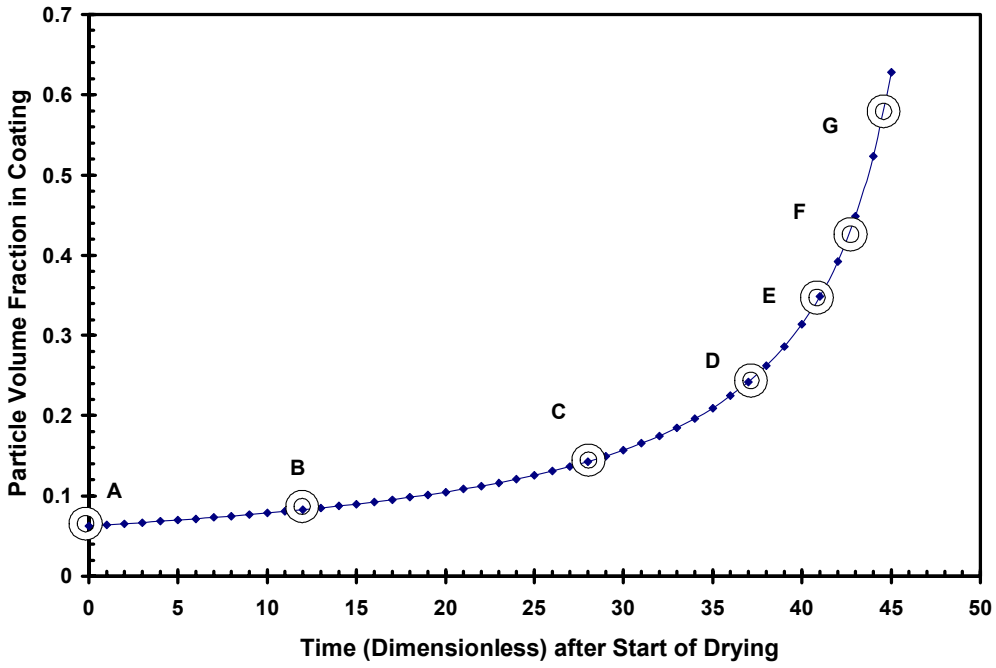

Figure 4.1 Particle volume fraction as a function of dimensionless time

Table 4.1 List of parameters used for the base case.

Variable	Symbol	Value	Units
Particle radius	**a**	**0.5**	**microns**
Air-water interface velocity	**V_S**	**10^{-5}**	**m/s**
Particle charge	**Q**	**$4.7*10^{-16}$**	**Coloumbs**
Inverse screening length	**k**	**10^{7}**	**/m**
Variance of random force	**$<R^2>$**	**$7.8*10^{-23}$**	**$(Newton)^2$**

4.3.1 Evolution of Particle Layers with Water Evaporation for Base Case

As water evaporation occurs and the particles move continuously under the influence of several forces, under suitable conditions, the system evolves slowly from an aqueous dispersion to a regularly ordered array. In the initial stages of drying, when the latex system is dilute, random Brownian forces dominate over columbic repulsions. This is because at relatively high inter-particle distances, columbic forces become negligible. As particle volume fraction increases and the inter-particle distances decrease, the magnitude of inter-particle columbic repulsions increases and largely influences the particle distribution and arrangement. This section of the chapter details the evolution of particle layers due to the effect of inter-particle repulsions.

The formation of layers of particles is demonstrated by 3D images of particle positions at various times during the course of water evaporation. For the base case, the approximate time of drying is 2.25 s or 45 in dimensionless units. This is the time taken for the computational cell to shrink to a size of approximately five particle radii

i.e. it is the time taken for the system to evolve from particle volume fraction of 0.06 to approximately 0.6. The 3D snapshots are taken at seven different instants of time to show the evolution and merging of layers. The volume fractions and time instants to which they correspond are indiacted as A to G in Figure 4.1. The first point 'A' corresponds to the distribution at $\tau = 2$ and points 'D' to 'G' correspond to instants where considerably distinct layers can be seen. Points 'B' and 'C' correspond to time instants where layers are only evident at the top and bottom surfaces of the coating.

Figure 4.2 shows snapshots of particle arrangements at the seven times which are points A to G in Figure 4.1. The side view of the particle positions at $\tau = 2$ are shown in Figure 4.2 (a). The initial particle positions are generated from a random number generator as discussed in Chapter 3, and there is no visible ordering or layering.

Figures 4.2 (b) and (c) show the side views of the particle distribution at times τ = 12 and 28, corresponding to particle volume fractions of 0.08 and 0.14 respectively. At these volume fractions, layers start to form close to the air-water interface and at the substrate, but most part of the computational cell still has randomly distributed particles.

Figures 4.2 (d) to (g) show the side views of the particle distributions at times τ = 37, 40.8, 42.5, and 44.4, corresponding to volume fractions of 0.24, 0.34, 0.42, and 0.56 respectively. At these volume fractions, distinct particle layers span through the thickness of the computational cell.

As water evaporation occurs and particle volume fraction increases, the latex system can be considered to go through a series of stages before a final packing

structure is formed. At short times after drying starts, layers of particles are formed at top and bottom surfaces. Surface tension forces are responsible for the formation of particle layer at the top surface. When air-water interface contacts a particle, surface tension dominates over all other forces and the motion of the particle is entirely under the influence of surface tension force. So the particles tend to move along with the interface resulting in higher particle density at the top. The layer of particles forms at the bottom of the computational cell due to the presence of the impermeable substrate. In this model when particles hit the substrate, they no longer move in the z-direction, resulting in the formation of a layer.

Intermediate layers form due to repulsions from particles in top and bottom layers and also due to repulsions among the particles in the intermediate region. As computational cell shrinks with evaporation, the distance between layers decreases. This continues until the repulsions between layers (inter-layer repulsions) become much greater than repulsions between particles in a layer (intra-layer repulsions). This domination of inter-layer repulsions results in an unstable configuration. A small vertical perturbation in particle position will cause it move to next layer by forcing a hole open in next layer. This finally results in merging of layers. This can be seen from Figures 4.2 (d) to (g), where six layers of particles have merged to form a final three layered structure.

During a drying simulation, the number of layers decreases with time and the number of particles per layer increases. However, the simulations show that the number of particles in each layer is almost equal. This is shown in Figure 4.3 which is the plot of number of particles in each layer corresponding to Figures 4.2 d), e), f),

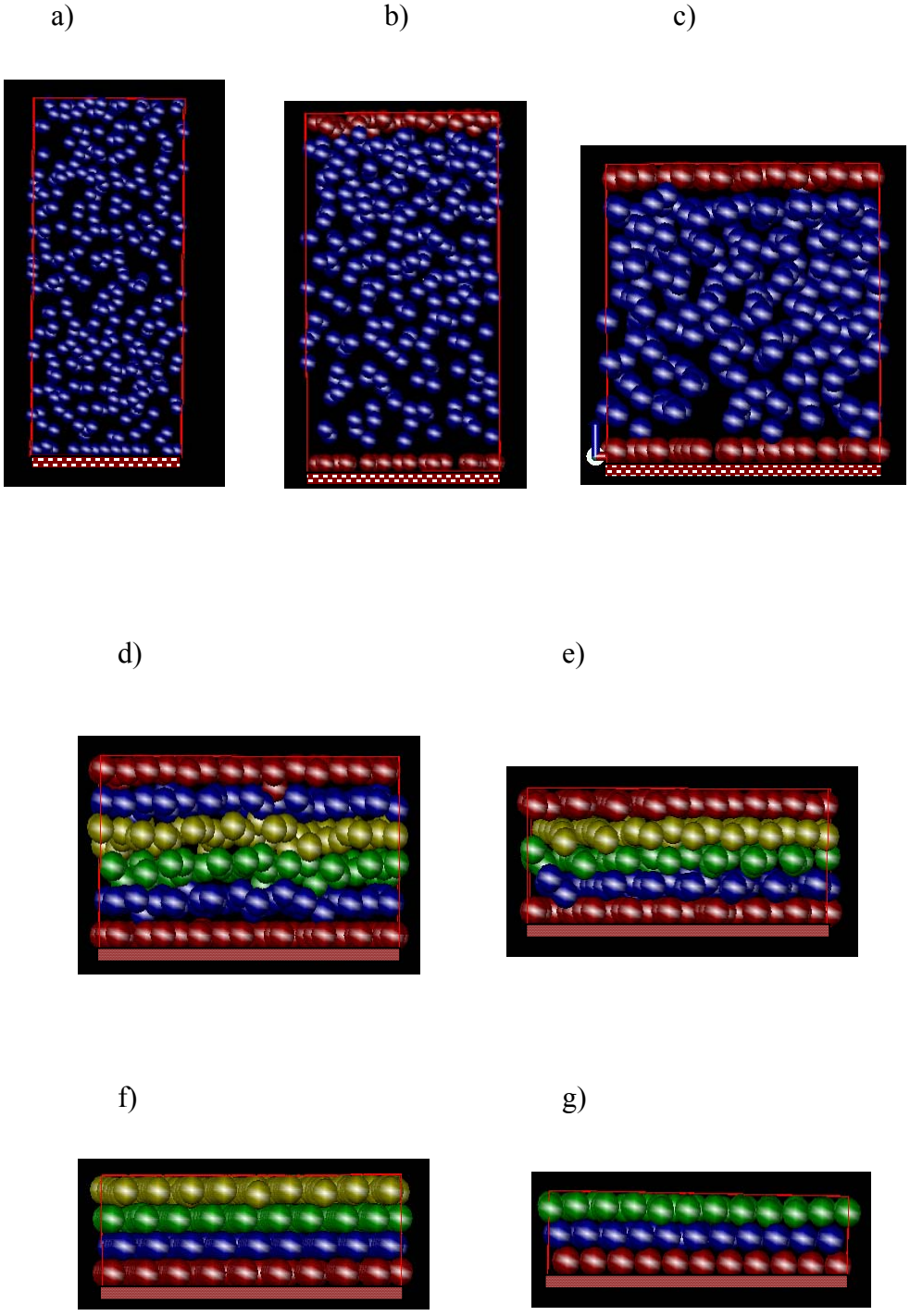

Figure 4.2 Rendered images of side views of predicted particle arrangements at various times during evaporation: a) $\tau = 2$; b) $\tau = 12$; c) $\tau = 28$; d) $\tau = 37$; e) $\tau = 40.8$; f) $\tau = 42.5$; g) $\tau = 44.4$. Particles are colored only to aid the reader in identifying layers.

and g). This is expected because, in the present simulations, all particles were assumed to be equally charged. If the particles were unequally charged, the layers might have had unequal number of particles.

Figure 4.4 shows the evolution of distinct layers as a function of time. For most of the drying period no internal layering was observed and distinct layers are

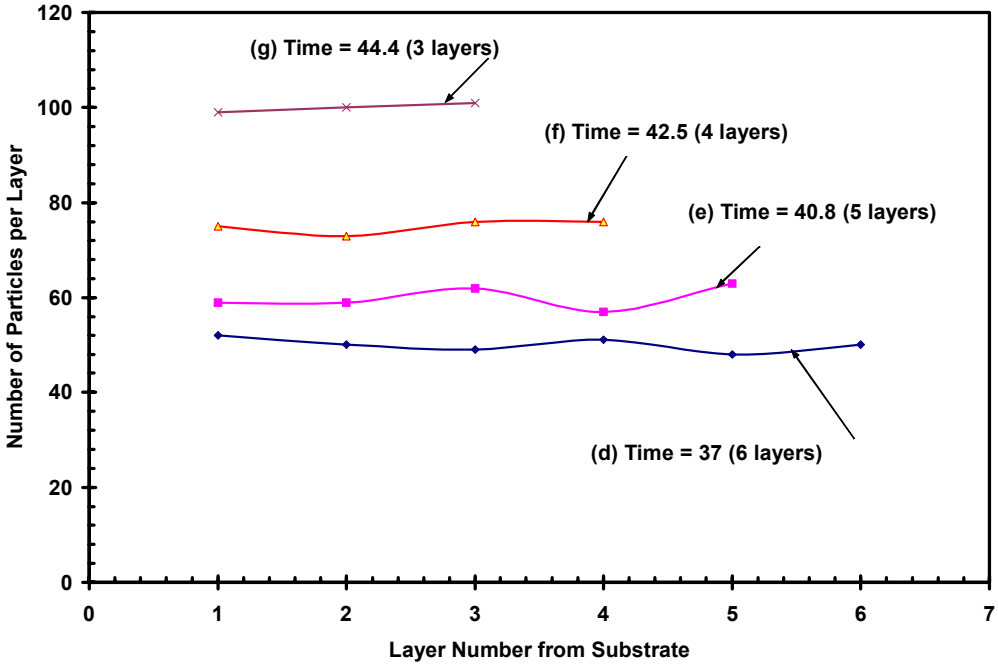

Figure 4.3 Plot showing the number of particles per layer corresponding to Figures 4.2 (d) to (g).

visible only at times beyond τ = 37 (greater than 80% of the drying time). Though layers are formed at the top and bottom surfaces at times below τ = 37, they are not shown in the plot. Only the times at which the layers of particles span through out the thickness of the cell are used for the plot. Furthermore, once layers form, they collapse quickly; the transition from six layers to three layers takes approximately 16% of the drying time. This is because of the strongly influencing inter-particle repulsions during the later stages of drying.

The formation of layers can be quantified by plots of the areal particle density through the thickness of the film. At any point of time during drying, the computational cell can be divided into infinitesimally thin imaginary planes parallel to the x-y plane (substrate). For a plane at a given distance from the substrate, the areal particle density is the fraction of the plane that intersects particles:

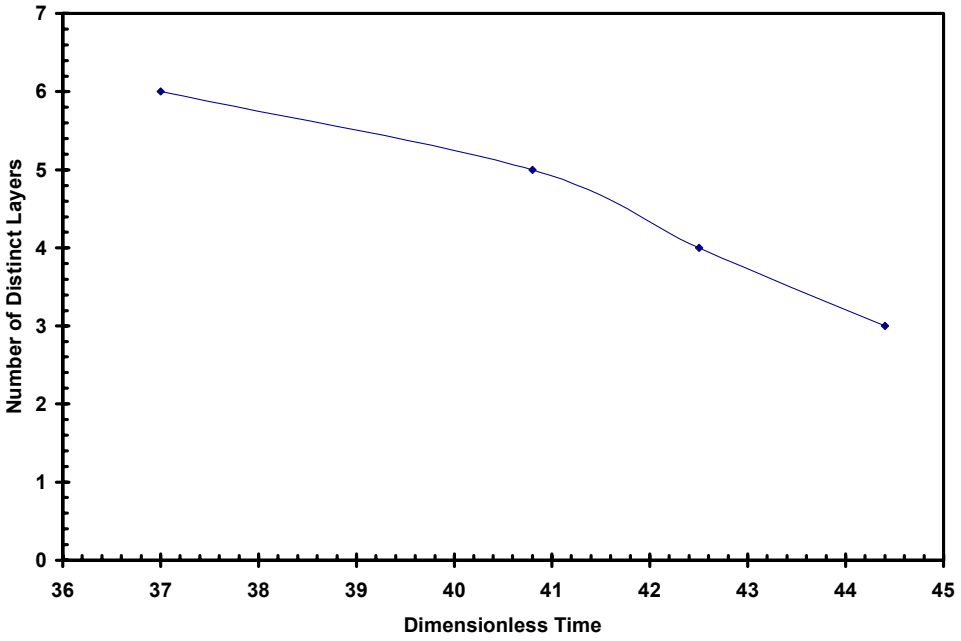

Figure 4.4 Plot showing the number of distinct layers as a function of dimensionless time.

$$A_D = \frac{\sum_{i=1}^{N_p} \pi r_i^{\,2}}{X_0 Y_0} \tag{4.2}$$

A_D is the areal particle density, r_i is the radius of the circle of intersection of the spherical particle i and the plane, N_p is the number of particles that intersect the plane and X_0Y_0 represents the area of the plane. The parameter r_i depends on the extent to which a particle penetrates into the imaginary plane.

Finding the areal particle density at a given distance (Z) from the substrate is a good way of following the evolution of particle layering. Along a plane at a given Z, if there is a higher concentration of particles, then equation (4.2) results in a higher value for the areal density function and vice versa. So, if a plot of areal density distribution vs. distance from substrate shows alternating high and low peaks, it is an indication that there are alternating regions of high and low particle concentrations which is an indication of particle layering.

Figure 4.5 (a) is the areal particle density plot corresponding to times τ = 0, 7, 12, and 28. Figure 4.5 (b) is the plot corresponding to times τ = 37, 40.8, 42.5, and 44.5. The areal density distributions are plotted on two different plots to show the two different drying phases. The first plot (a) corresponds to the drying phase during which no internal layers exist. The second plot (b) corresponds to the phase during which distinct layers span throughout the thickness of the cell.

In Figure 4.5 (b), as was discussed earlier, the peaks correspond to the number of layers that are formed. At time τ = 37, the areal particle density curve shows six peaks indicating the presence of six layers; at τ = 40.8, the curve shows five peaks indicating the presence of five layers, and so on. As all particles belonging to the same layer do not have exactly the same z-coordinates, the points at which peaks occur can be considered to be the average location of the particle layers. From this data we can calculate the distance between the particle layers. For a given number of layers (i.e. at a given time and volume fraction), the distance between each of the layers is approximately the same (as shown in Figure 4.5 (b)). For example, the inter-layer distance for the case of six layers is approximately 2.2 (in dimensionless units)

and the inter-layer distance for the case of 3 layers is approximately 1.8. This observation of equal inter-layer distance is in a way same as the observation of equal number of particles per layer shown in Figure 4.3. These observations are a result of equal charge present on all the particles in the system, resulting in the tendency to form uniformly distributed, equally spaced particle layers.

The greater the differences between the high and low peaks, the more distinct are the layers. For the case of six layers, the differences between peaks are relatively less, showing that the particle layers are not as distinct as in the case of four and three layers. This is also evident from the snapshots of the side views shown in Figures 4.2 d) to g). In the early phases of drying, the inter-particle interactions are not strong enough to facilitate particle layering (as shown in Figure 4.5 (a)). This time period corresponds to approximately 60% of the drying time.

As time increases, the areal densities close to the air-water interface (away from substrate) are relatively higher compared to those close to the substrate. This shows that in this phase of drying the particles tend to accumulate more close to the air-water interface than at other locations. This can be attributed to the high Peclet number. Peclet number (Pe) is the ratio of evaporative convection and Brownian diffusion:

$$Pe = \frac{ZV_S}{D} \tag{4.3}$$

Z is the thickness of the cell, V_S is air-water interface velocity, and D is the Brownian diffusivity defined in Chapter 2. For the base case, at the starting of drying, Peclet number has a value of 489. A Peclet number much greater than one shows that the air-water interface moves much faster than the particles could diffuse due to random

a)

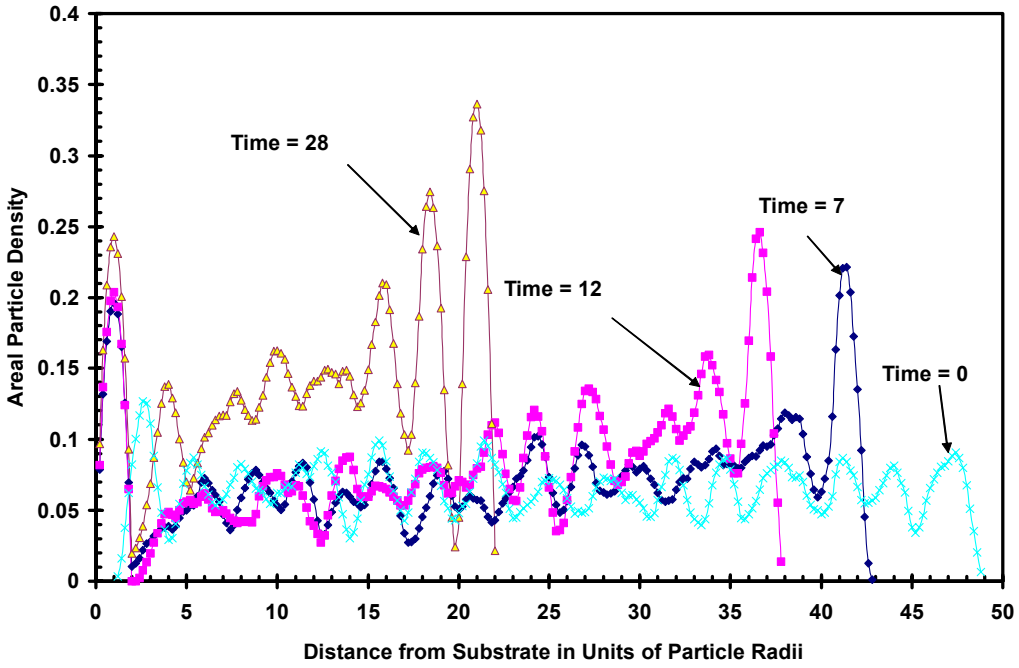

b)

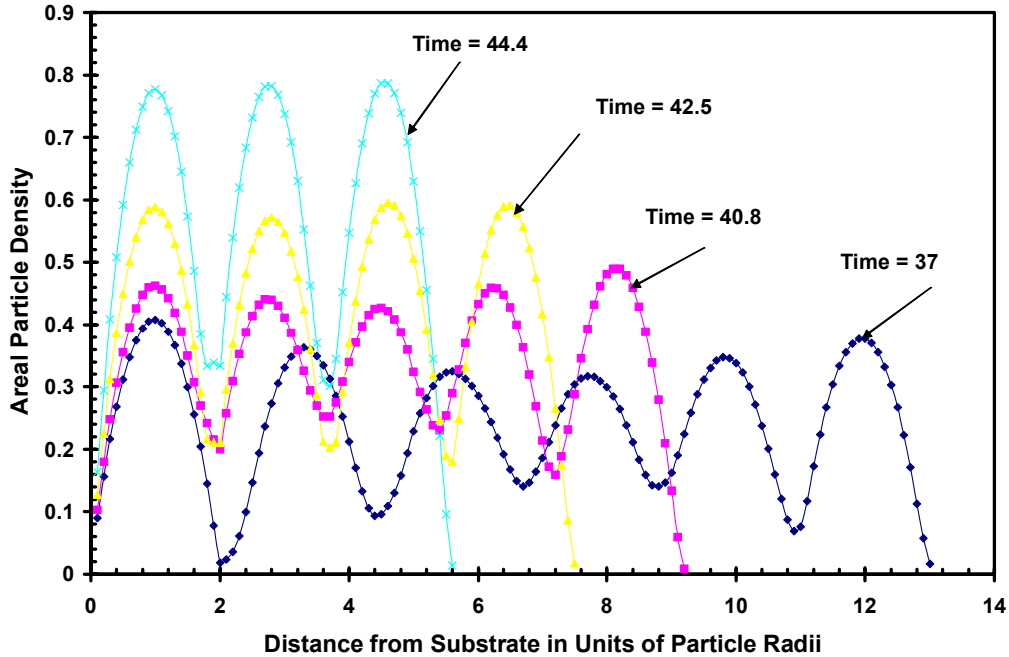

Figure 4.5 Plots of areal particle density as function of distance from substrate for: a) Initial phase and b) Later phase of drying. (Times indicated on the curves are dimensionless times τ .)

force. This results in accumulation of particles close to the top surface. The mechanism for higher particle densities close to air-water interface is corroborated using a particle equilibration simulation in the absence of drying. Those results will be presented in Section 4.3.3.

As the substrate is impermeable and all the particles which hit the x-y plane can not move anymore in the z-direction, there is accumulation of particles at the substrate. Also, particles close to the substrate may sometimes hit the substrate due to the random nature of the Brownian force acting on them. This causes a depletion zone close to the substrate (Figure 4.5 (a)).

In summary, the analysis using 3D snapshots of side views and areal density distributions shows that for most of the drying process (i.e. for 80% of the drying time), no internal layering is predicted. When layers start to form, is the balance of several factors: magnitude of columbic repulsions, drying rate, particle size, etc. Evaporative time scale being much larger than the diffusive time scale is responsible for high particle densities close to air-water interface during the initial phase of drying. The next section discusses the evolution of ordered packing structure with evaporation for the base case.

4.3.2 Evolution of Packing Structure with Water Evaporation for Base Case

As water evaporates, apart from the evolution of particle layers, under ideal conditions, the system evolves from a disordered state to an ordered packing structure. Past experimental analysis indicated the evolution of face-centered and hexagonal cubic packing structures at the end of water evaporation stage (Jaonicot et. al., 1990). Ideally a complete closed packed structure is obtained at a particle volume fraction of

0.74. All the models that are used to predict particle deformation during stage II assume the existence of a close packed structure at the starting of the stage. So, following the evolution of packing structure using the particle dynamics model would be useful in corroborating the experimental evidence and identifying the conditions under which the assumptions made during Stage II of latex film formation are true.

Because of the high computational effort needed to achieve a volume fraction of 0.74, the simulations were carried until the volume fraction reaches 0.6. As multiple layers form, the particles within the layers tend to arrange before merging occurs. During the merging process, the arrangement of the particles is lost. The snapshots of the top views of the particle distributions are taken at four different instants of time (four different volume fractions).

The first snapshot (Figure 4.6 (a)) is taken at a volume fraction of 0.06, which is the which corresponds to $\tau = 2$. The second (Figure 4.6 (b)) corresponds to the volume fraction (0.42) at which four particle layers exist. The third and fourth snapshots correspond to the volume fractions (0.56 and 0.59) at which 3 layers exist (Figures 4.6 (c) and (d)).

The top view of the distribution at $\tau = 2$ shows that there is no ordered structure at the start of the simulation. Before analyzing the packing structure for the other three volume fractions, the particle layer stacking for the case of an ideal FCC and HCP structures will be discussed.

An ideal FCC or HCP close packed structure can be viewed as a stacking of hexagonal particle layers one over the other. Figure 4.7 shows the stacking of layers for the case of both FCC and HCP structure. As is evident, the 1^{st} and 2^{nd} layer of

particles are the same for both FCC and HCP structures. The interstitial spaces between the particles in the 1st layer are of two types. The spaces at which 2nd layer of particles are centered are called Left Interstitial Spaces (LIS) and the spaces at which 3rd layer of particles are centered are called Right Interstitial Spaces (RIS) (shown in Figure 4.7 (a) for FCC).

In FCC stacking, if the particles in the 2nd layer are at the LIS, then the 3rd layer particles are at the RIS and vice versa. In HCP stacking, the 2nd layer of particles can be at either LIS or RIS, but the 3rd layer of particles are exactly above the 1st layer of particles. In an FCC structure, the hexagonal close packed layers form the (1, 1, 1) lattice planes of the cubic packing structure. In a HCP structure, these hexagonal layers form (0, 0, 1) basal planes of the hexagonal packing structure. Based on this understanding of the FCC and HCP structures, the packing structures shown in Figure 4.6 will be analyzed.

In the snapshots shown in Figure 4.6, the particles are given different colors to aid us in distinguishing the different layers to which they belong. In Figure 4.6 (b) the bottommost layer (1st layer) is colored red, 2nd layer is colored blue, 3rd green, and 4th (topmost layer) yellow. The stacking of layers corresponds to a HCP packing. The particles in the 4th and 2nd layers are centered exactly one over the other and the particles in the 3rd layer are centered at the RIS of the 4th layer. The particles in the 1st layer have the same lattice points as of particles in the 4th layer, indicating the repeating of layers. The small deviations of the particle positions from their ideal lattice positions can be attributed to the fact that these particles are in continuous motion and these are the snapshots taken at an instant of time.

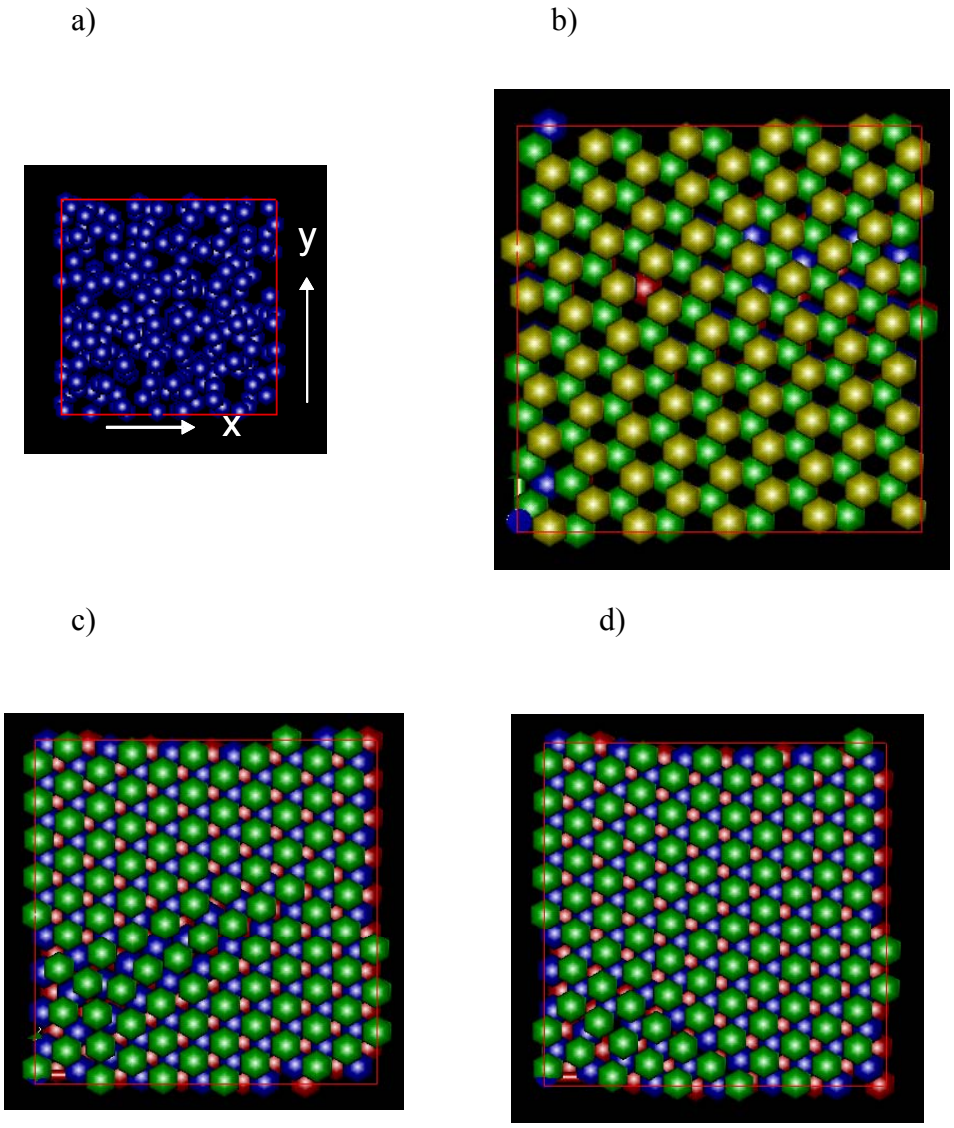

Figure 4.6 Top views of packing structure evolution at four different times: a) $\tau = 2$ ($\phi = 0.06$); b) $\tau = 42.5$ ($\phi = 0.42$); c) $\tau = 44.4$ ($\phi = 0.56$); d) $\tau = 44.7$ ($\phi = 0.59$). ϕ is the particle volume fraction. Particles are colored only to aid the reader in identifying layers.

Figure 4.6 (c) is the snapshot of the top view when the number of layers has reduced to 3 and the volume fraction has increased to 0.56. The packing structure has changed from HCP to FCC. The particles in the 2nd layer (colored blue) are located at the RIS of the particles in the 1st layer (colored red) and the particles in the 3rd layer (colored green) are located at the LIS of the 1st layer particles. This is an indication of an FCC structure. Comparison of b) and c) shows that the orientation of layers has remained almost the same and the particles have just moved to new lattice locations to form an FCC structure. As the volume fraction is increased to 0.59 (Figure 4.6 (d)), the packing structure has evolved into a more ordered FCC structure without the small disorders that are visible at volume fraction of 0.56.

Thus, as particle volume fraction increases due to water evaporation, FCC and HCP are the two most stable packing structures to which the latex system evolves. As particles in different layers merge under the influence of increasing inter-particle repulsions, the particles move from HCP lattice points to FCC lattice points. This depends on which of the two structures have lowest free energy at that instant of time. As free energy calculations for the packing structures cannot be made from the present simulations, the exact influence of free energies on type of packing obtained cannot be determined. It can only be concluded that FCC and HCP are the only two stable structures that can be seen during Stage I of latex film formation.

As the hexagonal close packed particle layers in c) and d) of Figure 4.6 are the (1, 1, 1) planes of FCC structure, the distance between the particle layers can be used to determine the size of the unit FCC cell. In an FCC crystalline structure, the distance between (1, 1, 1) planes, $d_{(1,1,1)}$, is related to the unit cell size by:

a)

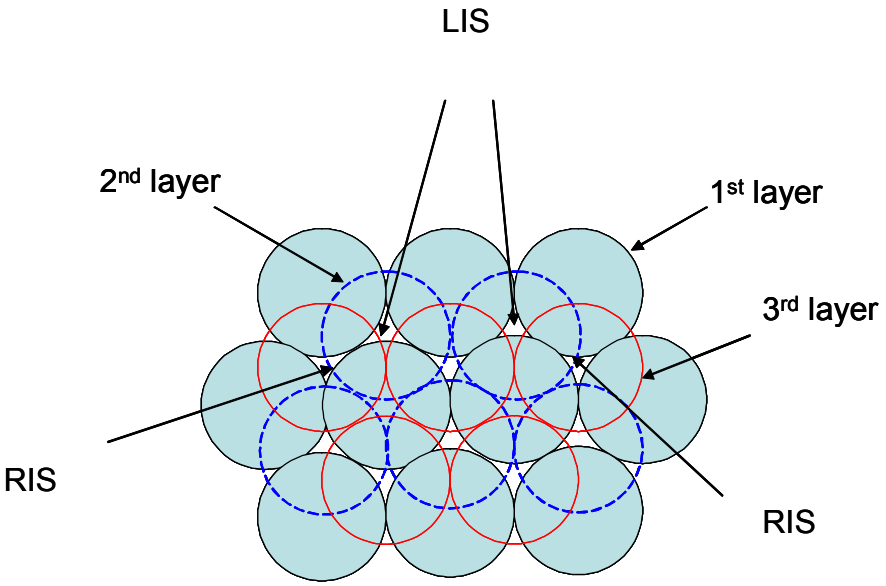

b)

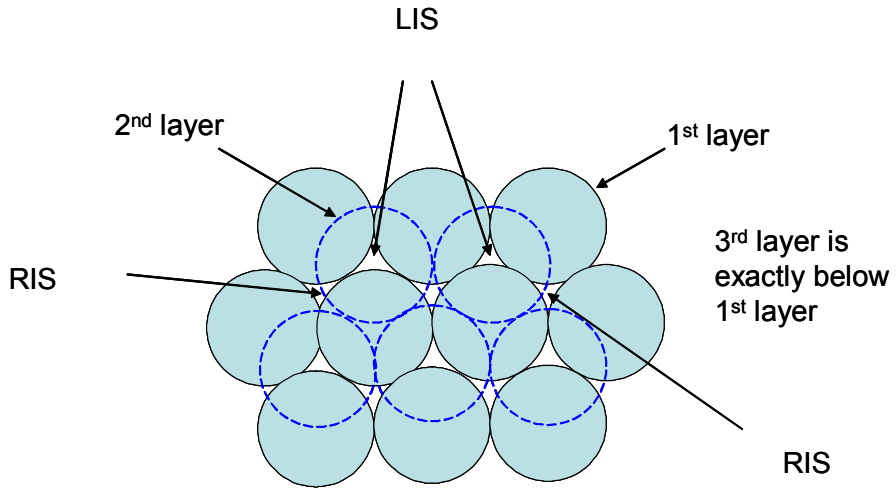

Figure 4.7 Hexagonal Layer Stacking for the case of a) FCC and b) HCP structures. Shaded circles represent 1st layer; Unshaded and dotted circles represent 2nd layer; Unshaded and continuous circles represent 3rd layer.

$$d_{(1,1,1)} = \frac{a_0}{\sqrt{3}} \tag{4.4}$$

Where a_0 is the size of the unit cell. At volume fraction of 0.56, the distance between the planes was found to be 1.78 in dimensionless units. This gives a cell size of 3.08 from equation 4.4. In an ideal FCC packing, when the particles on the face diagonal exactly touch, the unit cell size is 2.828 in dimensionless units (scaled with particle radius).

As the volume fraction is increased to 0.59, a cell size of 2.788 is obtained. This indicates that the particles are close packed and in fact, they have penetrated slightly into each other. This behavior is observed because in this study, no account is taken of the sticking or deformation phenomena occurring when particles touch each other i.e. the particle contact boundary conditions were not included in the model. As the goal is to make a qualitative analysis of the packing structure and layering phenomena, this is a reasonable assumption.

From the analysis made on evolution of packing structure with water evaporation, it can be concluded that HCP and FCC are the stable structures obtained. This is in agreement with the experimental predictions made by He et al. (1996) and Monovoukas et al. (1988). It was also evident that distance between layers can be used to determine the FCC cell size. As volume fraction increases, the cell size shrinks and the inter-layer distances decrease, resulting in less and less compatibility with the FCC closed packed structure. The anomalous observation of particle penetration is due to the neglecting of particle contact boundary conditions in the model. The next section presents the results of the particle equilibration simultion run in the absence of drying.

4.3.3 Particle Equilibration Simulations in the Absence of Drying

For carryingout particle equilibration simulations in the absence of drying, the air-water interface velocity (water evaporation) is set to zero, and the particles are allowed to move under the influence of all other forces. The parameters used are same as those used for the base case.

Figure 4.8 shows the areal density plots from the thermal equilibration simulation at several times, with $\tau = 50$, corresponding to the time it would take for the interface to reach the substrate in the drying simulation. Comparison of the three curves shows that even after sufficiently long times, the areal density distribution has remained qualitatively the same as that of the initial areal density distribution. Unlike in the case of water evaporation, here the particles have not shown special preference to settle close to air-water interface. This is because the Peclet is number not greater than one in this case.

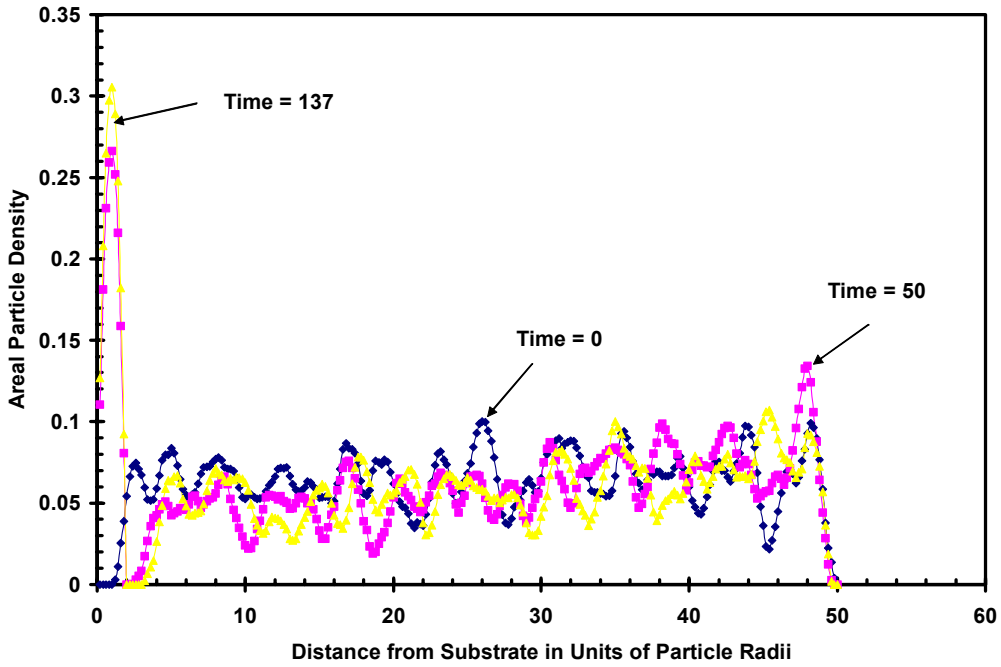

Figure 4.8 Areal density plots for Particle equilibration run in the absence of drying.

4.4 Influence of Initial Particle Distribution on Particle Packing and Layering

Once a detailed analysis on the base case was made, the influence of various physical parameters involved in the drying process on the packing structure obtained at the end of water evaporation and on the evolution of particle layers with evaporation is investigated. In this section, the influence of the initial particle distribution used for the simulation on evolution of particle layers and packing was analyzed. The initial particle distribution in real systems is predominantly random and does not come in the modeling analysis as any particular physical parameter, so, it should not have any influence on the final structure. This section demonstrates that the analysis would serve as a method of verifying the accuracy of the numerical technique.

Figure 4.9 shows the comparison of areal density plots obtained at three different instants of time for two different initial particle distributions. Figure 4.9 (a) shows the formation of five particle layers at time τ = 40.8 for the two cases. Comparison is not made at times below 40.8 because the inter-particle forces are not strong enough to influence particle distribution and it is more dependent on the initial particle distribution used.

The results in Figure 4.9 show that the number of layers formed is independent of the initial distribution. Also, the density peaks for both cases occur at same distances from substrate, indicating that the inter-layer distances are the same. This is expected because number of layers formed and the inter-layer distance is dependent on the total effective inter-particle interactions; and after considerably long drying times (beyond τ = 40 in this case), these interactions would be dependent

a)

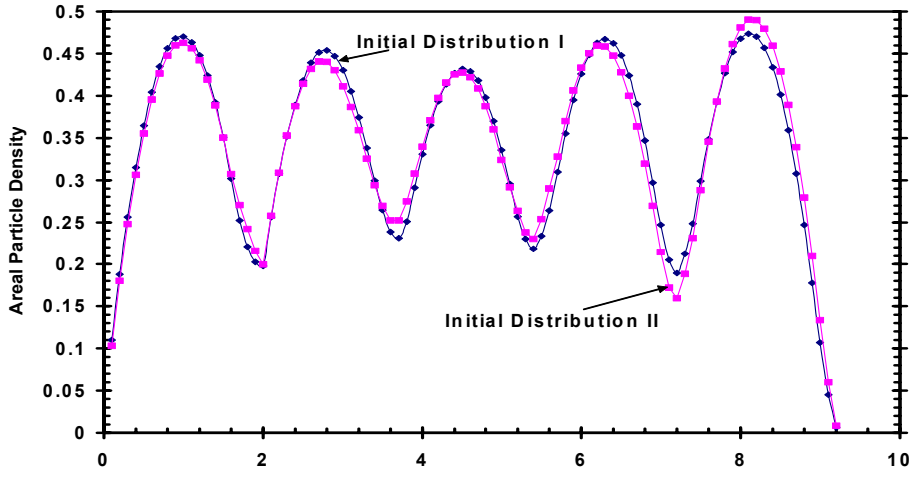

b)

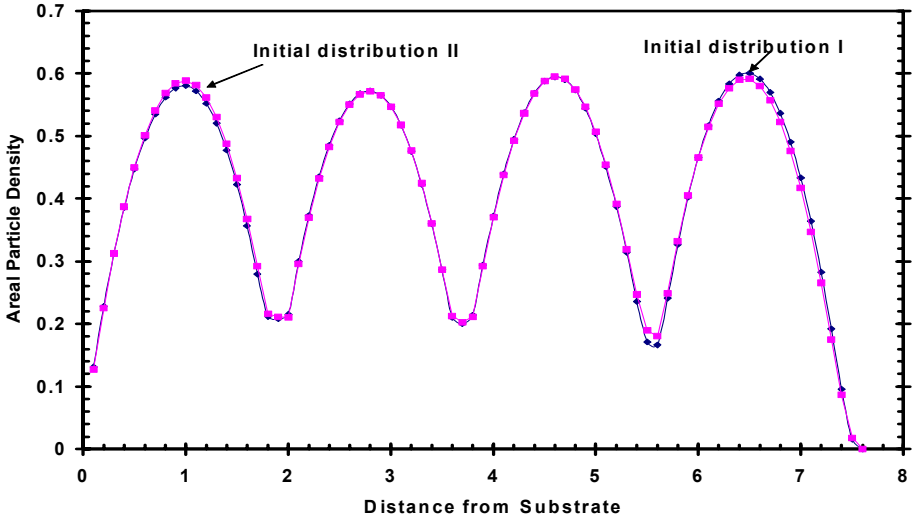

c)

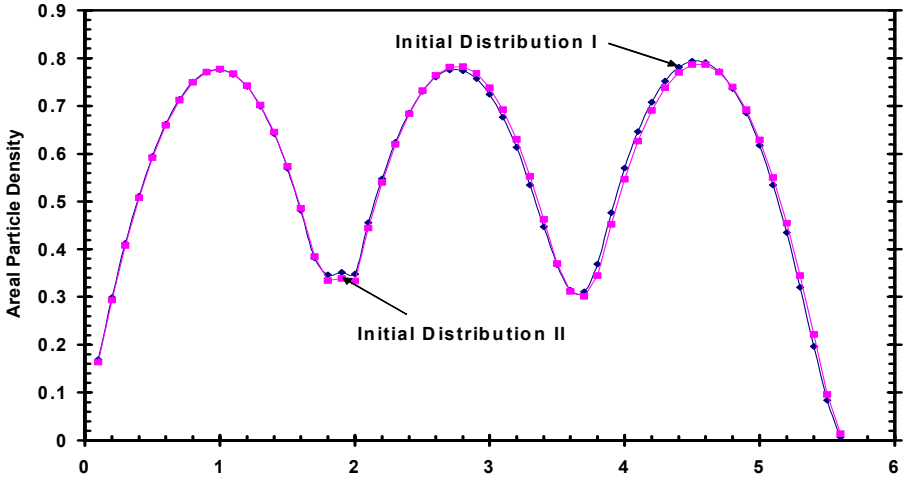

Figure 4.9 Areal density vs. dimensionless distance from substrate plots for two different initial particle distributions at times: a) $\tau = 40.8$; b) $\tau = 42.5$; c) $\tau = 44.4$.

only on the total particle charge and the total number of particles and would be independent of the initial relative particle orientation (distribution).

Small deviations between the two curves in Figure 4.9 (a) may be due to the fact that the inter-particle repulsions are still not too strong to completely negate the influence of initial distribution. At higher times (τ = 42.5 and 44.4), when the interactions become stronger, the two curves are more identical, as is evident from Figures 4.9 (b) and (c).

Figure 4.10 compares the packing structures obtained using the two initial distributions at times τ = 42.5 and 44.7 ((a) and (b) respectively). The snapshots at both times agree well for the two cases. For the time instant at which the packing structure is FCC, the size of the unit cell is estimated from the average inter-layer distance using Equation (4.3). For the two distributions, the cell sizes obtained were 2.788 and 2.792 in dimensionless units. This corresponds to an error of less than 0.15% which is clearly acceptable given the assumptions made.

Thus from the areal density plots and snapshots of the top views of the particle packing obtained using two different initial distributions, it can be concluded that beyond τ = 40, the inter-particle interactions would be strong enough to negate the effect of initial particle distribution and the evolution of particle layers and packing structure is the same irrespective of the initial distribution. This analysis also serves as a method of verifying the consistency and accuracy of the numerical technique. The next section discusses how initial particle volume fraction influences the evolution of particle layers and packing structure.

a)

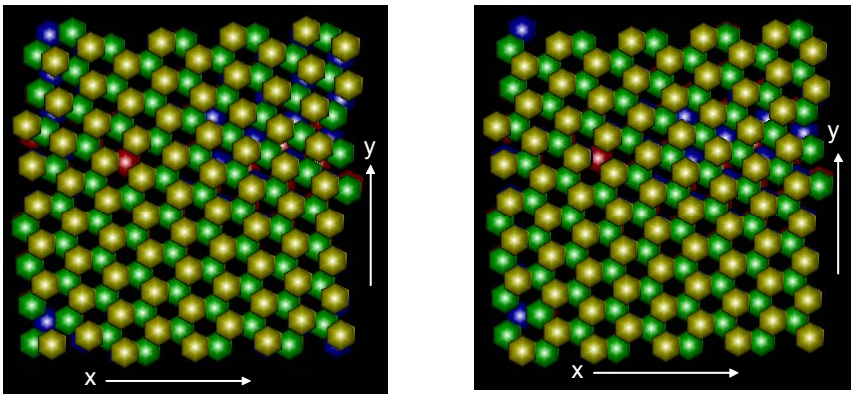

b)

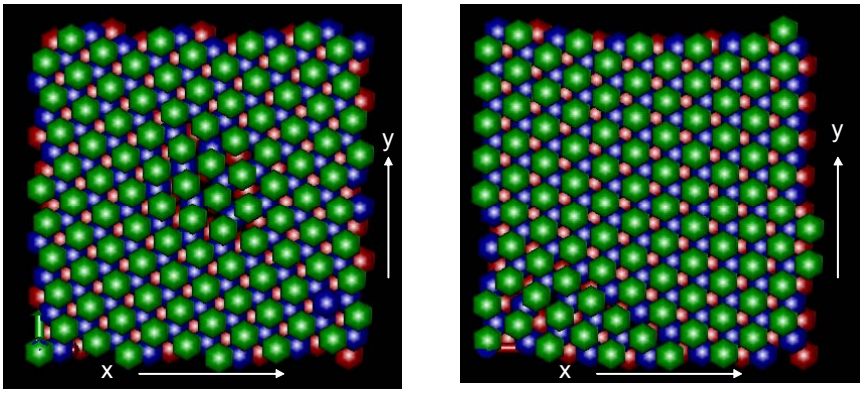

Figure 4.10 Top views of particle packing for two different initial distributions at: a) $\tau = 42.5$ and b) $\tau = 44.4$. Particles are colored only to aid the reader in identifying layers.

4.5 Influence of Initial Particle Volume Fraction on Particle Packing and Layering

Initial particle volume fraction with which drying of a latex coating is started is a significant parameter that influences the drying phenomena. In the present modeling study, the initial volume fraction depends on the computational cell size chosen and the number of particles used. Here in order to start with higher volume fraction compared to base case, the computational cell size was kept constant and the

number of particles was increased from 300 to 400. This corresponds to a change in volume fraction from 0.06 to 0.08. Higher initial volume fractions were not used due to high computational costs with additional number of particles.

Plots of areal particle density showed that using higher number of particles has no significant influence on the evolution of layers during Stage I. Figures 4.11 (a) and (b) show the areal density plots made at times τ = 12 (initial phase) and 40.8 (later phase) for the case of 300 and 400 particles. It can be seen that the only difference between the 300 particles and 400 particles case is that throughout the thickness of the computational cell, the areal density for the case of 400 particles is higher than that of 300 particles by approximately 33%. For example, in Figure 4.11 (a) the peak at air-water interface has a value of 0.25 for 300 particles and a value of 0.31 for 400 particles. This is a difference of approximately 33%. Same is true for the peak at the substrate. Similar trend can be observed from Figure 4.11 (b). Thus using higher number of particles for simulation does not result in more distinct layers. It only helps in achieving higher volume fractions maintaining the same number of layers at a given time.

a)

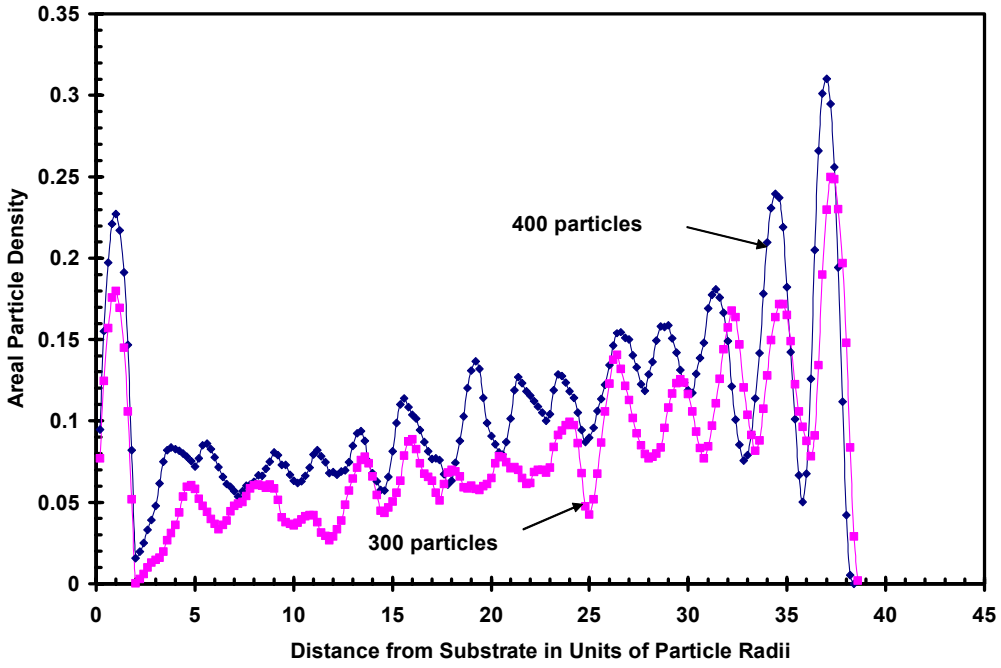

b)

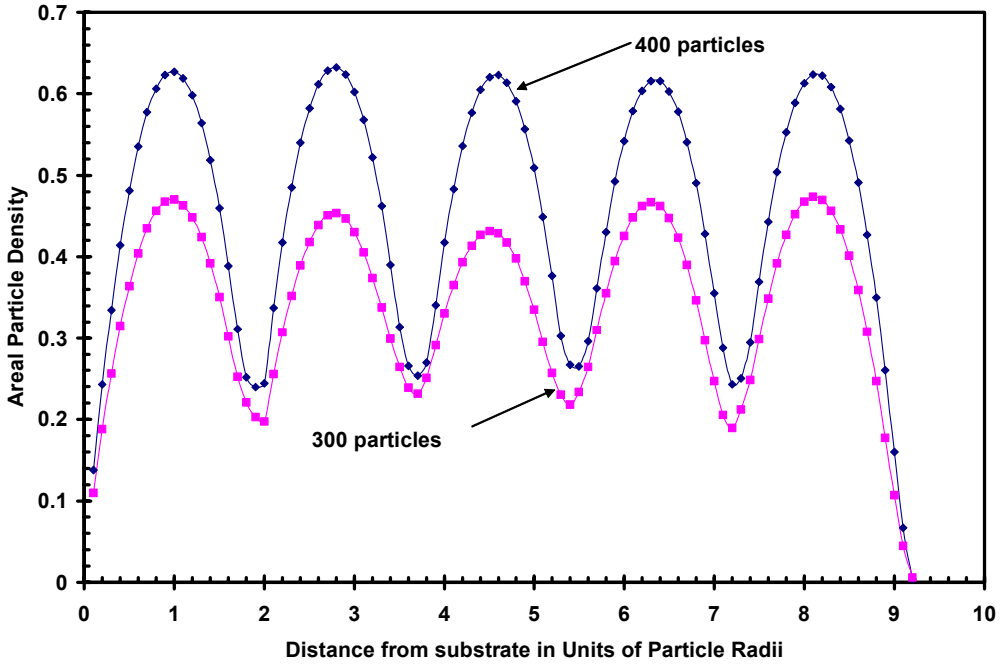

Figure 4.11 Areal density plots comparison for the case of 300 and 400 particles at times a) $\tau = 12$; b) $\tau = 40.8$.

4.6 Influence of Random Force on Particle Packing and Layering

During the initial phase of Stage I, when the inter-particle columbic repulsions are relatively weak, the Brownian motion of the particles becomes relatively significant. So a change in the magnitude of the random force used for simulating Brownian motion would result in a change in the behavior of the latex system during drying. In the present analysis, the magnitude of the random force is changed by changing the magnitude of the variance of the random force vector (given by equation 2.6). Two different magnitudes of the variance were used for comparison with the base case ($<R^2> = 7.8*10^{-23}$ $(Newton)^2$). One corresponds to a variance which is ten times the base case variance (i.e. $<R^2> = 7.8*10^{-22}$ $(Newton)^2$). The other corresponds to a variance which is one-fifth of the base case variance (i.e. $<R^2> = 1.56*10^{-23}$ $(Newton)^2$).

4.6.1 Influence of Random Force on Particle layering

Figure 4.12 compares the areal particle density plots for the three cases at times τ = 7 and 12. These times correspond to the initial phase of Stage I where Brownian motion is significant. From the plots, two important observations can be made.

First, particle density in the top most layer (near the air-water interface) of the computational cell decreases with increase in the magnitude of the random force. This is seen from the decrease in the areal density peak seen at air-water interface (changes from 0.22 to 0.17). This corresponds to a decrease in Peclet number from 489 to 155 as the magnitude of random force variance increases from $7.8*10^{-23}$ to $7.8*10^{-22}$ $(Newton)^2$. As was discussed in Section 4.3.1, the top layer is formed because the

evaporation rate is much higher than the Brownian diffusion rate. As the magnitude of random force is increased, the diffusion rate increases. This increase in the diffusion rate can help maintain a more uniform particle distribution at the top of the cell and there by result in a relatively lower peak of areal density at the top.

Second, the opposite trend is observed for the bottom layer i.e. the particle density in the bottommost layer near the substrate increases with increase in the magnitude of random force. This trend corresponds to a decrease in Peclet number. As was discussed in Section 4.3.1, the bottommost layer of particles is formed due to the impermeable substrate boundary condition used. During any time step, due to the random nature of the Brownian motion, half of all the particles which are with in a distance of 1.5 units of particle radii from substrate have a chance to hit the substrate and stick to it. With a higher magnitude of the random force, the likelihood of particles hitting the substrate would be even higher because of the greater net force acting on the particles. This results in greater particle densities at the substrate compared to the case of lower random force.

Figure 4.13 compares the areal density plots at times τ = 40.8 (five layers) and τ = 42.5 (four layers). These times correspond to the later phase of Stage I where Brownian motion becomes less significant and inter-particle columbic repulsions dominate. During this phase of drying, particle layers keep forming and merging under the influence of transverse (z direction) and lateral (x and y directions) inter-particle columbic repulsions. During this phase, the number of layers formed, distance between particle layers, and number of particles per layer depend on two factors: net overall repulsions forces and number of particles used for the simulation.

a)

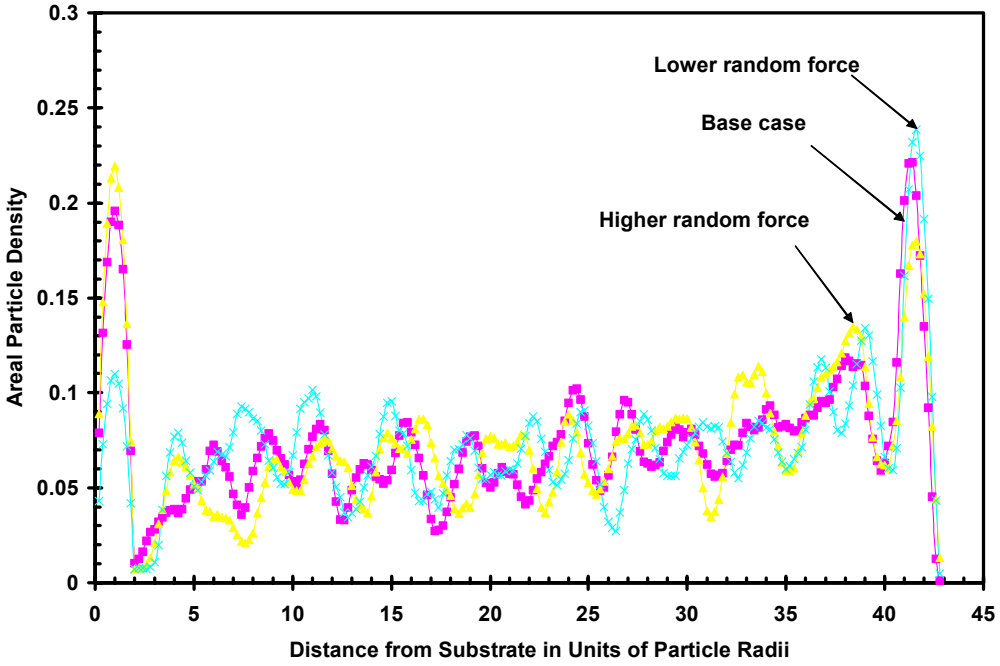

b)

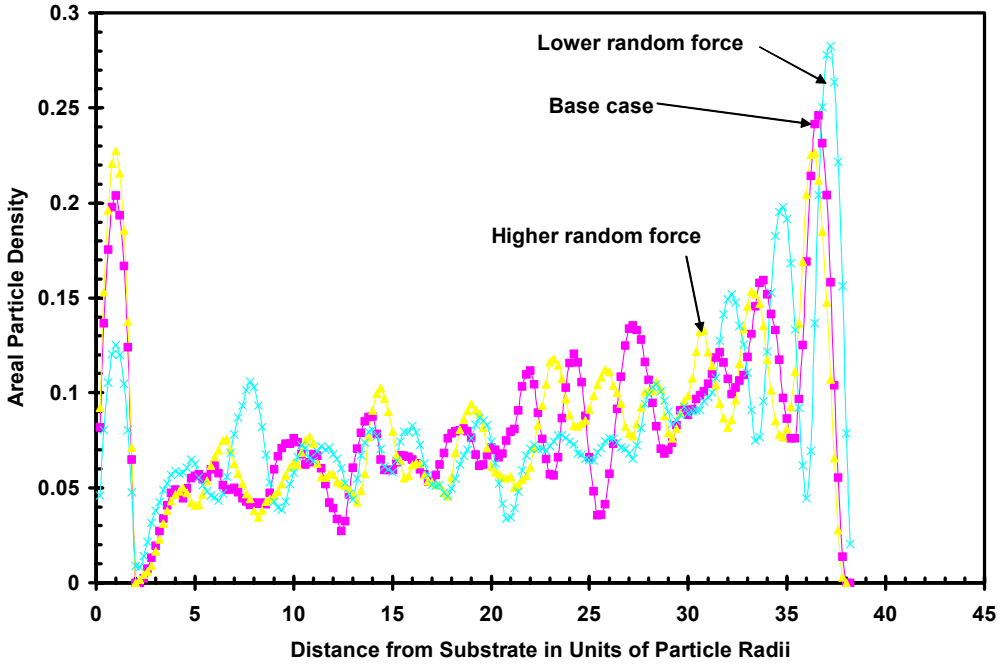

Figure 4.12 Areal density plots for three different magnitudes of random force variance at times a) $\tau = 7$; b) $\tau = 12$.

In the present analysis as both of these are kept constant, at a given time, the number of layers formed is same for all the three cases. The areal density peaks also occur at approximately same distances from substrate for all the three cases of random force magnitude. In an ideal case, the magnitude of peaks should be the same for all three cases. Figures 4.13 (a) and (b) show that this is true for peaks corresponding to top most and bottom most layers but not for intermediate layers. This is because, though inter-particle repulsions cause the layers to have same areal densities for all the three cases, random force acting on particles may cause slight displacement of particles in the intermediate layers resulting in different areal density profiles. This does not happen for top layer because there the particles are strongly held by surface tension forces and all particles which hit the interface stick to it. The same argument holds for the bottom layer where the particles stick to the impermeable substrate.

4.6.2 Influence of Random Force on Particle Packing

Figure 4.7 in section 4.3.2 shows that for the base case considered, the system evolves into HCP and FCC packings. Also, a truly ordered packing was obtained only when four or less number of particle layers are formed which corresponds to times beyond τ = 42.5. This sub-section analyzes how this behavior changes when the magnitude of the random force is changed.

Figures 4.14 (a) to (e) show the top views of the packings obtained at five different instants of time for the case of higher random force. Unlike the base case, with high random force, a highly ordered packing is predicted even when five layers of particles still exist. This is obtained at time τ = 40.8 which is less than the onset time for the base case (τ = 42.5). This is because, when a higher random force is

a)

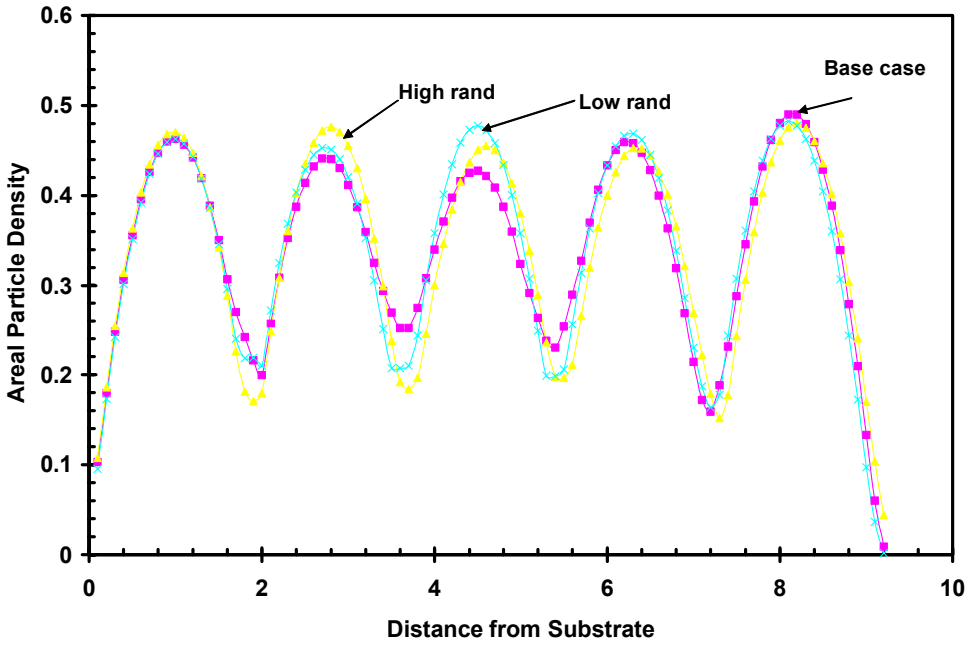

b)

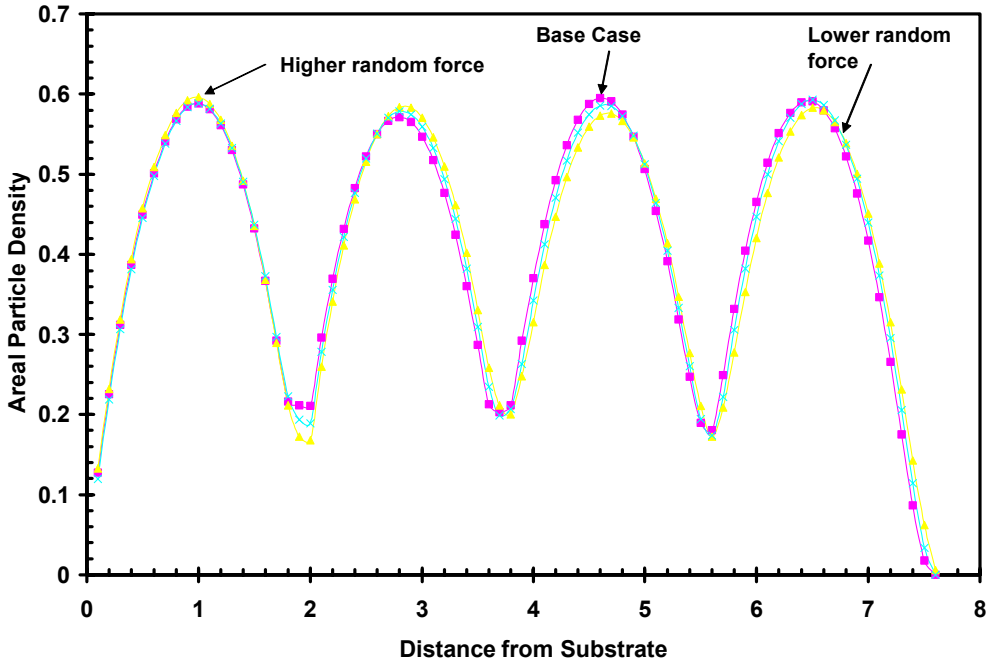

Figure 4.13 Areal density plots for three different magnitudes of random force variance at times a) $\tau = 40.8$; b) $\tau = 42.5$. Distance is in units of particle radii.

used, the net force on the particle increases and thereby the time scale of particle motion increases resulting in higher time available for particles to order themselves before the layers merge. This results in a better packing obtained at a given time compared to the base case. Figure 4.14 (a) shows an FCC structure with each layer representing the (1 0 0) plane of the unit cell. This unit cell structure is compatible with the size of the computational cell. At time τ = 41.6, when the number of layers is still five, the structure remains FCC but with better ordering. When the number of layers decreases to four, the particle ordering is disturbed as seen in (c) at time τ = 42.5. The FCC structure is restored at time τ = 43.2. The layers still correspond to the (1 0 0) planes of the unit cell. When the number of layers decreases to three at time τ = 44.7, the FCC structure is retained but the layers now represent the (1 1 1) planes. When the size of the unit cell is calculated using the inter-layer distance, the cell size is obtained as 2.77 in dimensionless units. This is approximately the same as the one obtained for the base case at same volume fraction.

Thus, when the magnitude of random force is increased, FCC is the only compatible structure obtained with increase in volume fraction. Also, the particles would have sufficient time to move to lattice points which give better ordered packing structure compared to the base case. For the case of five and four layers, the layers represent the (1 0 0) plane of the FCC cell and for the case of three layers, the layers represent the (1 1 1) plane.

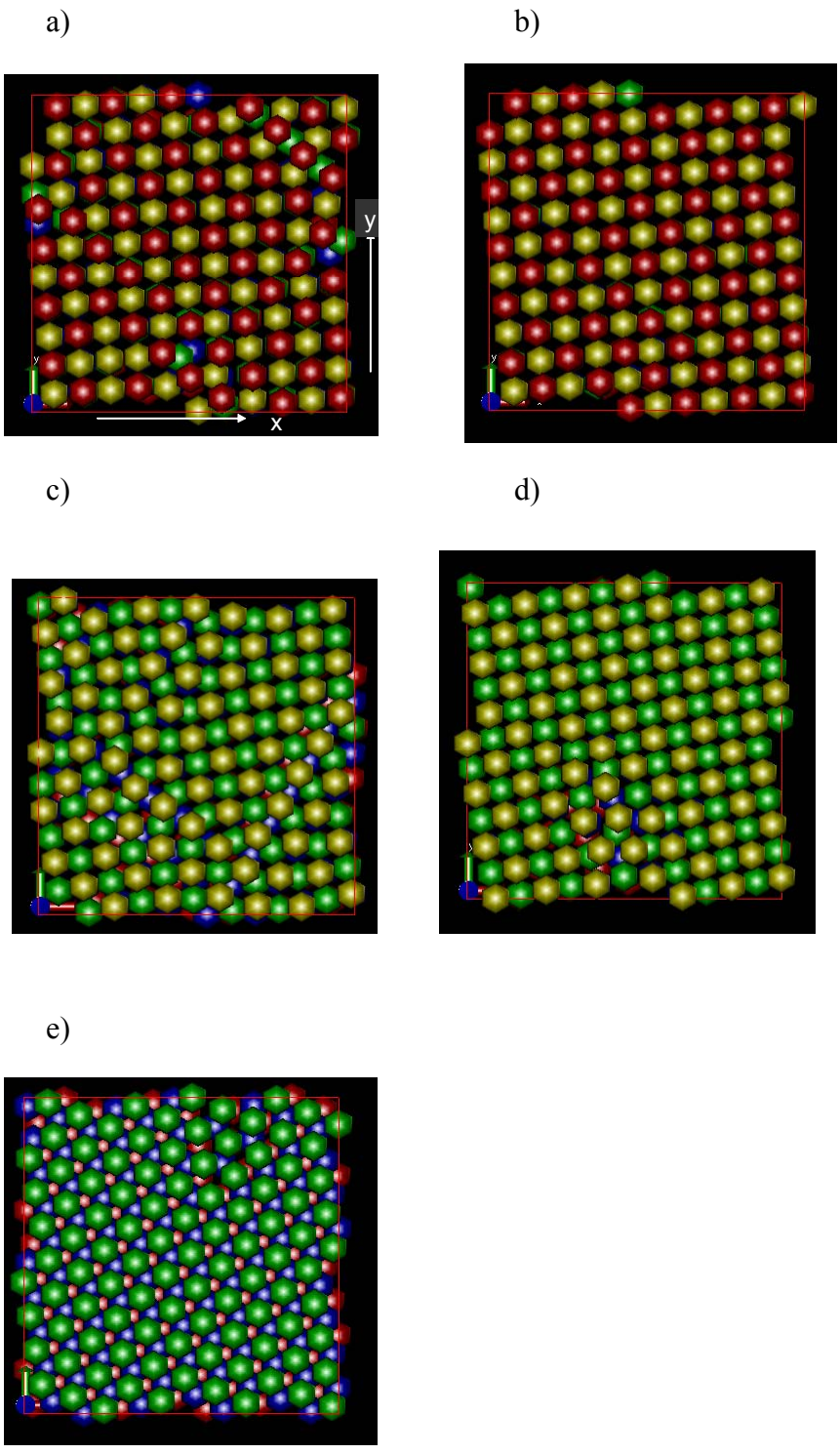

Figure 4.14 Particle packing top views for the case of higher random force seen at five instants during drying: a) τ = 40.8 (five layers), b) τ = 41.6 (five layers), c) τ = 42.5 (four layers), d) τ = 43.2 (four layers), and e) τ = 44.7 (three layers). The particles are colored only to aid the reader in identifying different layers.

4.7 Influence of Drying Rate on Particle Packing and Layering

The rate at which drying occurs during Stage I of film formation plays an important role in the evolution of particle layers and packing. Experimental evidence shows that latex systems dried slowly produce better packings compared to those obtained from faster drying. In the present model, the drying rate is changed by changing the velocity of the air-water interface. For the base case, the value used was 10^{-5} m/s. Parametric analysis is made by using a higher value (10^{-4} m/s) for the air-water interface velocity.

Figure 4.15 shows the areal density plots for the base case and faster drying case at two different times during the initial phase of Stage I: a) τ = 7; b) τ = 12. From Figure (a) shows that the areal density peak close to the air-water interface increases from 0.22 to 0.28 when the drying is faster. This is because, with faster drying, the magnitude of Peclet number (ratio of evaporation rate to diffusion rate) increases from 489 to 4890 i.e. the air-water interface moves at a much shorter time scale than the diffusivity time scale. This results in accumulation of more particles compared to the base case and this is reflected in the increase in the areal density. Figure 4.15 (a) also shows that for the case of faster drying, the peak corresponding to the particles stuck to substrate has decreased and thereby the depletion seen at a distance of two particle radii from substrate has also decreased. This can be explained using the random force that causes depletion. For the case of faster drying, the decrease in the time scale for evaporation has the net effect of decreasing the magnitude of the forces (columbic and random forces) acting on the particles (based on the scaling). This lowering of magnitude of random force causes lesser number of

a)

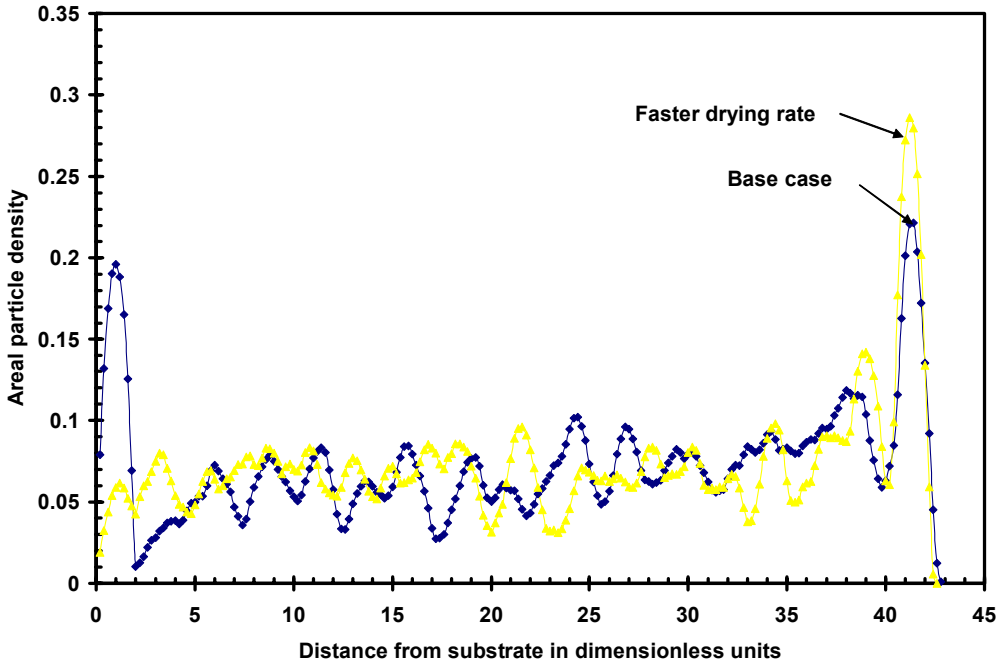

b)

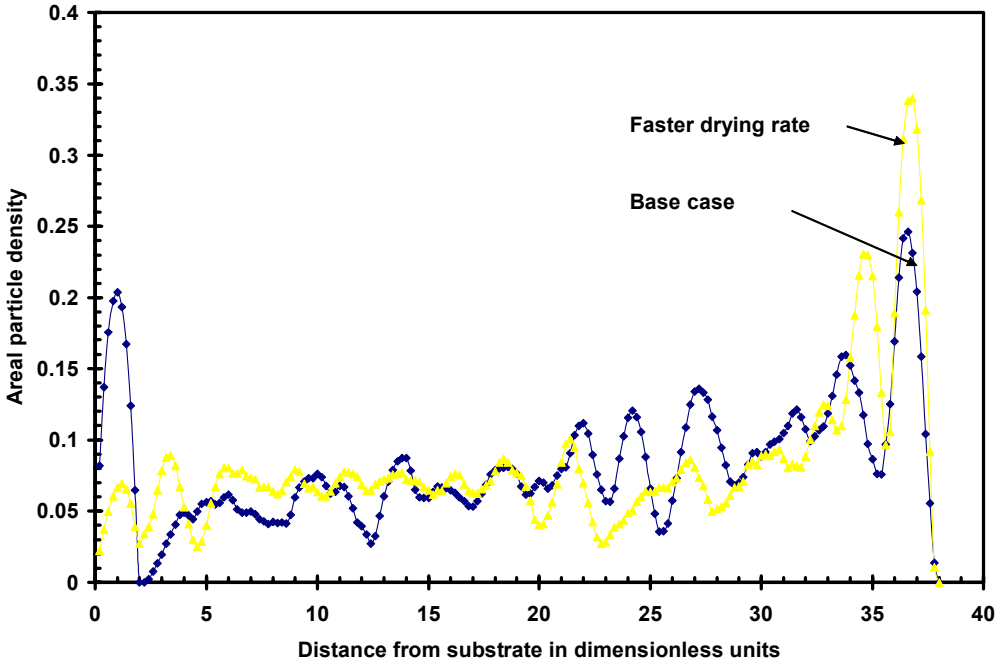

Figure 4.15 Areal density plots for base case ($V_s = 10^{-5}$ m/s) and for the case of faster drying rate ($V_s = 10^{-5}$ m/s) at times: a) $\tau = 7$; b) $\tau = 12$

a)

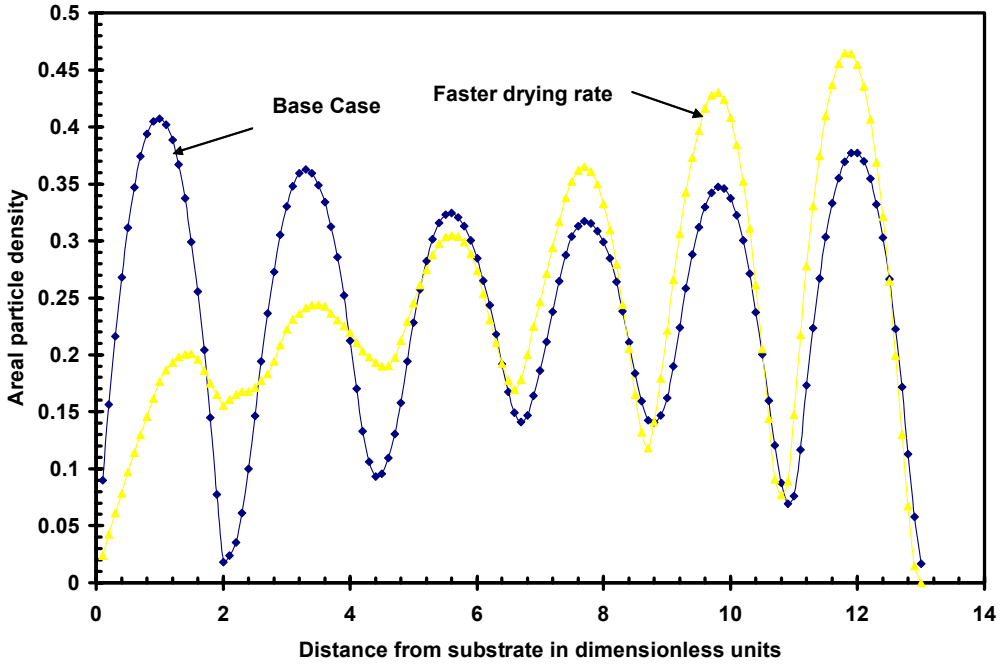

b)

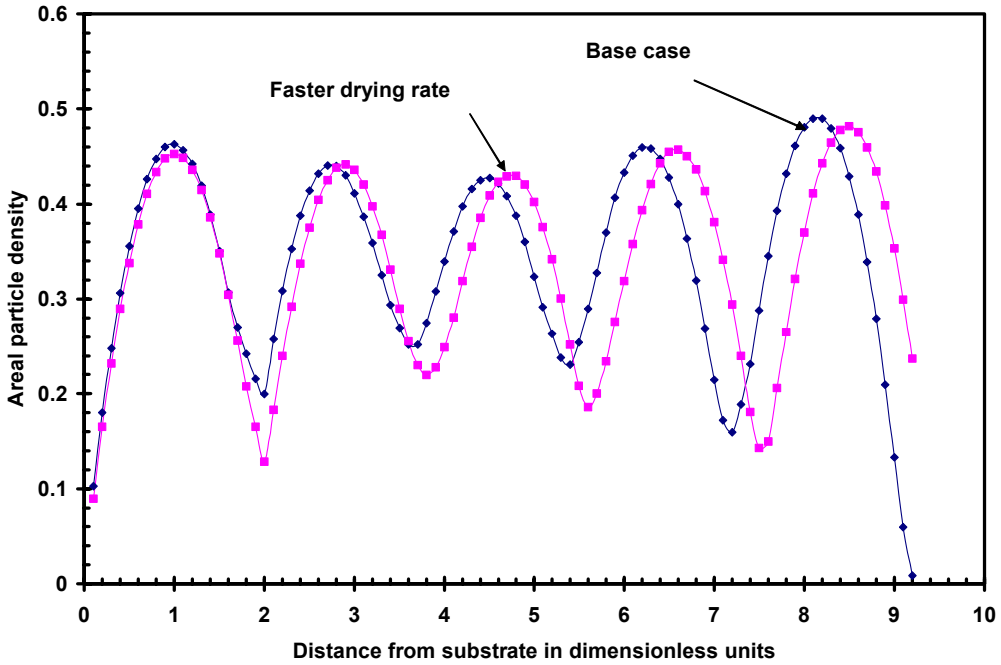

Figure 4.16 Areal density plots for base case ($V_s = 10^{-5}$ m/s) and for the case of faster drying rate ($V_s = 10^{-5}$ m/s) at times: a) $\tau = 37$; b) $\tau = 40.8$

particles to hit the substrate and get stuck and thereby causes lesser depletion at distances slightly away from substrate.

During the later phase of drying, when layers from due to increasing repulsions, the lowering of the magnitude of the columbic forces due to faster evaporation rate has the effect of producing less distinct layers at the same volume fraction. This is can be seen from the areal density plot made at time τ = 37 (Figure 4.16 (a)). Base case shows six distinct layers but faster evaporation rate does not produce proper layers at the bottom part of the computational cell. This effect of drying rate on particle layering becomes less prominent when the columbic repulsions become relatively stronger. This can be seen from Figure 4.16 (b) made at time τ = 40.8.

Figure 4.17 shows the top views of particle packing obtained from base case and using faster drying rate at two different times: τ = 42.5 (4 layers) and τ = 44.4(3 layers). It can be seen that at τ = 42.5, faster drying rate has produced a disordered packing structure compared to the HCP structure obtained for the base case, due to insufficient time available for particle arrangement. But at τ = 44.4, the time available for particles to arrange is sufficient enough even for the faster drying rate. This is seen from the FCC packing structure obtained in both cases. The layers represent the (1 1 1) plane of FCC cell. For the case of faster drying rate, the distance between layers is approximately 1.8 in dimensionless units, giving a cell size of 3.11. This is close to the 3.08 cell size obtained for the base case. So, it can be inferred that if FCC packing is needed at a volume fraction of 0.56 (corresponding to 2.22 s), air-water interface velocity of 10^{-4} m/s is good enough and slower drying is not needed.

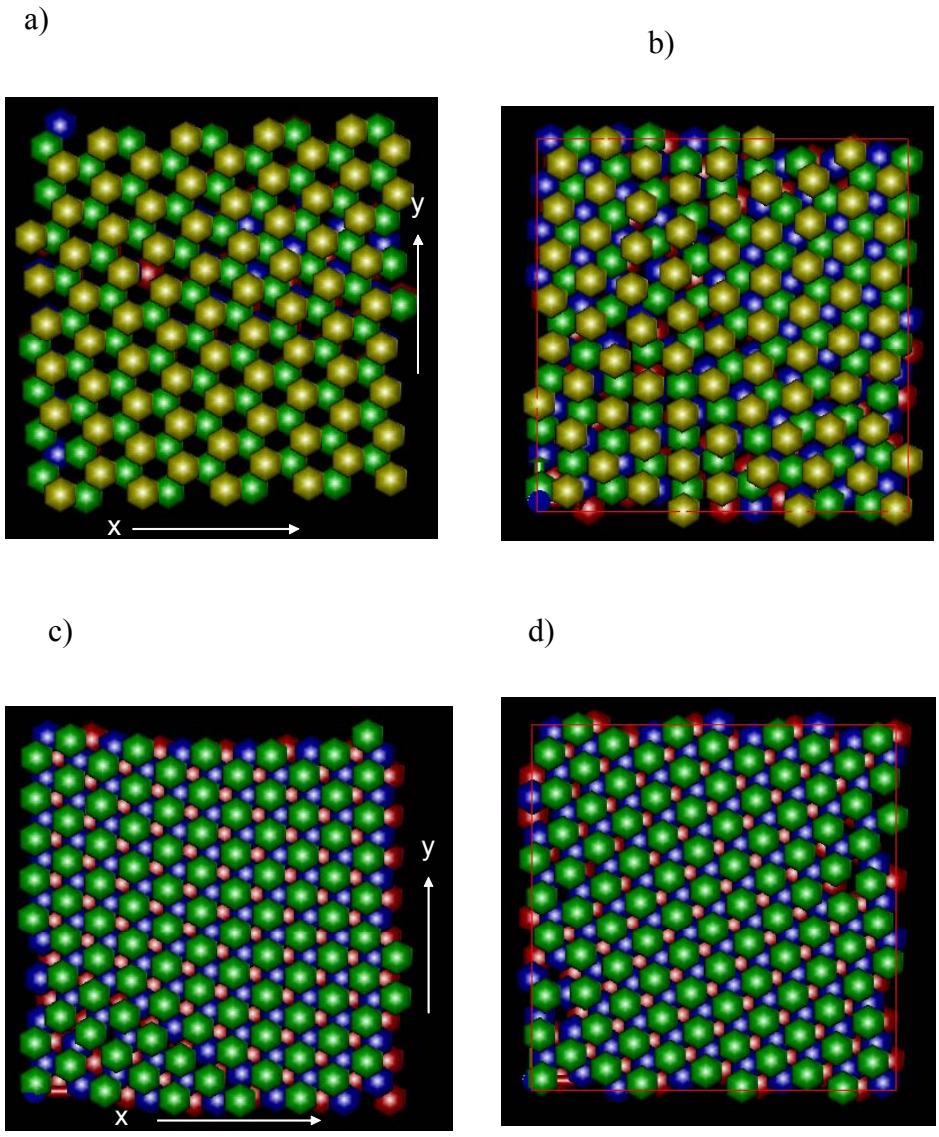

Figure 4.17 Comparison of top views of particle packing for base case (a) and c)) and faster drying rate (b) an d)) at times: τ = 42.5 (a) and b)) and τ = 44.4 (c) and d)). Particles are colored only to aid the reader in identifying layers.

4.8 Influence of Particle Size on Particle Packing and Layering

Particle size in a latex dispersion has an important role to play in evolution of particle layers and packing. In the present analysis, double the particle size used in the base case is used to see the influence of higher particle size. In the present modeling analysis, based on the governing equations for random force and columbic repulsions,

increasing the particle size has the effect of decreasing the magnitude of both random force and columbic repulsions. Thus areal density plot during the initial phase of Stage I shows that the peak close to air-water interface increases with increase in particle size and the peak close to substrate decreases with increase in particle size. The same argument used in Section 4.7 holds here. This is seen from Figure 4.18 plotted at time $\tau = 7$.

As the net columbic forces decrease with increase in particle size, the layers formed using larger particle size are not as distinct as for the case of lower particle size (base case) at a given time (or volume fraction). This is seen from Figure 4.19 (a) plotted at time $\tau = 37$. But as the particles approach closer and closer, this effect of particle size decreases resulting in lesser difference in layers observed between base

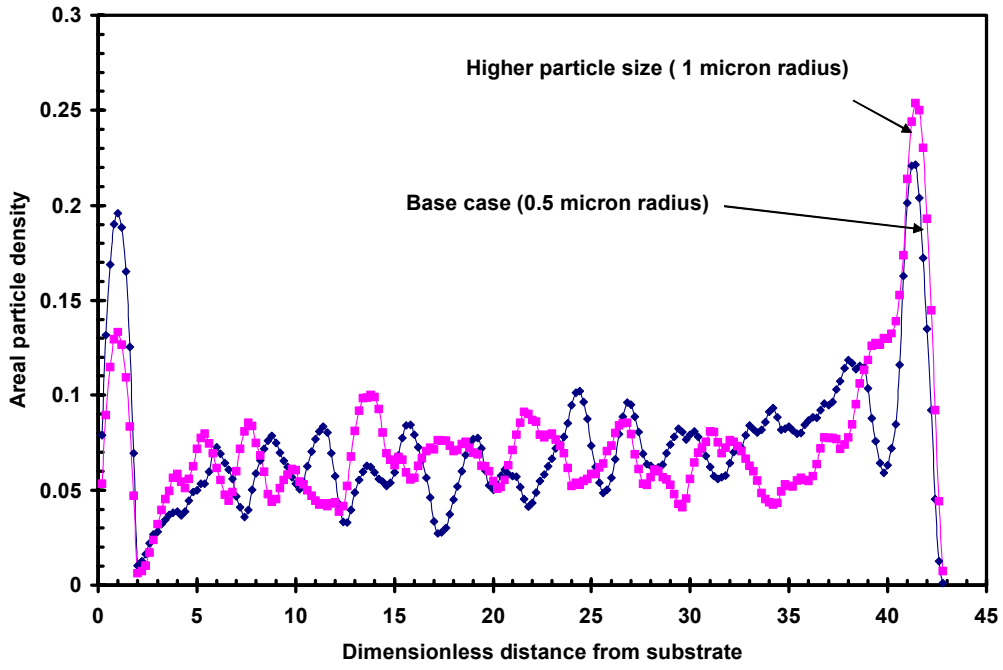

Figure 4.18 Comparison of areal density plots for different particle sizes at time $\tau = 7$

a)

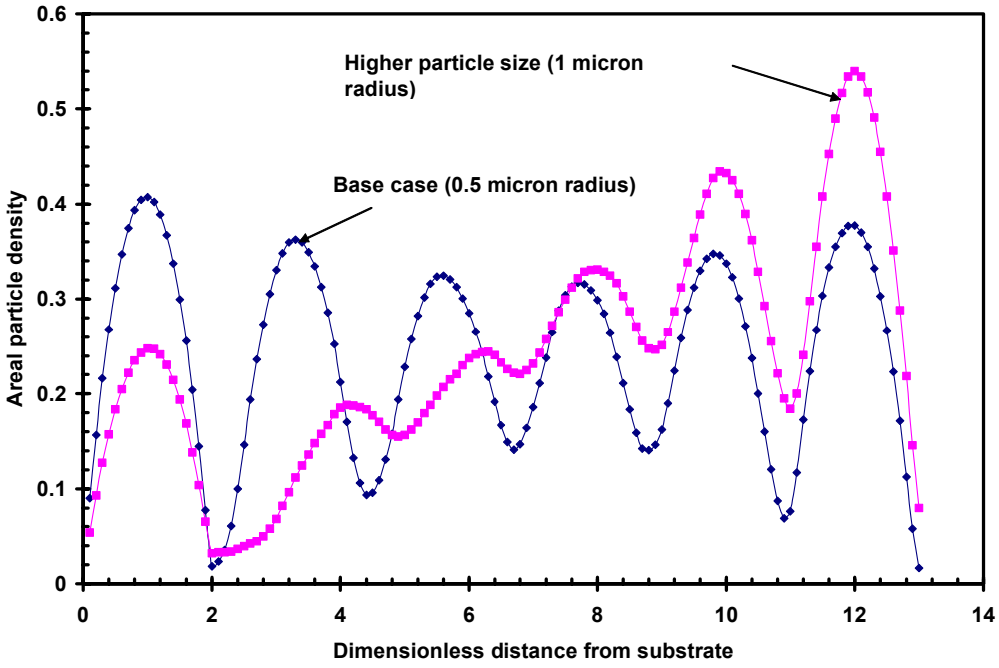

b)

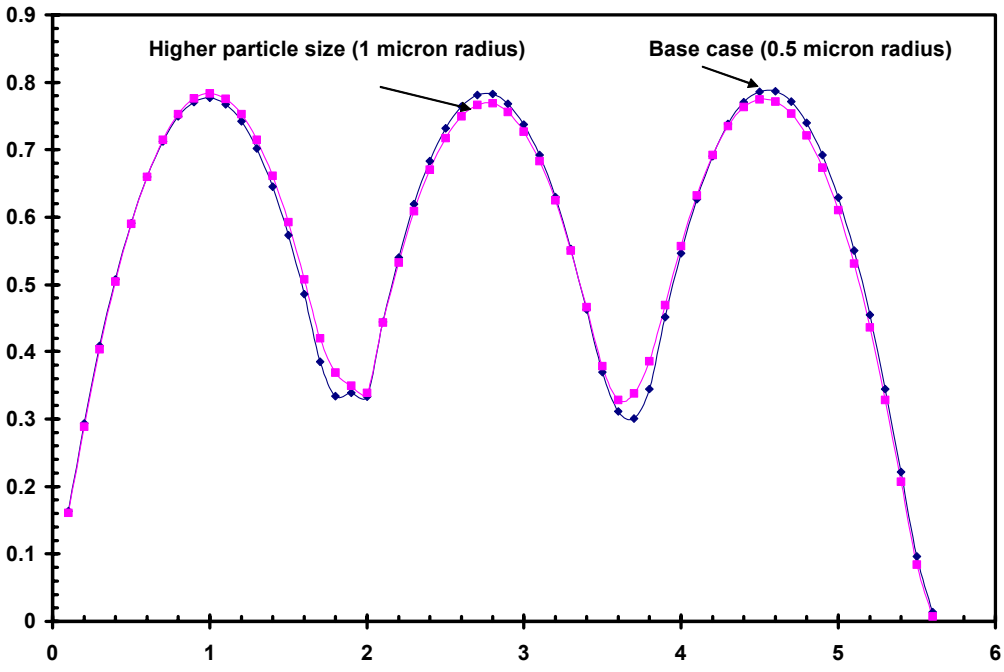

Figure 4.19 Comparison of areal density plots for two different particle sizes at times: a) $\tau = 37$; b) $\tau = 44.4$.

case and higher particle size. This can be seen from Figure 4.19 (b) plotted at time τ = 44.4.

Comparison of packing structures obtained using half micron particle radius (base case) and one micron particle radius indicates that for the case of higher particle size, the time available for particles to find stable lattice positions is very short resulting in a disordered packing even when only three particle layers exist (Figure 4.20). This is different from the case of higher evaporation rate discussed in Section 4.7, where, though no ordered packing was seen for four layers, FCC structure was obtained for three layers. This shows that doubling the particle size has greater influence on particle packing than increasing the evaporation rate by ten times.

4.9 Influence of Electrolyte Concentration on Particle Packing and Layering

Experimental work on Stage I of film formation has shown that electrolyte concentration in the latex system plays an important role in determining the kind of packing structure obtained. Use of higher electrolyte concentration decreases the screening length (from equation 2.14), thereby resulting in lower magnitude of effective columbic repulsions between particles. In the present analysis, the screening length is decreased by four times to see its influence on layering and particle packing. Figure 4.21 (a) – (c) compares areal density plots obtained using higher electrolyte concentration with those obtained for base case, at three different times. At times τ = 12 and τ = 37, the particle density close to air-water interface is higher for high electrolyte concentration, though the Peclet number is the same. This happens because, for the base case, the repulsions which are relatively higher, oppose the build up of particle density close to air-water interface. When the electrolyte concentration

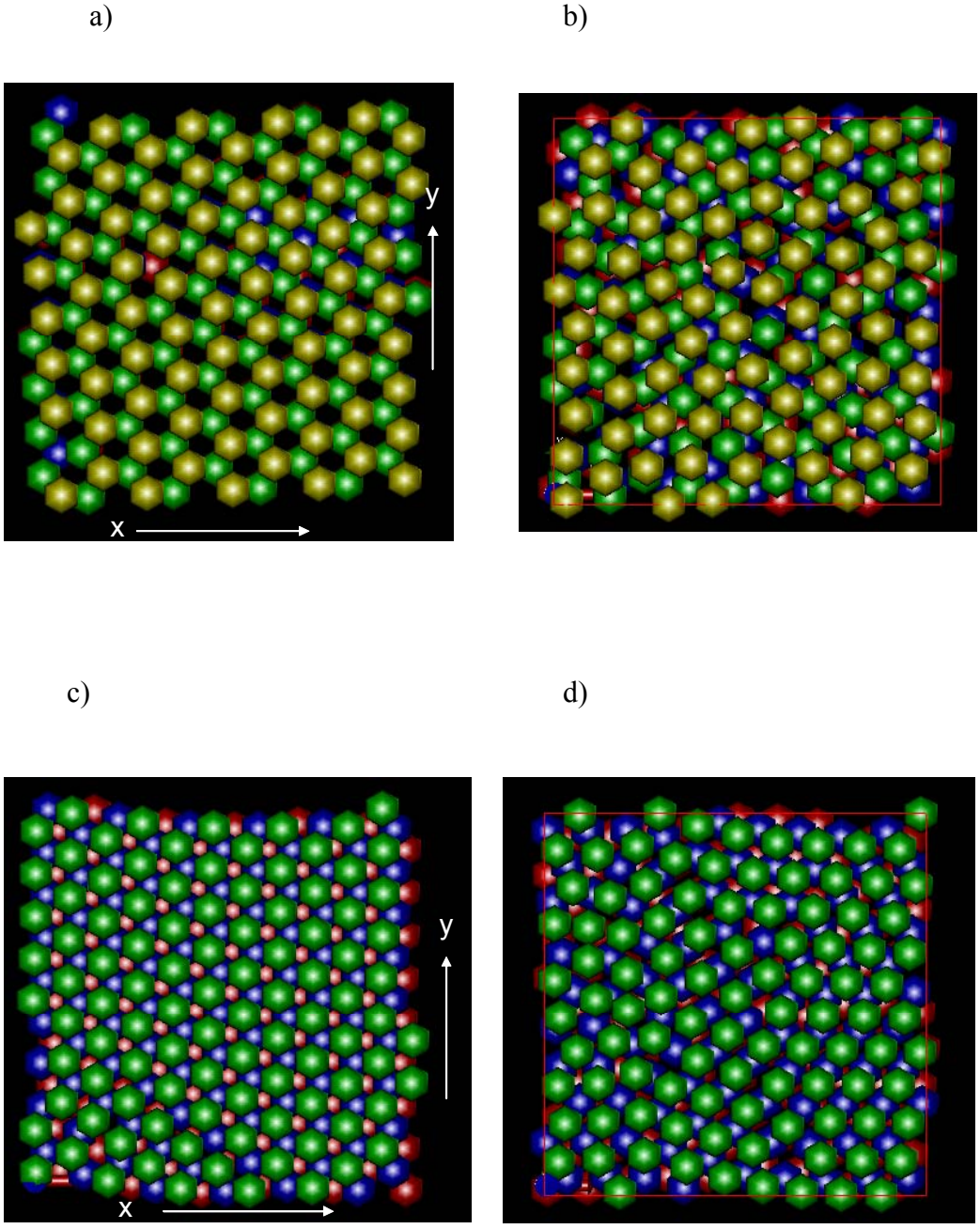

Figure 4.20 Comparison of top views of particle packings obtained using two different particle sizes a) a = 0.5 microns; τ = 42.5, b) a = one micron; τ = 42.5, c) a = 0.5 microns; τ = 44.4, and d) a = one micron; τ = 44.4. Particles are colored only to aid the reader in identifying layers.

a)

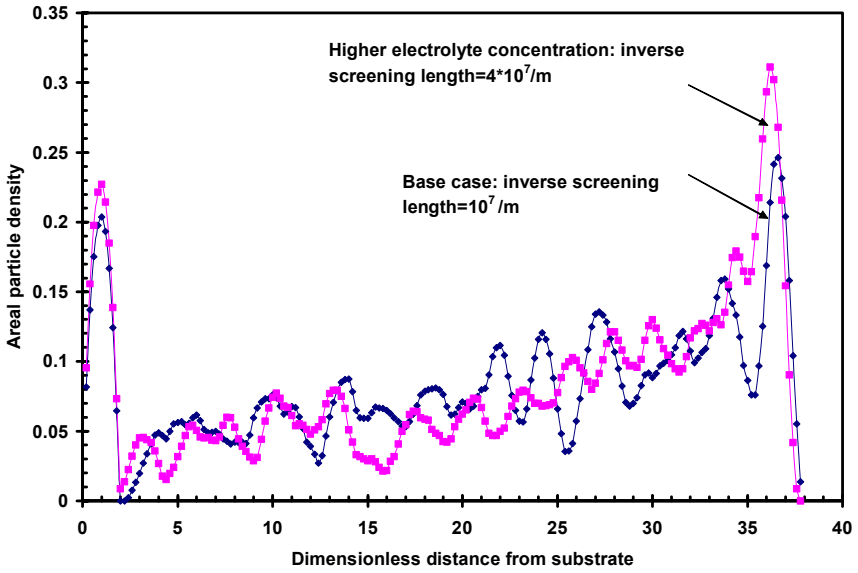

b)

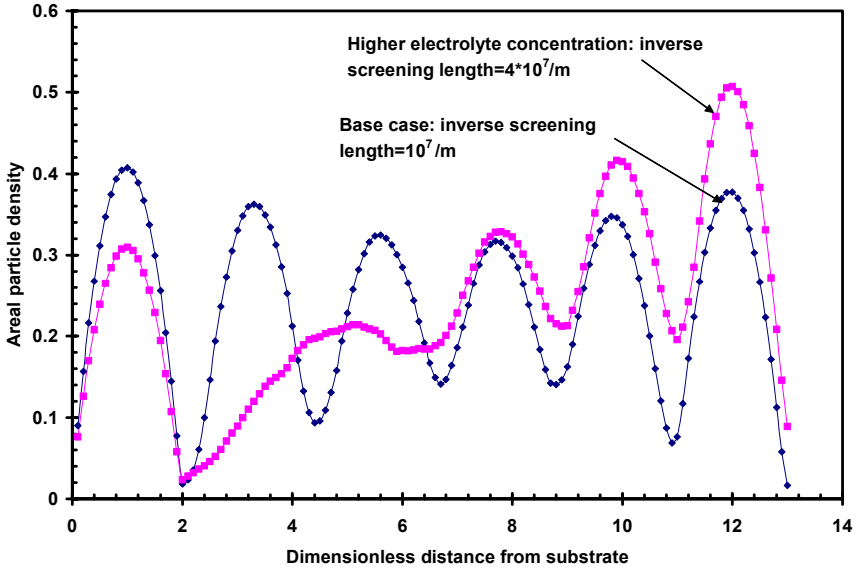

c)

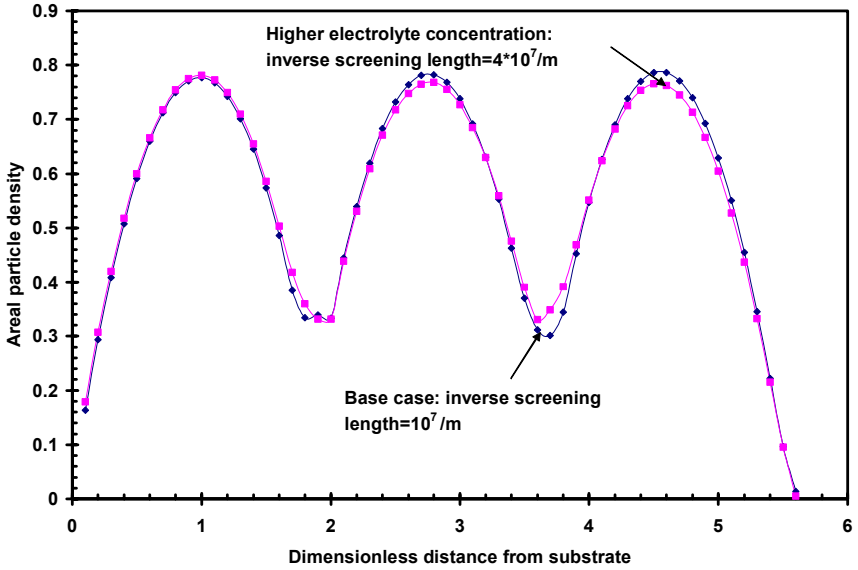

Figure 4.21 Comparison of base case and high electrolyte concentration areal density plots at times: a) 12; b) 37; c) 44.4.

a) b)

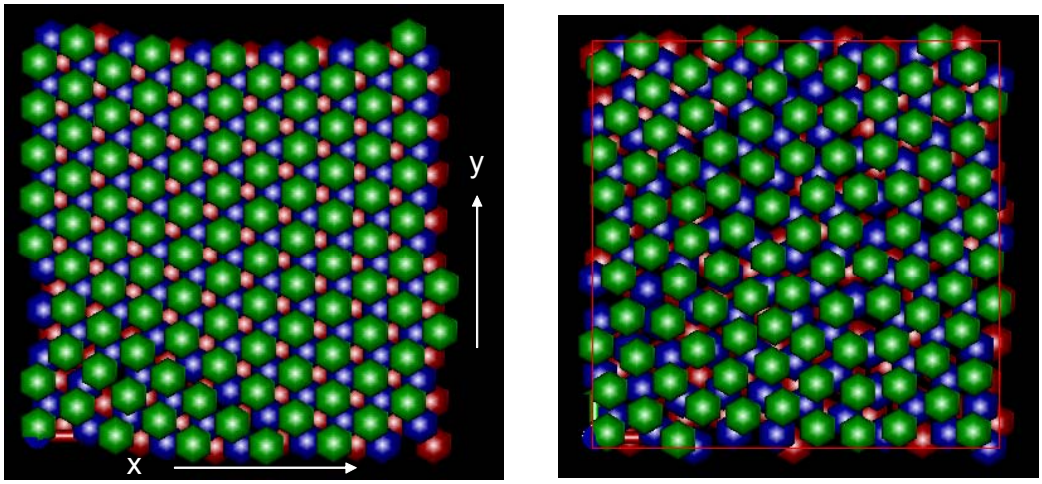

Figure 4.22 Top views obtained at time τ = 44.4, for base case (a) and higher electrolyte concentration case (b). Particles are colored only to aid the reader in identifying layers.

is high, the repulsions are weaker and there is little that resists the particle density build up. It should be noted that in the present simulations, the electrolyte concentration and thereby the screening length is assumed to be constant throughout the drying period. In real situations, the electrolyte concentration increases as volume fraction of water decreases. The present model can be further improved by considering variable screening length.

At time τ = 37, when the base case shows six almost distinct layers, the higher electrolyte concentration case shows no such layers, especially in the bottom half of the computational cell where the particle density is less. This is due to the weak repulsions existing between the particles for the case of higher electrolyte concentration. At time τ = 44.4, the particles come close enough so that the gap between base case and higher electrolyte concentration case decreases due to increasing electrolyte concentration. This is seen from Figure 4.21 (c).

Comparison of top views (Figure 4.22) obtained for base case and higher electrolyte concentration at τ = 44.4, shows that in the latter case, the time available for particles is not long enough to find stable lattice positions even when only three layers exist.

Thus increasing the electrolyte concentration has similar influence on particle packing as increasing the particle size. The next chapter summarizes the conclusions that were drawn from the base case and parametric analysis and discusses the recommendations for future work.

Chapter 5: Conclusions and Recommendations

5.1 Conclusions

The particle mechanics model developed in Chapter 3 was used to analyze the evolution of particle layers and ordered packing structure with increase in particle volume fraction during Stage I of film formation. The base case analysis showed that increasing volume fractions result in the transformation of an aqueous dispersion containing discrete polystyrene latex particles into an ordered packing structure with discrete layers. The evolution of particle layers does not occur until near the end of the drying period. Distinct internal layers can be seen only after approximately 80% of the drying time. This is due to the columbic repulsions being too weak to cause layer formation during this early phase.

Areal density plots and 3-D views of particle packing show that early in Stage I of drying, a top layer forms due to surface tension force, and a bottom layer forms due to a combination of random force and impermeable substrate condition. During the early phase, higher particle density is also seen at distances close to the air-water interface. This is due to the high Peclet number (a ratio of evaporation rate to diffusivity rate) i.e. the evaporation time scale is much smaller than diffusivity time scale. Increasing the magnitude of random force (Brownian diffusivity), decreasing the rate of evaporation, and decreasing the particle size result in lower particle density at air-water interface compared to base case. This occurs due to decrease in Peclet number. The particle density of the bottom layer (a result of random force and impermeable substrate condition) decreases with decrease in random force, increase in evaporation rate, and increase in particle size.

During the later phase of Stage I, when columbic repulsions dominate over random force, evolution of layers starts. For the base case, at $\tau = 37$, six distinct layers are formed. With increase in volume fraction, as inter-layer repulsions dominate over intra-layer repulsions, merging of layers occurs. The simulations were carried until three layers are formed. This occurs at $\tau = 44.4$ for the base case. Because of equal charge present on all particles, the particles tend to distribute uniformly between all the layers at any instant. The layers also tend to maintain equal distance between them.

Top views of particle packing seen during later phase of drying for base case show that an ordered packing structure can be seen only after four layers are formed. The packing transforms from a HCP structure to FCC structure (the layers represent the (1 1 1) plane) when four layers merge to form three layers. The dimensions of the unit cell show that FCC structure is compatible with the overall size of the computational cell. The prdections from the model are in agreement with the experimental observations made by He et al. (1996) and Monovoukas et al. (1988), which showed the formation of FCC/HCP structures at end of Stage I.

The change in the packing structure and layering with changes in some parameters involved in the model was also analyzed. The initial particle distribution used for the simulation had no significant influence on the layering or packing structure obtained. When the magnitude of the random force is increased better packing structures were seen because of the longer time available for particles to find stable lattice points. The layering phenomenon during the later phase of Stage I was similar to that of the base case because magnitude of repulsions remains unchanged.

Using a faster drying rate resulted in disordered packing when four layers were present, but as merging occurs and three layers form, FCC structure was observed. This indicates that when the particle volume fractions become sufficiently high, the columbic repulsions become strong enough to produce ordered packing, thus nullifying the effect of faster drying rate. Using a higher particle size showed that a disordered structure is obtained even when only three layers exist and particle volume fractions are high. This indicates that doubling the particle size has greater influence on particle packing than increasing the drying rate by ten times.

Using higher electrolyte concentration reduces the effective screening length, thereby reducing the net columbic repulsions. Comparison of areal density plots with base case showed that layers are less distinct compared to base case. The packing structure obtained was also disordered showing that the time scale for particle motion is small for any ordering to be seen.

Overall, the model developed in this thesis included most of the mechanics relevant to latex systems. It can be readily used to get rough estimates of the operating parameters that would be needed to obtain long-range (few tens of microns) ordered packing. The parametric analysis presented in this thesis helps identify the conditions under which assumption of the existence of a close packed FCC structure at start of Stage II can be made.

5.2 Recommendations for Future Research

A major limitation in this model is the neglecting of particle collisions, which may result in sticking or elastic rebound in practical systems. Including particle collisions by imposing contact boundary conditions (using either elastic collision laws or sticking condition laws) would bring the model close to applicability in practical systems. In practical systems, the substrate may also have a charge on it. Considering the interactions between particles and charged substrate could also be a useful addition to the model. This would help in understanding the influence of charged substrate on particle packing. A major computational challenge in dealing with the present model is to reach volume fractions close to 0.74 maintaining multi layers. This would be possible using much more number of particles for the simulation. Then hydrodynamic interactions and Van der Waals attractions would also have to be taken into account, which are neglected in the current analysis.

In the present model, the screening length was assumed to be constant during drying. But in real systems, as water evaporates the concentration of electrolytes increases and the screening length changes. The evolution of electrolyte concentration with drying could be a useful study that can be made. If the evolution of electrolyte concentration with drying is considered, the model may predict less ordering of particles because of the decreasing of electrostatic interactions with increase in electrolyte concentration.

In practical systems, the latex dispersions are generally poly-disperse. Our parametric analysis showed that particle size plays an important role in determining the type of packing obtained. So, studying the evolution of layers and packing

structure for a poly-disperse system would be a useful exercise. As the simulations showed that increasing the particle size results in a less ordered packing, we can expect the polydisperse system to evolve into a packing containing ordered and disordered phases. DLVO theory can still be used to predict the columbic repulsions, but a different equation should be used when $ka << 1$.

In a major extension of this study, the packing structure obtained from the simulations can be used as starting point to develop a model to predict deformation during Stage II of film formation.

Experiments could also be conducted to verify the accuracy of the present model. Investigation can be made using ESEM, AFM, etc. to see the type of packings obtained. Theoretically, the accuracy can be verified by changing the time-step control parameter, changing the simulation cell size, etc.

So the improvements that could implemented with little changes to the model would be, extending the study to poly-disperse systems, including Van der Waals interactions, and accounting for the evolution of electrolyte concentration with drying. Including hydrodynamic interactions and imposing sticking or elastic rebound boundary conditions need some major changes to the existing model.

Bibliography

Batchelor, G.K. "Brownian Diffusion of Particles with Hydrodynamic Interaction", Journal of Fluid Mechanics, **74 (1)**, p 1-29, 1976.

Brown, G.L. "Formation of Films from Polymer Dispersions", Journal of Polymer Science, **22**, p 423-434, 1956.

Butt, H.J., Kuropka, R., and Christensen, B. "Latex Film Formation Studies with the Atomic Force Microscopy: Influence of Aging and Annealing", Colloid and Polymer Science, **272**, p 1218-1223, 1994.

Croll, S.G. "Drying of Latex Paint", Journal of Coatings Technology, **58 (734)**, p 41-49, 1986.

Dillon, R.E., Matheson, L.A., Bradford, E.B. "Sintering of Synthetic Latex Particles", Journal of Colloid Science, **6**, p 108-117, 1951.

Dingenouts, N., and Ballauff, M. "Assessment of Spatial Order in Dried Latexes in Small Angle X-ray Scattering", Macromolecules, **31**, p 7423-7429, 1998.

Dobler, F., Pith, T., Lambla, M, and Holl, Y. "Coalescence Mechanism of Polymer Colloids II. Coalescence with Evaporation of Water", Journal of Colloid and Interface Science, **152**, p 1-12, 1992.

Eckersley, S.T., and Rudin, A. "Drying Behavior of Acrylic latexes", Progress in Organic Coatings, **23**, p 387-402, 1994.

Hastings, C. Jr., "Approximations for Digital Computers", Princeton, NJ: Princeton University Press, 1955.

He, C. and Donald, A.M. "Morphology of Core-Shell Morphology Lattices During Drying", Langmuir **12**, p 6250-6256, 1996.

Humphrey, W., Dalke, A. and Schulten, K., "VMD - Visual Molecular Dynamics", Journal of Molecular Graphics, **4**, p 33-38, 1996.

Joanicot, M., Wong, K., Maquet, J., Chevalier, Y., Pichot, C., Graillat, C., Lindner, P., Rios, L., and Cabane, B. "Ordering of Latex Particles During Film Formation", Progress in Colloid and Polymer Science, **81**, p 175-183, 1990.

Keddie, J.L., Meredith, P., Jones, R.A.L., and Donald, A.M. "Kinetics of Film Formation in Acrylic Latexes Studied with Multiple-angle-of-incidence Ellipsometry and Environmental SEM", Macromolecules, **28,** p 2673-2682, 1995.

Keddie, J.L, Meredith, P., Jones, R.A.L, and Donald, A.M. "Rate-Limiting Steps in the Film Formation of Water-borne Acrylic Lattices as Elucidated with Ellipsometry and Environmental SEM", Journal of Material Science and Enggineering, **73**, p 90-91, 1996.

Lamprecht, J. "New Criterion for Film Formation in Aqueous dispersions of Polymers", Journal of Colloid and Polymer Science, **258 (8)**, p 960-967, 1980.

Mason, G. "Formation of Films from Latex Films: a Theoretical Treatment", British Polymer Journal, **5**, p 101-108, 1973.

Monovoukas, Y. and Gast, A.P. "The Experimental Phase Diagram of Charged Colloidal Suspensions", Journal of Colloid and Interface Science,**128**, p 533, 1988.

Press, W.H., Teukolsky, S.A., Vetterling, W.T., Flannery, B.P. Numerical Recipies in C, Cambridge University Press, Cambridge, 1996.

Pusey, P.N., Van Megen, W., Barlett, P., Ackerson, B.J., Rarity, J.G., and Underwood, S.M. "Structure of Crystals of Hard Colloidal Spheres", Physical Review Letters, **63**, p 2753, 1989.

Qi Liao, Liusheng Chen, Xiaozhong Qu, and Xigao Jin, "Brownian Dynamics Simulation of Film Formation of Mixed Polymer Latex in the Water Evaporation Stage", Journal of Colloid and Interface Science, **227**, p 84-94, 2000.

Richard, B.W., and Sharif A.O, "Long-range Electrostatic Attraction Between Like-charge Spheres in a Charged Pore", Nature, **393(n6686)**, p 663-665, 1998.

Robbins, M.O., Kremer, K., and Grest, G.S. "Phase Diagram Applied to Yukawa Systems", Journal of Chemical Physics, **88 (5),** March 1988.

Routh, A.F., and Russel, W.B. "Horizontal Drying Fronts During Solvent Evaporation from Latex Films", AICHE Journal, **44 (9)**, p 2088-2098, 1998.

Sheehan, J.G, Takamura, K., Davis, H.T, and Scriven, L.E. "Microstructure Development in Particulate Coatings Examined with High Resolution, Cryogenic Scanning Electron Microscopy", Tappi Journal,**76 (12)**, p 93-101, 1993.

Turq, Lantelme, and Friedman. "Brownian Dynamics Applied to Ionic Solutions", Journal of Chemical Physics, **66(7),** 1977.

Vanderhoff, J.W. "Mechanism of Film Formation of Latexes", British Polymer Journal, **2**, p 161-172, 1970.

Van De Ven. Colloidal Hydrodynamics, Acadenic Press Inc, San Diego, 1988.

Voyutskii, S.S. “Amendments to the Papers by Bradford, Brawn and Co-worker, Concerning Mechanisms of Film Formation from High Polymer Dispersions”, Journal of Polymer Science, **32 (125)**, p 528-530, 1958.

Appendix: Computer Program for Predicting Particle Motion

/* This is a program for predicting particle motion in stage I of film formation of latex coatings. The code contains: 1) a main program that involves incrementing the time step and updating the particle positions; 2) a Sub-routine that evaluates the net force acting on a particle at a given time step; 3) a Sub-routine ran1() for generating uniformly distributed random numbers between 0 and 1. The code uses Forward Euler's Technique with time automatic step control. The code was run on a 12 processor machine with X-Win 32 interface. The input parameters are contained in the sub-routine that calculates net force on a particle. The 50000 initial dummy particle positions are contained in the text file named, randnum_420. After compiling and building, at the prompt on the screen, 1 should be entered for nm (Numerical method) and 3 should be entered for rt (repulsion type). */

```
#define NP 300    // 300 particles are considered
#define ND 3      // 3 Dimensional motion is considered
#define NI 500000  // Total number of time steps
#define ERROR_CRIT 0.5   /*   Max displacement of any
   particle in any direction in one time step is 0.5 */
#define t_p 50000   /* Initially 50000 dummy
   particle positions are considered   */
#define num_part 300

#include <stdlib.h>
#include <stdio.h>
#include <math.h>
#include "nr.h"

#define sub_cell_size 4.0
#define max_part_cell  30   /*  Maximum particle number in
   a sub-cell */
#define N_C_x 5   // Number of sub-cells in x direction
#define N_C_y 5   // Number of subcells in y direction
#define MIN_DIST 3.0       /* Initially all particles are
   seperated by atleast 3.0 */

/* Parameters to be defined for generating random numbers
   using ran1()  */
#define IA 16807
#define IM 2147483647
#define AM (1.0/IM)
#define IQ 127773
#define IR 2836
#define NTAB 32
#define NDIV (1+(IM-1)/NTAB)
#define EPS 1.2e-7
#define RNMX (1.0-EPS)

long seed=-2010; /* Initial input to random number
   generator,ran1() */
```

```
int main()
{
   int nm,rt,brkval = 0,z0=50,x0=20,eta1,eta2,eta3,eta4,k,l;
   double value,w=0,eta_new[NP][ND],vel[NP][ND];
   double alpha,eta_displ[NP][ND],eta_predict,h,gap[NP],
      eta_old[NP][ND],w_half;
   double K[ND],v[NP][ND],sqdist,dist[NP][NP],
      invdist[NP][NP],great_displ, h_old, force[ND];
   int cell_num_x=0,cell_num_y=0,
      part_in_cell[N_C_x][N_C_y][max_part_cell];
   int n,m,i,j,count,dummy, n_read = 0, NI_10,print_num;
   double eta_dummy[ND]={0},dist_dummy,sqdist_dummy,
      min_dist,eta_curr[NP][ND]={0};

   /* Declaration of function that calculates the force on a
      particle */
   void fun_phi(double,double,double [NP][3],int,int, int,
      int [N_C_x][N_C_y][max_part_cell],
      int,int,double [ND]);

   // output data files
   FILE *data1_value;
   FILE *data2_value;
   FILE *data3_value;
   FILE *data4_value;
   FILE *data5_value;
   FILE *data6_value;
   FILE *data7_value;
   FILE *data8_value;
   FILE *data9_value;
   FILE *data10_value;
   FILE *data16_value;
   FILE *data17_value;
   FILE *randnum_420part;   /* input data file for dummy
      particle positions  */
   FILE *in_31p;    /* file for storing actual initial
      particle positions  */
   FILE *min_file;  /* file for storing the inter-particle
      distances of dummy particles*/

   // File opening
   randnum_420part=fopen("randnum_420part.txt","r");
   min_file=fopen("min_file.txt","w");
   in_31p=fopen("in_31p.txt","w");

   //  Start of assigning initial particle positions
   /* put first particle in current list  */
   NI_10=NI/10;
   for (j=0; j&lt;ND; j++)
   {
      fscanf(randnum_420part, "%lf",&eta_curr[0][j]);
      printf("%f\n",eta_curr[0][j]);
```

```
   n_read++;
}

/* read in next particle from dummy file */
for (j=0; j<ND; j++)
{
   fscanf(randnum_420part, "%lf", &amp;eta_dummy[j]);
   printf("%f\n",eta_dummy[j]);
   n_read++;
}

/ * Start of for loop used for obtaining 300 initial
   particle positions from dummy particle positions */
for(count=1;count<NP && n_read<t_p;n_read++)
{
   min_dist=1.e16; /* set this as an unreasonably large
      number  */
   for(m=0;m<count && m<NP;m++)
   {
      sqdist_dummy=0;
      for(j=0;j<ND;j++)
      {
         sqdist_dummy +=(eta_curr[m][j]-
         eta_dummy[j])*(eta_curr[m][j]-eta_dummy[j]);
      }
      dist_dummy = sqrt(sqdist_dummy);
      if(dist_dummy<min_dist)
      {
         min_dist=dist_dummy;
      }
   }
   fprintf(min_file,"%lf \n",min_dist);
   if(min_dist >= MIN_DIST)
   {
      for(j=0;j<ND;j++)
      {
         eta_curr[count][j]=eta_dummy[j];
      }
      count++;
   }

   /* read in next particle from file    */
   for (j=0; j<ND; j++)
   {
      fscanf(randnum_420part, "%lf",&eta_dummy[j]);
      printf("%f\n",eta_dummy[j]);
   }
} /* close of for loop used for obtaining 300 initial
   particle positions from dummy particle positions  */

for (i=0; i<count ; i++)
{
```

```
   for (j=0; j<ND; j++)
   {
      fprintf(in_31p, "%f \n", eta_curr[i][j]);
   }
}
// end of assigning particle positions
fclose(randnum_420part);
fclose(in_31p);
fclose(min_file);

// Initialize the particle count in a cell to -1
for(i=0;i<N_C_x;i++)
{
   for(j=0;j<N_C_y;j++)
   {
      partcount_cell[i][j]=-1;
   }
}

/* Distributing particles into subcells  based on their
   co-ordinates values */
for(i=0;i<NP;i++)
{
   cell_num_x=eta_curr[i][0]/sub_cell_size; /*
      determining x direction cell number for particle */
   cell_num_y=eta_curr[i][1]/sub_cell_size; /*
      determining y direction cell number for particle */
   /* Adding one particle to the count of that
      corresponding cell */
   partcount_cell[cell_num_x][cell_num_y]=
      partcount_cell[cell_num_x][cell_num_y]+1;
   /* Assigning the global particle number to that local
      particle */
   part_in_cell[cell_num_x][cell_num_y][partcount_cell
      [cell_num_x][cell_num_y]]=i;
}

/* Assigning global nums. -1 to all unfilled
   positions in each cell */
for(i=0;i<N_C_x;i++)
{
   for(j=0;j<N_C_y;j++)
   {
      while(partcount_cell[i][j]&amp;lt;(max_part_cell-1))
      {
         part_in_cell[i][j][partcount_cell[i][j]+1]=-1;
         partcount_cell[i][j]++;
      }
   }
}
printf("enter numer. method number and repulsion type
   number\n"); // 1 for nm and 3 for rt are entered
```

```
scanf("%d %d",&nm,&rt);
if (num_part != NP)
{
   printf("wrong number of particles\n");
   exit(-1);
}
h=0.0001;
h_old = h;
// Opening of output data files
data1_value=fopen("data1.value","w");
data2_value=fopen("data2.value","w");
data3_value=fopen("data3.value","w");
data4_value=fopen("data4.value","w");
data5_value=fopen("data5.value","w");
data6_value=fopen("data6.value","w");
data7_value=fopen("data7.value","w");
data8_value=fopen("data8.value","w");
data9_value=fopen("data9.value","w");
data10_value=fopen("data10.value","w");
data16_value=fopen("data16.value","w");
data17_value=fopen("data17.value","w");
// Start of iteration loop
for(i=0;i<=(NI);i++)
{
   /*Assigning new particle positions to variables that
      store current particle positions is valid from
      2nd time step */
   if(i>0)
   {
      for(n=0;n<NP;n++)
      {
         for(j=0;j<ND;j++)
         {
            eta_curr[n][j] = eta_new[n][j];
         }
      }
   }
   value=1;
   /* reducing time step to half till error is less than
      a limit  */
   while(value==1)
   {
      if(nm==1) // Forward Euler's method
      {
         for(k=0;k<N_C_x;k++)
         {
            for(l=0;l<N_C_y;l++)
            {
               for(n=0;n<max_part_cell &&
                  part_in_cell[k][l][n] != -1;n++)
               {
```

```
            /* Calling sub-routine that calculates
               force    */
            fun_phi(w,h,eta_curr,k,l,n,
               part_in_cell,ND,rt,force);
            for(j=0;j<ND;j++)
            {
               K[j]=h*force[j];
               eta_new[part_in_cell[k][l][n]][j] =
                  eta_curr[part_in_cell[k][l][n]][j]
                  +K[j];
            }  // close of for(j=0) loop
         } // close of for(n=0) loop
      } // close of for(l=0) loop
   } // close of for(k=0) loop
} // clsoe of if(nm==1) loop

if(i>0)
{
   /* Calculating the displacement of particles
      during a time step  */
   for(n=0;n<NP;n++)
   {
      for(j=0;j<ND;j++)
      {
         eta_displ[n][j]=fabs(eta_new[n][j]-
            eta_curr[n][j]);
      }
   }

   // Finding the maximum displacement
   great_displ=eta_displ[0][0];
   for(n=0;n<NP;n++)
   {
      for(j=0;j<(ND);j++)
      {
         if(eta_displ[n][j]>great_displ)
            great_displ=eta_displ[n][j];
      }
   }
   /* Time step is made half if displacement is
      greater than the error criterion.  */
   if(great_displ>ERROR_CRIT)
   {
      h=h/2.0;
   }

   /* Once displacement is less than error
      criterion,periodicity is used to locate the
      subcells to which the particles belong and
      then the particle positions are printed to
      output files */
   if(great_displ<ERROR_CRIT)
```

```
{
   alpha=z0-(w+h);
   for(n=0;n<NP;n++)
   {
      for(j=0;j<ND;j++)
      {
         if(j!=2)
         {
            if(eta_new[n][j]>x0)
            {
               eta1=((eta_new[n][j])/x0);
               eta_new[n][j]=eta_new[n][j]-
                  eta1*x0;
            }
            else if(eta_new[n][j]<0)
            {
               eta2=((eta_new[n][j])/x0);
               eta_new[n][j]=eta_new[n][j]+
                  (1-eta2)*x0;
            }
         }
      }
   }
   for(k=0;k<N_C_x;k++)
   {
      for(l=0;l<N_C_y;l++)
      {
         partcount_cell[k][l]=-1;
      }
   }
   for(n=0;n<NP;n++)
   {
      /* determining x direction cell number for
         particle  */
      cell_num_x=eta_new[n][0]/sub_cell_size;
      /* determining y direction cell number for
         particle  */
      cell_num_y=eta_new[n][1]/sub_cell_size;
      /* Adding one particle to the count of that
         corresponding cell */
      partcount_cell[cell_num_x][cell_num_y]=
         partcount_cell[cell_num_x][cell_num_y]
         +1;
      /* Assigning the global particle number to
         that local particle */
      part_in_cell[cell_num_x][cell_num_y]
      [partcount_cell[cell_num_x][cell_num_y]]=n;
   }
   /* Assigning global nums. -1 to all unfilled
      positions in each cell */
   for(k=0;k<N_C_x;k++)
   {
```

```
   for(l=0;l<N_C_y;l++)
   {
      while(partcount_cell[k][l]<
         max_part_cell-1))
         {
            part_in_cell[k][l]
               [partcount_cell[k][l]+1]=-1;
            partcount_cell[k][l]++;
         }
   }
}
/*******************************************
*******************************************
Printing of output to 10 files starts here */
/* Particle co-ordinates are printed only
  after every 2000 time steps  */
if (i%2000== 0)
{
   printf("%10.6f \n",(w+h));
   fprintf(data17_value,"%10.6f \n",h);
   fprintf(data16_value,"%10.6f \n",(w+h));
   /* print_num is used to print the total
      output into 10 different files */
   print_num= i/NI_10;

   // Start of output to 1st file
   if(print_num==0)
   {
      /* 50 particle positions are printed
         onto each line of the text file  */
      for(n=0;n<NP;n++)
      {
         for(j=0;j<ND;j++)
         {
            if(n==50 && j==0)
            {
               fprintf(data1_value, "\n");
            }
            if(n==100 && j==0)
            {
               fprintf(data1_value, "\n");
            }
            if(n==150 && j==0)
            {
               fprintf(data1_value, "\n");
            }
            if(n==200 && j==0)
            {
               fprintf(data1_value, "\n");
            }
            if(n==250 && j==0)
            {
```

```
                        fprintf(data1_value, "\n");
                     }
                     fprintf(data1_value,"%10.4f",
                        eta_new[n][j]);
                  }
               }
               if(n==NP)
               {
                  fprintf(data1_value, "\n");
               }
            } // close of if(print_num==0) loop
            // End of writing output to 1st file
            /* The output is written in similar fashion
               to the other 9 output files. The
               commands are not put here but are
               similar to the  if(print_num==0) loop.
               print_num ranges from 0 to 9. */
         } // close of if(i%2000==0) loop
         /* End of printing output
            ****************************************
            ****************************************/
         h_old = h;
         value=2;
      } // close of if(great_err<error_criter.) loop
      if(great_displ<ERROR_CRIT/5.)
         h=2*h;
   } // close of if(i>0) loop
   else value=2;
   if(brkval == 1)
      break;
} // close of while(value==1 loop
if(i==0)
{
   h_old=h;
}
w=w+h_old;
} //close of total iterations loop

// Closing of output files
fclose(data1_value);
fclose(data2_value);
fclose(data3_value);
fclose(data4_value);
fclose(data5_value);
fclose(data6_value);
fclose(data7_value);
fclose(data8_value);
fclose(data9_value);
fclose(data10_value);
fclose(data16_value);
fclose(data17_value);
```

```
   return(0);
} // close of main loop


//Sub-routine that calculates the net force on a particle

void fun_phi(double w,double h,double eta_curr[][3],int k,
   int l, int n,int part_in_cell[N_C_x][N_C_y]
   [max_part_cell], int nd, int rt,double force[ND])
{
   float x,Q,t;   /* parameters used for obtaining Brownian
      force */
   int k1,l1,k2,l2,n1,r1,r2,x0=20,y0=20,z0=50,i;
   double CR=0,pi=3.141592654,inv_dist,xsqdis,
      ysqdis,zsqdis,x_curr[3],inv_dist_3,dx_curr[3]; /*
      Variables used for evaluating net screened repulsions
      on a particle */
   double variance,rand_force,t_s=pow(10,-6); /* Variables
      used for evaluating Browian force */
   double ST=0 // Surface tension force
   double dlvo_const=(0.59933e9); /* dlvo_const is 4/(3πε),
      where ε is permittivity of water */
   double visc=0.001;  // Viscosity of water (equation 2.1)
   double inter_vel=1.11e5 ; /* Air-water interface velocity
      shown in equation 3.8  */
   double dia=0.000001; // particle diameter
   double air_dens=0.821; // Air density
   double susflu_dens=1000.; // Density of water
   double par_dens=1190.0;  // Particle density
   double charge=(4.7124e-16); /* surface charge on particle
      used in equation 2.16b */
   double inv_screen=100.96*(pow(10,5)); /* Inverse
      screening length 'k' given by equation 2.14 */
   double acc_grav=9.8; // Acceleration due to gravity
   double sur_ten=0.0728; // Air-water interfacial tension
   float c_0=2.515517,c_1=0.802853,c_2=0.010328,
      d_1=1.432788,d_2=0.189269,d_3=0.001308; /* constants
      needed for inverse cumulative distribution function */
   float TEMP=300.; // Temperature of the system in kelvin.
   float k_b=1.3806503*pow(10,-23); // Boltzmann constant.

   // Evaluating the net coloumbic repulsion force
   for (i=0; i<nd; i++) force[i] = 0.; /* Initial value of
      force is set to zero. */
   /* When calculating the force on a particle, only
      particles in the nearest sub-cells are considered.*/
   for( k1=k-1;k1<k+2;k1++)
   {
      for(l1=l-1;l1<l+2;l1++)
      {
```

```
if(k1==-1)
{
   k2=k1+ N_C_x;
   r1=-x0;
}
else if(k1==N_C_x)
{
   k2=k1-N_C_x;
   r1=x0;
}
else
{
   k2=k1;
   r1=0;
}
if(l1==-1)
{
   l2=l1+ N_C_y;
   r2=-y0;
}
else if(l1==N_C_y)
{
   l2=l1-N_C_y;
   r2=y0;
}
else
{
   l2=l1;
   r2=0;
}
/* Start of for loop that calculates the net
   columbic repulsive force on a single particle due
   to all particles in the surrounding sub-cells */
for(n1=0;n1<max_part_cell &&
   part_in_cell[k2][l2][n1]!=-1;n1++)
{
   if(part_in_cell[k][l][n]!=
      part_in_cell[k2][l2][n1])
   {
      xsqdis=pow((eta_curr[part_in_cell[k][l][n]][0]
         -(eta_curr[part_in_cell[k2][l2][n1]][0]
         +r1)),2);
      ysqdis=pow((eta_curr[part_in_cell[k][l][n]][1]
         -(eta_curr[part_in_cell[k2][l2][n1]][1]
         +r2)),2);
      zsqdis=pow((eta_curr[part_in_cell[k][l][n]][2]
         -eta_curr[part_in_cell[k2][l2][n1]][2]),2);
      inv_dist=1./sqrt(xsqdis + ysqdis + zsqdis);
      inv_dist_3 = ((dlvo_const/(visc*inter_vel))
         (dia*dia*dia))*charge* charge*
         ((exp(inv_screen*dia/2.))/
```

```
                (1+inv_screen*dia/2.0))*((exp(inv_screen*
                dia/2.))/(1+inv_screen*dia/2.0))
                *inv_dist*inv_dist*inv_dist;

             // Columbic force in the x-direction
             force[0] += inv_dist_3*(eta_curr[part_in_cell
                [k][l][n]][0]-(eta_curr[part_in_cell
                [k2][l2][n1]][0]+r1))*(exp(-inv_screen*dia/
                (2.*inv_dist)))*((inv_screen*dia/
                (2.*Inv_dist))+1.0);

             // Force in the y-direction
             force[1] += inv_dist_3*(eta_curr[part_in_cell
                [k][l][n]][1]-(eta_curr[part_in_cell
                [k2][l2][n1]][1]+r2))*(exp(-inv_screen*dia/
                (2.*inv_dist)))*((inv_screen*dia/
                (2.*Inv_dist))+1.0);

             // Force in the z-direction
             force[2] += inv_dist_3*(eta_curr[part_in_cell
                [k][l][n]][2]-eta_curr[part_in_cell
                [k2][l2][n1]][2])*(exp(-inv_screen*dia/
                (2.*inv_dist)))*((inv_screen*dia/
                (2.*Inv_dist))+1.0);
          } // close of if loop
       } // close of for (n1=0) loop
    } // close of for (l1=l-1) loop
}  // close of for (k1=k-1) loop
// End of evaluating net Columbic Repulsions

/* Random Force calculation: The random number generator
   ran1() that generates uniformly ditributed random
   numbers between 0 and 1 is taken from "Numerical
   Recipes in C", Cambridge University Press, Cambridge,
   1996. */
variance=6*pi*k_b*TEMP*visc*dia/(t_s); // Equation 2.7
for(i=0;i<nd;i++)
{
   x= ran1(&seed);
   Q=1-x;
   t=sqrt(log(1/(Q*Q)));
   rand_force=((sqrt(variance))*((t-(c_0+c_1*t+c_2*t*t)/
   (1+d_1*t+d_2*t*t+d_3*t*t*t))-0.016))/
   (3*pi*visc*dia*inter_vel);
   force[i] += rand_force;
}
// End of evaluating random force on a particle

// Surface Tension Force
if(eta_curr[part_in_cell[k][l][n]][2]<1)
   force[2]=0; /*If a article hits the substrate, its z-
      direction velocity is made zero */
```

```
   else
   {
      if((z0-w-eta_curr[part_in_cell[k][l][n]][2])<1)
      {
         ST=-(sur_ten/(3*visc*inter_vel))*(1-
            (z0-w-eta_curr[part_in_cell[k][l][n]][2])*
            (z0-w-eta_curr[part_in_cell[k][l][n]][2]));
         force[2] += ST;
      }
   }
   return;
} /* End of Sub-routine for calculating net force on a
   particle */

/*************************************************************
   Sub-routine for random number generator, ran1() */

float ran1(long *idum)
{
   int j;
   long k;
   static long iy=0;
   static long iv[NTAB];
   float temp;

   if (*idum <= 0 || !iy)
   {
     if (-(*idum) < 1) *idum=1;
     else *idum = -(*idum);
     for (j=NTAB+7;j&gt;=0;j--)
     {
        k=(*idum)/IQ;
        *idum=IA*(*idum-k*IQ)-IR*k;
        if (*idum &lt; 0) *idum += IM;
        if (j &lt; NTAB) iv[j] = *idum;
     }
     iy=iv[0];
   }
   k=(*idum)/IQ;
   *idum=IA*(*idum-k*IQ)-IR*k;
   if (*idum &lt; 0) *idum += IM;
   j=iy/NDIV;
   iy=iv[j];
   iv[j] = *idum;
   if ((temp=AM*iy) &gt; RNMX) return RNMX;
   else return temp;
}  // End of subroutine for ran1()
```